PERFORMANCE OF AN OPEN ENDS SQUEEZE FILM DAMPER OPERATING WITH LARGE AMPLITUDE ORBITAL MOTIONS: EXPERIMENTAL ANALYSIS AND ASSESSMENT OF THE ACCURACY OF THE LINEARIZED FORCE COEFFICIENTS MODEL

A Thesis

by

SUNG-HWA JEUNG

Submitted to the Office of Graduate and Professional Studies of
Texas A&M University
in partial fulfillment of the requirements for the degree of

MASTER OF SCIENCE

Chair of Committee,	Luis San Andrés
Committee Members,	Alan Palazzolo
	Stefan Hurlebaus
Head of Department,	Andreas Polycarpou

December 2013

Major Subject: Mechanical Engineering

Copyright 2013 Sung-Hwa Jeung

ABSTRACT

Squeeze Film Dampers (SFDs) aid to suppress rotor vibrations and enhance the stability of high-speed rotor-bearing systems. A SFD is a simple oil lubricated film between a stationary housing and a precessing (whirling) journal. Aircraft engines use SFDs as the only means to provide damping to otherwise rigid ball bearing supports. This thesis presents experimental results for the dynamic forced performance of a test open ends SFD operating with large amplitude whirl motions, centered and off centered within the bearing clearance. The test rig comprises of an elastically supported bearing with a damper section having two parallel film lands separated by a feed groove. A film land is 25.4 mm long, with diameter 127 mm and nominal radial clearance c=0.251 mm. Two orthogonally placed shakers apply dynamic loads on the bearing to induce circular orbit motions at prescribed whirl frequencies. A static loader, 45˚ away from each shaker, pulls the bearing to a static eccentric position.

Circular orbit tests were performed (10 – 100 Hz frequency range) for eight increasing orbit amplitudes (r=0.08c to ~0.71c) and under four static eccentricities (e_s=0.0c to ~0.76c). An identification method estimates the test damper force coefficients from transfer functions in the frequency domain. The analysis shows that the SFD damping force coefficients increase with the static eccentricity (e_s) increase. On the other hand, the damper inertia coefficients decrease as the orbit amplitude (r) becomes large and also increase modestly with the static eccentricity (e_s). Predictions from a physical model show good agreement with the test dynamic force coefficients.

The accuracy of the linearized SFD force coefficients $(\mathbf{K}, \mathbf{C}, \mathbf{M})_{SFD}$ is evaluated from comparing the differences in mechanical work performed by actual and linear SFD reaction forces. The difference in mechanical work (E_{diff}) increases with increasing static eccentricity (e_s) and orbit amplitude (r). However, for most test conditions (r/c≤0.4,

$e_s/c \leq 0.25$), E_{diff} is less than ~5%, thus showing the linearized SFD force coefficients represent well the forced response of the actual test SFD system.

The test and predicted force coefficients as well as the analysis of the pressure fields contribute to a better understanding of the kinetics of SFDs operating with moderate to large amplitude size whirl motions, centered and off-centered.

DEDICATION

To my father, mother and sister for their endless love.

ACKNOWLEDGEMENTS

I gratefully thank Dr. Luis San Andrés, my advisor, for guiding me to becoming a better engineer. His sincere support and advice led me to finish my M.S. degree. His endless curiosity, passion and love for nature greatly inspired my attitude toward research.

I thank Turbomachinery Research Consortium (TRC) for their financial support during my M.S. program. I acknowledge my committee members, Dr. Stefan Hurlebaus and Dr. Alan Palazzolo, for their time and interest. I also thank Pratt & Whitney Engines (UTC) for their support and interest on the squeeze film damper research program.

I would like to thank my friends at the Turbomachinery Lab., Gary Bradley, Alain Anderson, Feng Yu, Yingkun Li, Joshua Norsworthy, Travis Cable, and Yujiao Tao for sharing their ideas on my research. Special thanks go to former student Mr. Sanjeev Seshagiri, Dr. Adolfo Delgado, Ms. Paola Mahecha and Shraddha Sangelkar for their effort to build up the SFD test rig.

NOMENCLATURE

a_X, a_Y	Bearing cartridge acceleration [m/s^2]
c	Film land clearance [m]
$C_{\alpha\beta,\ (\alpha,\beta=X,Y)}$	Damping coefficients [N.s/m]
C_S	Remnant damping coefficient [N.s/m]
d_G	Groove depth [m]
d_η	Effective groove depth [m]
D	Journal diameter [m], R= ½ D
e_s	Static eccentricity (along 45^o) [m]
e_X, e_Y	Dynamic eccentricity components [m]
E	Mechanical work [N·m]
f_n	Test system natural frequency [Hz]
f_{start} ,f_{end}	Start and end frequencies for system parameter identification [Hz]
h	Film thickness [m]
i	$\sqrt{-1}$. Imaginary unit
$K_{\alpha\beta,\ (\alpha,\beta=X,Y)}$	Stiffness coefficients [N/m]
K_S	Structural support stiffness [N/m]
L	Damper axial length [m]
L_F	Film land length [m]
L_G	Grove width [m]
$M_{\alpha\beta,\ (\alpha,\beta=X,Y)}$	Mass coefficients [kg]
M_S	Remnant mass coefficients [kg]
M_{BC}	Bearing cartridge mass [kg]
O_B, O_J	Bearing cartridge center and journal center
P	Dynamic pressures in film land [Pa]
P_a, P_{cav}	Ambient pressure and lubricant cavitation pressure [Pa]
P_{in}, P_G	Static oil pressure at journal inlet and in the central groove [Pa]

$\overline{P}$	Normalized pressure [-]
P^*	Normalized factor [Pa]
Q_{in}	Lubricant flow rate [LPM]
Q_T, Q_B	Lubricant flow rate through top and bottom lands [LPM]
r, r_X, r_Y	Circular orbit amplitude and its components along X and Y directions [m]
$\overline{r}$	r/c. Dimensionless orbit radius [-]
R	Journal radius [m], R= ½ D
R_T, R_B, R_o	Top and bottom film lands and orifice fluidic resistances
Re_s	$\rho\omega c^2/\mu$. Modified squeeze film Reynolds number [-]
t	Time [s]
T	Temperature [ºC]
X,Y	Coordinate axes
$x_{(t)}$, $y_{(t)}$	Relative displacement of bearing cartridge respect to the journal
γ	Squeeze flow parameter [-]
ξ	Damping ratio [-]
θ	x/R. Circumferential coordinate [rad]
Θ	Fixed angular coordinates [rad]
ρ,μ	Oil density [kg/m^3] and viscosity [Pa.s]
ω	Excitation frequency [rad/s]

Vectors and matrices

$\mathbf{a}_{(t)}$	$\{a_X, a_Y\}^T$ Vector of bearing accelerations [m/s^2]
$\overline{\mathbf{a}}_{(\omega)}$	$DFT\lfloor \mathbf{a}_{(t)} \rfloor$ Discrete Fourier transform of accelerations [m/s^2]
$\mathbf{C}$	Matrix of damping coefficient
$\mathbf{K}$	Matrix of stiffness coefficient
$\mathbf{F}_{(t)}$	$\{F_X, F_Y\}^T$ Vector of dynamic loads [N]

$\overline{\mathbf{F}}_{(\omega)}$	$DFT\lfloor \mathbf{F}_{(t)} \rfloor$ Discrete Fourier transform of accelerations [m/s^2]
$\mathbf{F}_{\mathbf{SFD}}$	Actual *nonlinear* SFD reaction force vector [N]
$\mathbf{F}_{\mathbf{SFD_L}}$	*Linearized* SFD reaction force vector [N]
G	$\mathbf{H}^{-1}$. Flexibility matrix [m/N]
H	$\mathbf{K} - \omega^2\mathbf{M} + i\,\omega\mathbf{C}$. Matrix of impedance coefficients [N/m]
M	Matrix of added mass coefficient
$\mathbf{z}_{(t)}$	$\{x,y\}^T$ Vector of bearing displacements relative to journal [m]
$\overline{\mathbf{Z}}_{(\omega)}$	$DFT\lfloor \mathbf{z}_{(t)} \rfloor$ Discrete Fourier transform of bearing displacements [m]

Subscripts

BC	Bearing cartridge
k	Single frequency excitation index
s	Structure
L	Lubricated system
SFD	Squeeze film damper
DIS	Dissipation
diff	Difference

TABLE OF CONTENTS

LIST OF FIGURES

FIGURE Page

LIST OF TABLES

CHAPTER I

INTRODUCTION

Modern high-speed turbomachinery uses flexible rotors and hence is sensitive to imbalance. High-speed operation causes large amplitude rotor motions and undesirable large dynamic loading on the bearing supports. A Squeeze Film Damper (SFD) can reduce rotor vibrations as it crosses system critical speeds. Thus, SFDs are widely adopted in aircraft engines and high-speed compressors to provide viscous damping to dissipate mechanical energy from rotor vibrations, to isolate structural components; and in other application, to improve the overall dynamic stability of rotor-bearing systems and to increase the life of support rolling element bearings [1,2].

Since the mid-1980s, the SFD research program at Texas A&M University brings significant contributions developing improved SFD analyses and design tools benchmarked by extensive experimental data.

Figure 1 depicts an open ends SFD in series with a ball bearing to support a rotating structure (shaft). The damper has two film lands of small clearance separated by a deep feed groove. The groove acts as a source of lubricant flowing continuously towards the adjacent film lands. A pin prevents the rotation of the journal holding the outer race of the ball bearing. Hence, the journal whirls (precesses) in the clearance space filled with a lubricant to generate hydrodynamic pressures that produce reaction forces. These forces, dynamic in character, oppose the journal whirl motion. In particular, forces parallel to the journal path, but opposite to it, are dissipative [2].

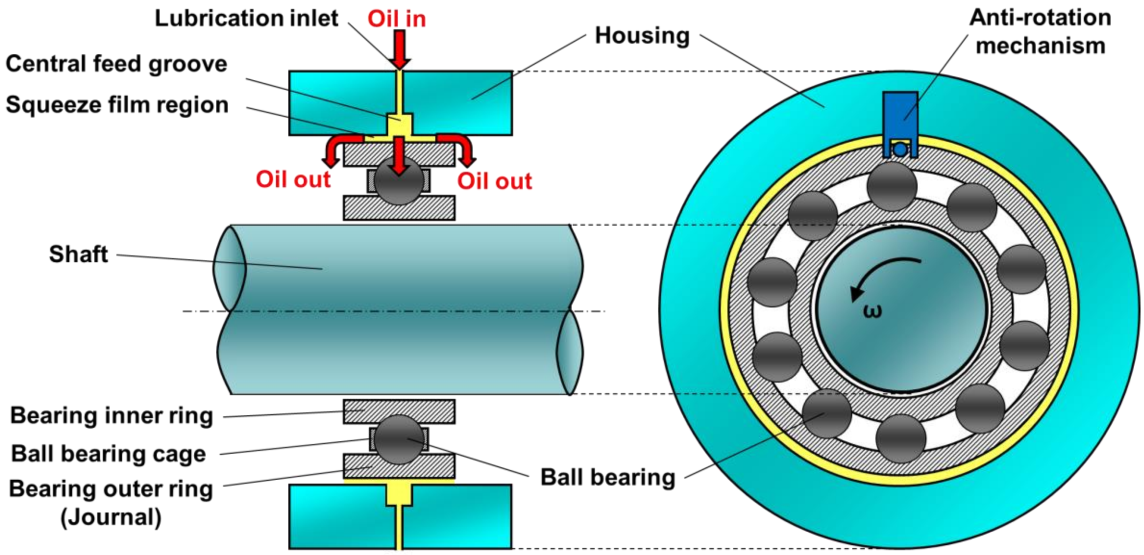

Fig. 1 Schematic view of an open ends squeeze film damper (SFD) with a central feed groove and ball bearing to support a rotor system [1].

In prior research applicable to gas turbine engines, Refs. [3-5] evaluate the dynamic forced performance of open ends SFDs and sealed ends SFDs with two film land lengths separated by a deep groove. Two journals, long and short, both with a diameter of 127 mm and a radial clearance of 0.127 mm, form 12.7 mm and 25.4 mm length film lands, respectively. First, Seshagiri [4] obtained force coefficients for an open ends SFD from circular orbits with amplitudes (r) equal to 10% of the film radial clearance c=127 μm (5 mil) and with journal static eccentricities (e_s) up to 66% of the film clearance. Later, with the same damper clearance but in a configuration with piston ring end seals, Mahecha [6] conducted tests to identify force coefficients from circular orbits with an amplitude (r) equal to 5.5% of the bearing clearance and static eccentricities (e_s) as large as 37% of the radial clearance. The experimental results in Refs. [4,5] show that the direct damping coefficients are sensitive to the amplitude (r) of the circular orbit and slightly increase with the static eccentricity (e_s), whereas the direct added mass coefficients decrease with an increase in orbit amplitude and show a mild increase with e_s. The test data also show the cross-coupled damping and added mass coefficients are negligible.

The current work extends prior art by performing experiments on the same SFD test rig [4,5] with a damper having a (larger) radial clearance c=251 μm (10 mil) and with film lands length equal to 25.4 mm. Presently, the film clearance is twice the original clearance in Refs. [4,6], but the feed groove depth and width are the same as in the past configuration. To extend prior knowledge, the current work produces larger orbital motions with amplitudes (r) to 71% of the film clearance (c) and larger bearing static eccentricities (e_s) to 76% c. Note that large whirl amplitude motions and high whirl frequencies make SFDs susceptible to lubricant cavitation (gas/vapor) and air entrainment; in particular for the open ends configuration [6]. Recall that the damping capacity of a SFD decreases as oil cavitation and air entrainment persist in the squeeze film lands [7,8]. The research obtains experimental dynamic forced coefficients (stiffness K_{SFD}, damping C_{SFD}, and added mass M_{SFD}) of an open ends SFD operating with large r and e_s. Finally, the validity of estimated SFD force coefficients is assessed by comparing the in mechanical work performed by actual and linearized SFD forces.

CHAPTER II

LITERATURE REVIEW

This chapter presents a compilation review of literature related to open ends squeeze film dampers (SFDs). In particular, the review addresses to the effects of feed grooves and fluid inertia on SFD forced performance, the identification of SFD force coefficients, and the quantification of air ingestion in SFDs.

Della Pietra and Adilletta [9,10] summarize the technical issues related to SFDs from their invention in 1963 through 2002. The review papers describe SFD configurations, their theoretical background, and the applications. Until 2002, SFD predictive analyses fell short of predicting actual performance.

1. Fluid inertia effects on SFDs with groove

In 1985, San Andrés [11] studies the influence of fluid inertia on the dynamic force performance of a SFD with a central groove, and finds that the groove affects the pressure profiles as well as the dynamic reaction forces in the damper. The author also derives a model that predicts the SFD force coefficients including convective and temporal fluid inertia terms for operation with circular centered journal motions. Importantly enough, the analysis shows that the added mass decreases with an increasing orbit amplitude, eventually reaching zero. On the other hand, the direct damping coefficient increases with an increasing orbit amplitude and also with the squeeze film Reynolds number ($Re_s = \frac{\rho \omega c^2}{\mu}$)[1]. The author questions the conventional knowledge that the lubricant pressure in a deep groove is invariant and that the film lands are effectively isolated by a groove. Later, San Andrés and Vance [12] show experimentally that the

[1] The parameters (ρ, μ) are the lubricant density and viscosity, ω denotes the whirl frequency, and c is a film radial clearance.

dynamic pressure in a feed groove is not nil, and which affects the overall dynamic forced coefficients of the test SFD.

Tichy [13] analyzes the effect of fluid inertia forces on the generation of dynamic pressures in a SFD. The analysis shows that fluid inertia causes a phase shift of the dynamic peak pressure. The magnitude of the phase shift decreases as the dynamic eccentricity of the journal increases. Ends side leakage rate (open ends condition) reduces the influence of fluid inertia on the dynamic pressure profile. The author concludes that an open ends SFD is more susceptible to variations in the pressure profile than a sealed ends SFD.

San Andrés [14] presents a model to predict SFD force coefficients based on the short length bearing model and for small amplitude journal motions about a centered condition. He presents a laminar flow analysis in the damper film lands and considers the liquid compressibility effects in the feeding central groove. Predictions of SFD force coefficients are in agreement with the experiment results from Ramli *et al*. [15].

Arauz and San Andrés [16] study the dynamic force response of an open ends SFD with various groove configurations (length $L_G = 0.1L_F$, $0.2L_F$, $0.3L_F$ and depth $d_G = 0.0c$, $3.5c$, $6c$, $11c$, $25c$ where the film land L_F=26.4 mm and clearance c=0.381 mm). The dynamic pressures in the film lands and in the groove are measured for a journal whirling with circular centered orbits with moderate size amplitudes, r=0.25c and 0.50c. Recorded film pressures are integrated to estimate fluid film reaction forces. As the groove depth increases to d_G/c=25, the damping force decreases rapidly, and approaches the predicted damping force from classical lubrication theory which considers the dynamic pressure in a deep groove to be nil. Furthermore, the same order magnitude of fluid inertia forces is estimated at both the circumferential groove and the adjacent film land.

Qingchang *et al*. [17] present a simplified Navier-Stokes equation analysis for an open-ends SFD with a circumferential feeding groove. The paper includes comparisons between predicted SFD dynamic force performance and experimentally determined fluid film reaction forces at the groove and at the film lands (L=9 cm, L_G=2 cm, d_G=0.7 mm,

c=0.2 mm). From the comparisons, the authors conclude that the groove depth mainly affects the fluid film tangential force rather than the radial force. This conclusion opposes prior findings for SFDs with a feed groove [11,14,16]. Predicted and experimental SFD tangential forces agree well over a range of orbit amplitudes r/c=0.1 - 0.5. However, for orbit amplitudes r/c>0.5, the tangential forces are overpredicted by about 30% whereas the SFD radial (inertia) forces are largely underpredicted throughout the whirl amplitude range, $r = 0.0c - 0.75c$.

2. Identification of SFDs force coefficients

Accurate estimation of the mechanical parameters in a structural system validates mechanical performance and integrity. To date, various analytical and experimental dynamic parameter identification methods exist to estimate the physical parameters of a mechanical system. This section focuses on the identification of force coefficients in SFDs.

The practitioners should refer to Tiwari *et al.* [18] for a thorough review of parameter identification techniques applied to fluid film bearings in rotating machinery. The authors categorize the identification methods by bearing types and the type of excitation used. Fritzen [19] presents the *Instrumental Variable Filter* (IVF) method for parameter identification as an extension of the least-square method. The IVF method delivers consistent estimations from measured data with noise.

Recently, San Andrés and Delgado [20-22], San Andrés [3], Seshaghiri [4], and Mahecha [5] present investigations on the identification of dynamic force coefficients in a grooved SFD. The authors compare experimental damping and inertia force coefficients with predictions from a model that accounts for an effective groove depth, different from the physical groove depth. This effective groove depth is the separation streamline that borders with a recirculation region (vortice) in the groove. By adopting the effective groove concept, the discrepancy between the dynamic force coefficients derived from predictions and experiments is reduced. In spite of the excellent agreement, actual experiments or Computational Fluid Dynamics (CFD) models are required to deliver a sound estimate of the effective groove depth.

Gehannin *et al*. [23] present analyses of SFDs based on a bulk flow model that accounts for convective fluid inertia effect, plus the local effects of feeding groove and feeding orifices. Predicted SFD tangential and radial forces are compared with the experimental results in Ref. [24]. Since the classical Reynolds equation does not account for fluid inertia effects, it largely underpredicts the test results of the test SFD radial force at r/c>0.5, whereas the bulk flow model correlates well with the SFD tangential and radial forces throughout the operating conditions. The conclusions show that the bulk flow model is suitable to predict SFD performance when the thin film flow is dominated by convective fluid inertia, Re_s>1.

3. Air ingestion in SFDs

The open ends SFD is a widely adopted damper design for air breathing jet engines. Air ingestion and entrapment is common in open ends SFDs operating with high whirl frequencies and large amplitude displacement motions [25-28]. Air ingestion occurs naturally when a film thickness increases locally as it generates a suction pressure at the discharge side of the damper. On the other hand, gaseous cavitation takes place when the film dynamic pressure reaches a sub-ambient magnitude at which dissolved gases in the lubricant divulge from the oil [6]. Air entrainment and gaseous oil cavitation are distinct phenomena.

San Andrés and Diaz [27] utilize a digital high-speed camera to record the images of air entraining into the lubricant film region in a SFD performing circular centered orbits. As air entrains, a constant pressure area develops and extends as the whirl frequency and air volume in the oil increases. Later, Diaz and San Andrés [28] show the tangential (damping) force decreases as the air-in-oil volume ratio increases. On the other hand, the radial (inertia) force shows a persistent magnitude until it rapidly decrease to zero for large air-in-oil volume fractions above 80%. Furthermore, the authors also find that the peak-to-peak film dynamic pressure decreases as the volume fraction of air in the lubricant bubbly mixture increases.

Diaz and San Andrés [29] present a two-phase bubbly mixture SFD model based on a simplified version of the *Rayleigh-Plesset* equation (*RPE*) [30]. The authors introduce a feed squeeze flow parameter γ, the ratio between q_{oil}, the oil supply flow rate, and $q_{sqz}=\pi DLr\omega$, the rate of volume change due to squeeze motion of the journal. The onset of air entrainment occurs when $\gamma=q_{oil}/q_{sqz}<1$, i.e., when there is not enough lubricant flow to replenish the physically displaced oil volume as the journal moves. The feed squeeze flow parameter γ is used to estimate the actual air in oil volume fraction β. Using the proposed model, predictions are compared with earlier measurements of a SFD performing circular centered orbits [28,31]. The comparisons show the proposed model gives a better agreement in both tangential forces and radial forces than previous work based on the continuum mixture theory (*CMT*) model [32]. However, note that the predictions of the squeeze film pressures and ensuing forces (tangential and radial) require of an a priori estimation of the air-to-oil mixture ratio (β). In addition, the predictions are valid for short length bearings ($L/D<0.5$) operating with circular centered journal motions only.

Mendez *et al*. [33] extend previous work [29] by modeling numerically finite length SFDs. The authors analyze the correlation amongst the feed squeeze flow number (γ), the air volume fraction (β), and the damper slenderness ratio (L/D). Expectedly, as γ decreases, the air volume fraction in the lubricant (β) increases. However, the air volume fraction (β) decreases for long dampers. In other words, for a fixed journal diameter, as the bearing length increases, the damper is less prone to air ingestion. Later, Torres and Diaz [34] continue the computational analysis of air ingestion in SFDs. In sum, the predictions show that air ingestion in the damper film land increases with a decreasing feed squeeze flow parameter (γ) or L/D. However, the air in oil volume fraction (β) increases with increasing journal orbit amplitudes. Even though, the magnitude of the film clearance, orbit amplitude, bearing length and diameter are different, predictions on the air volume fraction are identical when the slenderness ratio (L/D) and orbit amplitude ratio (r/c) are the same. In other words, the air volume fraction (β) depends on the ratios L/D and r/c only. To date, there is no experimental data verifying the predictions in Refs. [33,34].

4. SFDs undergoing large amplitude motions

Zhang *et al*. [35] measure the dynamic forced performance of a SFD operating with circular orbital motions as large as 80% of the film clearance. The open ends SFD consists of two parallel film lands (L_F=20.4 mm, D=136 mm) separated by a shallow circumferential groove (depth d_G=2.5c). The squeeze film Reynolds number (Re_s) ranges from 0.25 to 1.2. Experimental results are shown as radial and tangential forces versus orbit radius (r). Interestingly enough, estimated fluid tangential and radial forces show an abrupt change at an orbit amplitude of r/c=0.5. The aforementioned SFD responses represent '*jump'* phenomenon, typical of a nonlinear structural system. The experimental results also show that the damper inertia and damping coefficients are independent of the changes in lubricant feed pressure, but increase as the journal orbit amplitude increases. Furthermore, the damping coefficients decrease slightly with whirl frequency whereas the inertia coefficients are independent of whirl frequency.

Lastly, San Andrés and De Santiago [36] present identified SFD force coefficients in an open ends SFD operating with both circular and elliptical centered orbits with radii (r) up to 80% of the damper radial clearance (c). The authors introduce the concept of an effective axial length to link the experimentally identified SFD forced coefficients and the predictions using classical formulas in Ref. [11]. The estimated SFD damping coefficients show good correlation with conventional formulas when considering an effective length ~20% smaller than the actual length. A rationale for a smaller effective damper length follows from the insufficient lubricant supply (flow rate) that cannot replace the dynamic volume change caused by the large amplitude orbit motions. The rationale is also supported by measured dynamic pressures which show the prevalence of air entrainment that increases with an increasing orbit amplitude and whirl frequency.

CHAPTER III

TEST RIG DESCRIPTION

This chapter presents a detailed description of the SFD test rig, including the data acquisition system, lubricant properties, and the oil supply system. The SFD test rig replicates actual configurations in aircraft engines.

Figure 2 shows the top and cross-section views of the SFD test rig and its components labeled. The bearing assembly consists of a bearing cartridge (BC) supported on four main steel rods, spaced 90º apart, attached to a pedestal which is firmly affixed atop a rigid table. The BC provides an interface with the shakers and the static loader, and also holds various sensors: two pairs of eddy current displacement sensors, two accelerometers, two load cells and six pressure sensors. This design allows the journal to be exchangeable without altering the bearing assembly and installed instrumentations.

Figure 3 shows a cross section view of the test rig assembly with the journal installed and Table 1 lists the basic dimensions of the SFD. A journal with outer diameter of 127 mm (5 in) is installed on a journal base that is firmly affixed to a pedestal. The clearance (c) between the BC and the journal creates the lubricant film lands c=0.251mm (9.9 mil).

The squeeze film region consists of the two film lands each, with length L_F=25.4 mm, and a central groove of width L_G=12.7 mm. Thus, the oil wetted length is L=2L_F+L_G 63.5 mm (2.5 in). The circumferential groove in the BC inner surface fills with lubricant for subminister to the top and bottom film lands. The central groove depth d_G is 9.5 mm, ~38 times the film land clearance ($d_G \simeq 38c$).

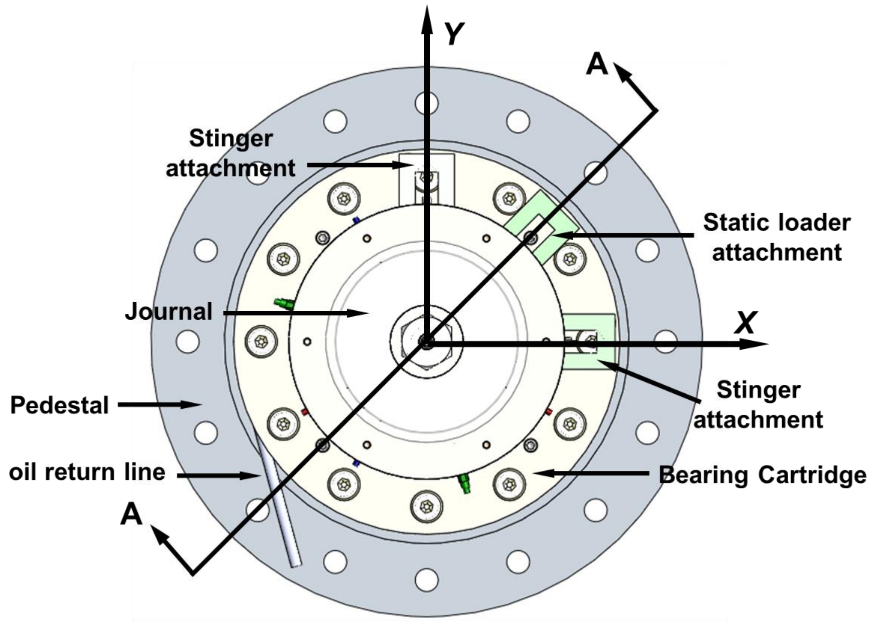

(a) Top view of SFD test bearing

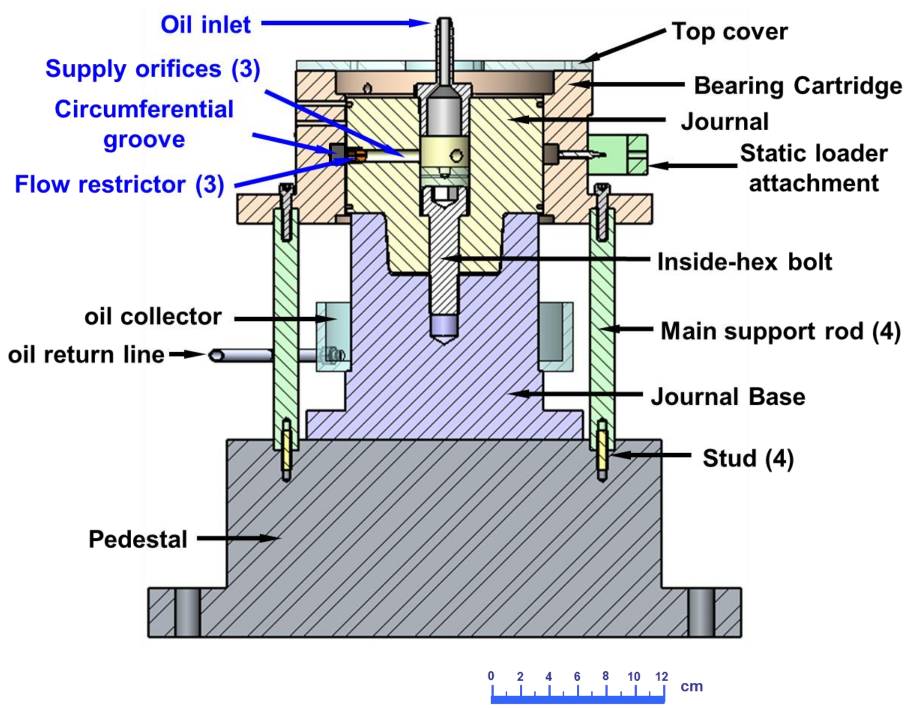

(b) Cross section (A-A) view of SFD test bearing

Fig. 2 Top and cross section views of SFD test rig

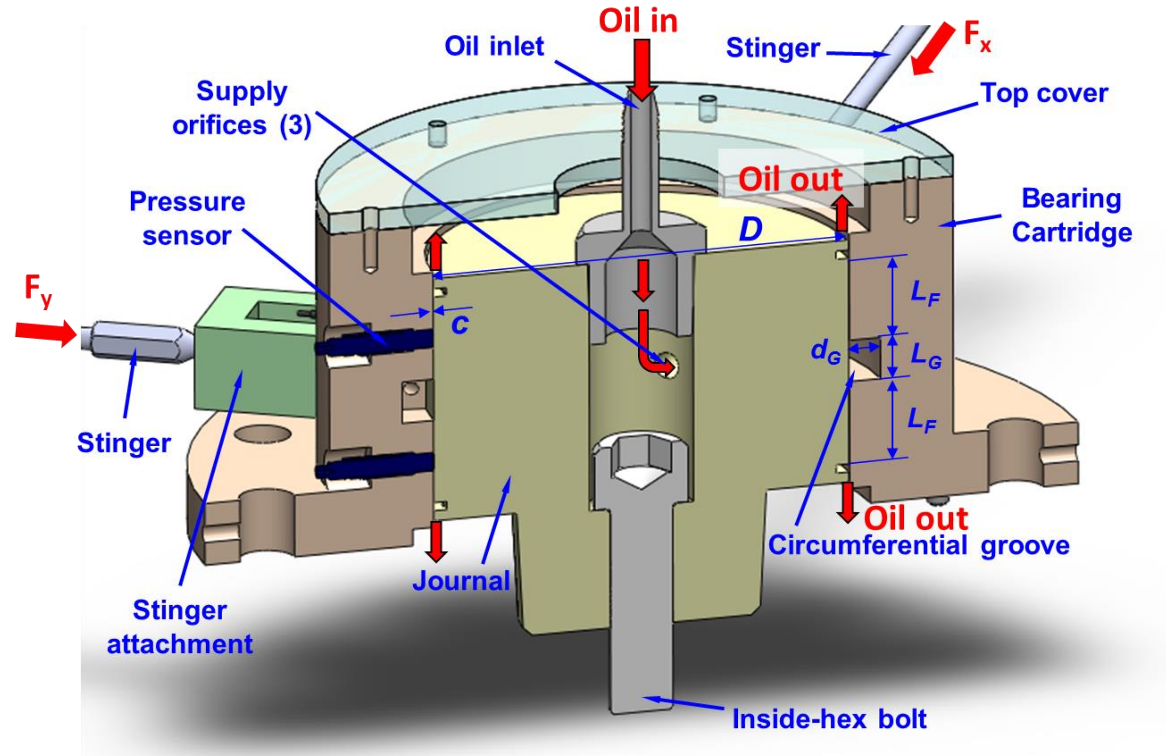

Fig. 3 Cross section view of test SFD with open ends.

Table 1. Main dimensions for open ends SFD.

Geometry (three feed holes 120° apart)	
Journal Diameter, D	12.7 cm (5.0 in) ± 2.5 μm
Land Length, L_F	2.54 cm (1.0 in) ± 12.7 μm
Radial Land Clearance, c	251.5 μm (9.9 mil) ± 2.5 μm
Damper Axial Length (two lands + groove), L	6.35 cm (2.5 in) ± 12.7 μm
Feed orifice Diameter, ϕ	2.54 mm (0.1 inch) ± 12.7 μm
Central Groove	
Groove Axial length, L_G	1.27 cm (0.5 inch) ± 12.7 μm
Groove Depth, d_G	0.96 cm (0.38 inch) ± 12.7 μm

Figure 4 shows a photograph of the journal as well as its top and cross sectional views. The hollow journal has a vertical flow path where oil is supplied and routed through three equally spaced (120°) horizontal orifices (ϕ = 2.54 mm) to flood the circumferential groove. The oil then flows through the top and bottom film lands to finally discharge to ambient (see Figure 5). The two grooves at the ends of the journal (top and bottom film lands) provide space for the (future) installation of piston ring seals.

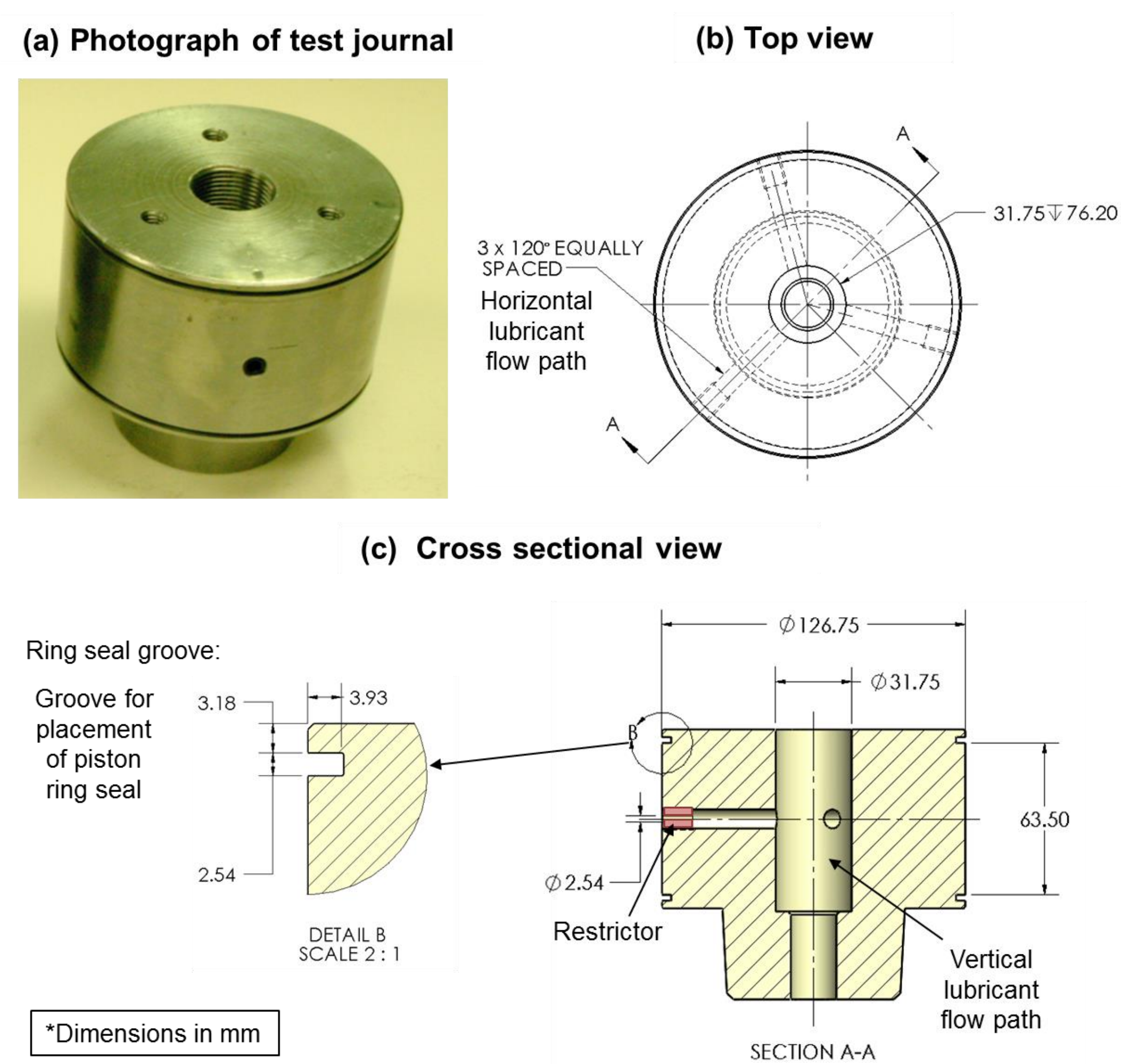

Fig. 4 Test journal: (a) photograph, (b) top view, and (c) cross sectional view

Figure 5 depicts a schematic view of the SFD damper section with the sensors installed in the BC and showing the lubricant flow path. Six piezoelectric pressure sensors measure the dynamic pressures in the film lands (θ=120° and 240°) and in the central groove (θ=165° and 285°), as shown in the figure. Note that the pressure sensor tips are flushed with the BC inner wall to ensure a smooth curved surface. Displacement sensors installed in the central groove along the *X* and *Y* directions measure the relative displacement of the BC with respect to the journal. During dynamic load tests, the BC accelerations are measured with piezoelectric accelerometers.

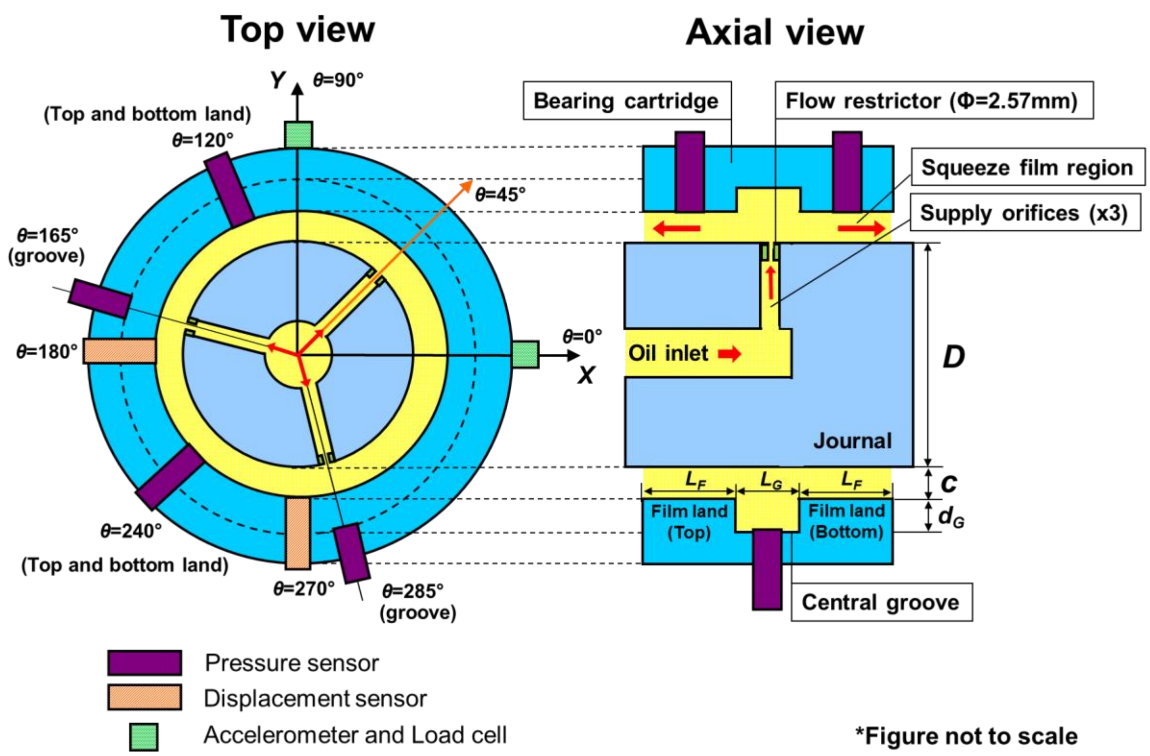

Fig. 5 Top and axial cross sectional views of open-ends SFD section with disposition of sensors and showing the lubricant flow path (exaggerated film clearance for illustrative purpose).

Figure 6 show an isometric view of the SFD test rig assembly. The test apparatus rests atop a vibration-absorbing mat and is rigidly attached to a massive table. Two electromagnetic shakers, with a maximum capacity of 2,200N, are positioned along the

X and Y directions and linked to the test bearing via stingers. A hydraulic piston, located 45° away from the X and Y directions and in between the two shakers, exerts static loads that displace statically the test bearing to a set eccentricity e_s<c. The maximum BC static eccentric position equals to the radial clearance (c).

Unidirectional, circular, and elliptical BC motions are generated by controlling the two shakers load amplitudes and relative phase. At the same time, various journal static eccentricity conditions are set by using the static loader.

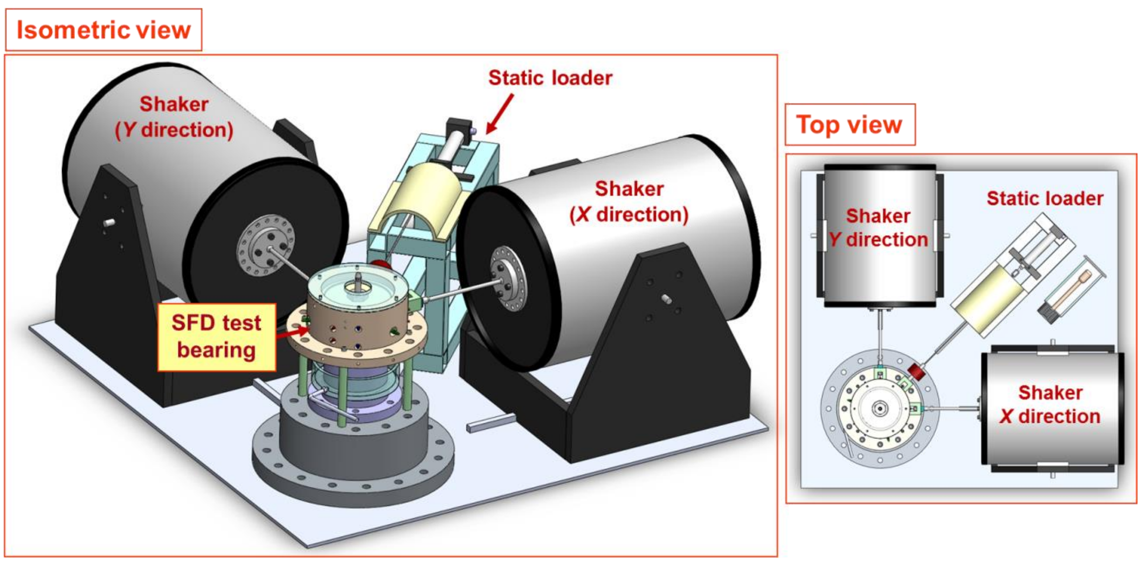

Fig. 6 Isometric and top views of the SFD test rig assembly [37].

1. Data acquisition system

In all measurements, a data acquisition (DAQ) system and an in-house LabVIEW® program record the output signal of the sensors and control the input voltages going through the shakers to regulate the amplitude motions of the BC. Refs. [4,5] present detailed descriptions of the DAQ system. The DAQ sampling rate is 16,384 samples/second and the DAQ stores 4,096 samples for each test condition.

For post-processing, an in-house MathCAD® program takes the recorded physical data (applied shaker loads, BC accelerations, and BC to journal relative displacements), perform an identification procedure and yields the lubricated damper system parameters (stiffness $\mathbf{K_L}$, added mass $\mathbf{M_L}$, and damping coefficient $\mathbf{C_L}$).

2. Lubricant supply system and properties

Figure 7 depicts a schematic view of the lubrication delivery system. The lubricant system consists of a storage tank (max. 150 liter) and a motor pump (5 HP). The motor pump can supply the lubricant to the test rig up to a maximum flow rate of 37.9 LPM (10 GPM) and its flow rate can be regulated by a remote controller.

The inlet lubricant flow rate (Q_{in}) is manually adjusted based on the measurement of the turbine-type flowmeter installed in the supply line. The supplied lubricant enters through the oil inlet and then flows through the damper top and bottom lands. After the lubricant discharges through the top and bottom lands, it is collected and recirculated to the storage tank by a separate return pump.

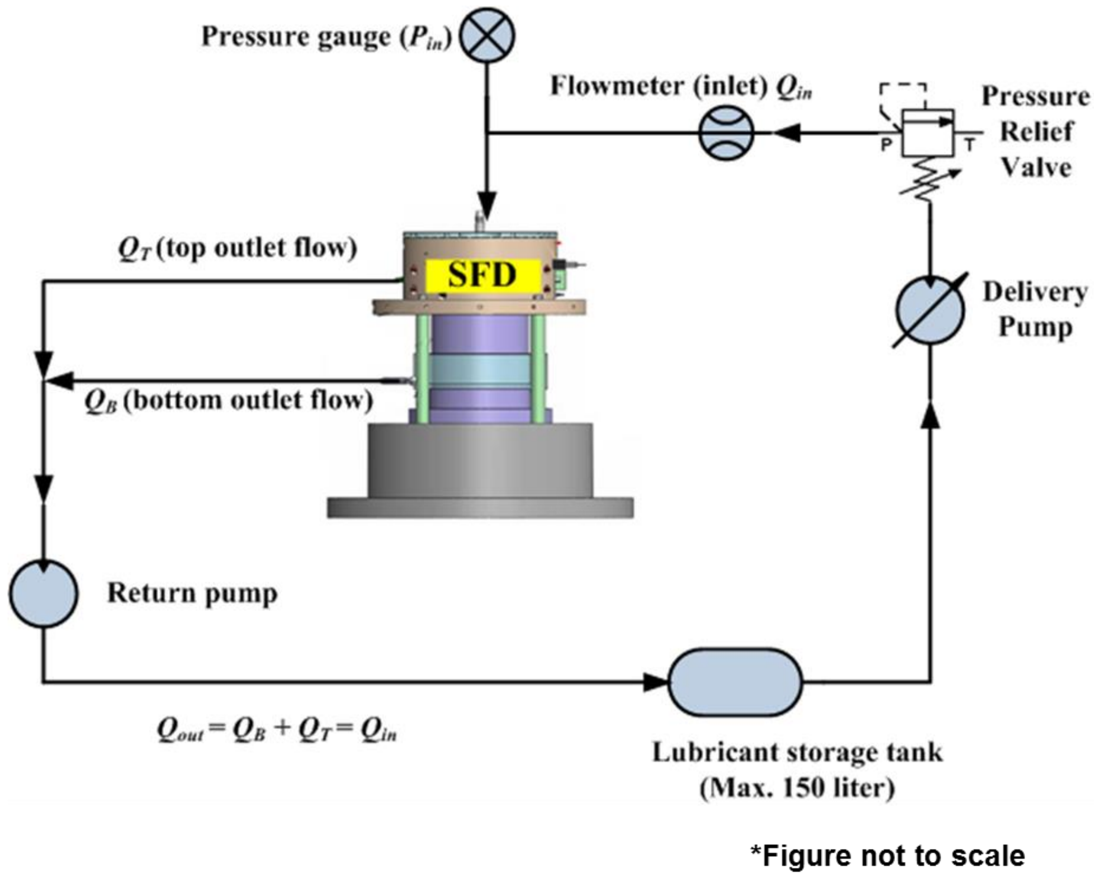

Fig. 7 Schematic view of lubricant system [4]

An ISO VG 2 grade lubricant with density ρ=785±0.5 kg/m^3 is used to lubricate the damper film lands. The measured oil viscosity follows

$$\mu(T) = \mu_0 e^{-0.0187\frac{1}{°\mathrm{C}}(T-T_0)} \tag{1}$$

where μ_0=2.96 cPoise and T_0=25.2ºC [5].

CHAPTER IV

FLOW RATE MEASUREMENTS

This chapter describes the experimental procedure for flow rate measurements and the results. The flow rate measurements aid to check a uniform distribution of lubricant into the top and the bottom film lands.

Figure 8 shows another view of the lubricant flow path through the test damper and a simple hydraulic circuit diagram. The ISO VG 2 grade lubricant, supplied through the oil inlet with flow rate Q_{in} at inlet pressure P_{in}, flows through three orifices (ϕ=2.5 mm), 120º apart, each with hydraulic resistance R_o. The central groove, at pressure P_G, fills up with lubricant and it continuously discharges to the top and bottom lands with flow rates Q_T and Q_B, respectively. After the lubricant passes through the top and bottom film lands, each with a hydraulic resistances R_T and R_B, it exits to ambient, P_a=0 bar(g).

The ISO VG 2 grade lubricant is supplied at room temperature (25 ºC) at the journal centered condition (e_s=0). In order to measure flow rate through the test rig, the inlet flow rate and at least one output flow rate (Q_T or Q_B) must be known. The oil delivery piping houses a turbine type flow meter to measure the inlet flow rate directly. Note that all air was evacuated from the oil lines prior to measurements. The outlet flow rate through the bottom land (Q_B) is determined by measuring the amount of time it takes to fill the oil collector and divided by the time to fill this region.

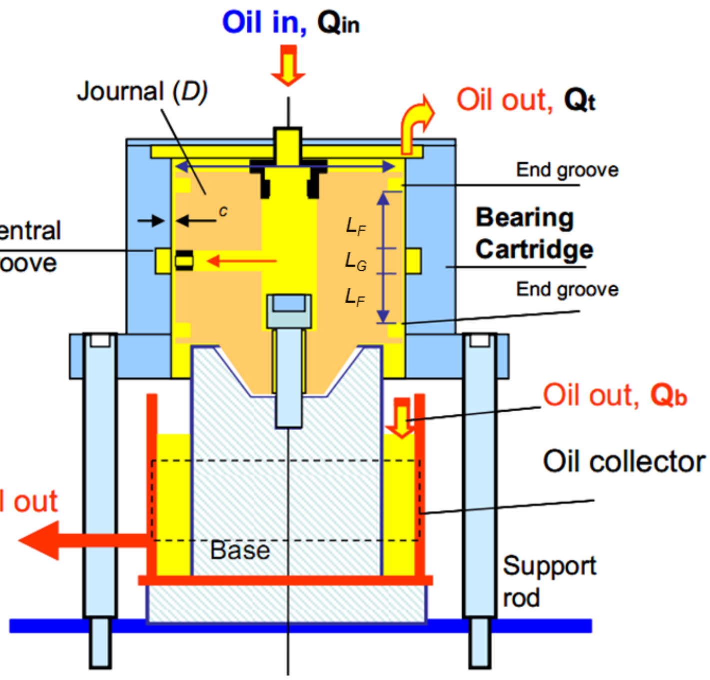

(a) Cross section view of SFD test rig and lubricant flow path through damper film [3]

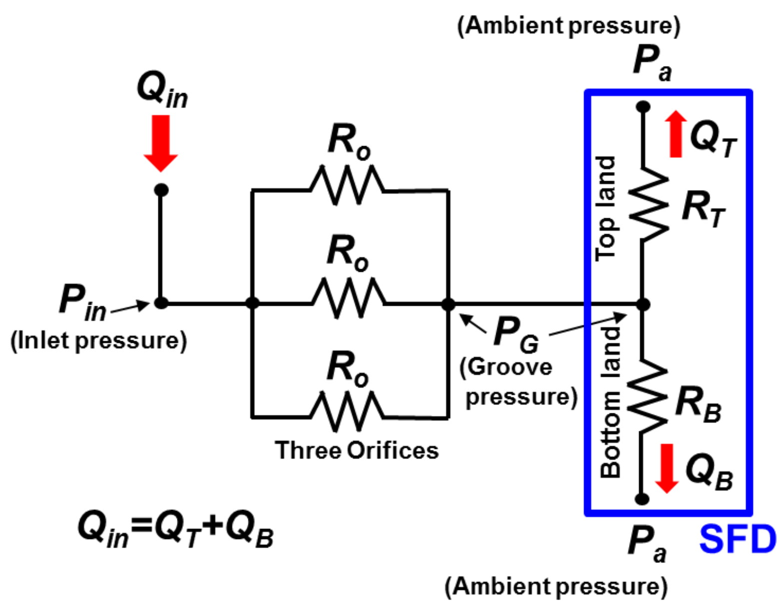

(b) Hydraulic circuit diagram for open ends SFD [5]

Fig. 8 (a) Cross section view of lubricant flow path and (b) hydraulic circuit diagram for open ends SFD.

Figure 9 shows the measured inlet flow rate (Q_{in}) and bottom land flow rate (Q_B) versus groove gauge pressure (P_G). In all cases, the bottom land outlet flow rate Q_B is ~48% of the inlet flow rate Q_{in}. The flow rate measurements show that the lubricant evenly distributes to the top and the bottom lands. Note that the measured inlet flow rate at P_G=0.09 bar(g) is 5% smaller than the value of curve fit which is within the uncertainty of measurement ~6%. Furthermore, the high correlation factor (R^2>0.99) between the measured data and curve fit indicates the adequacy of the curve fit.

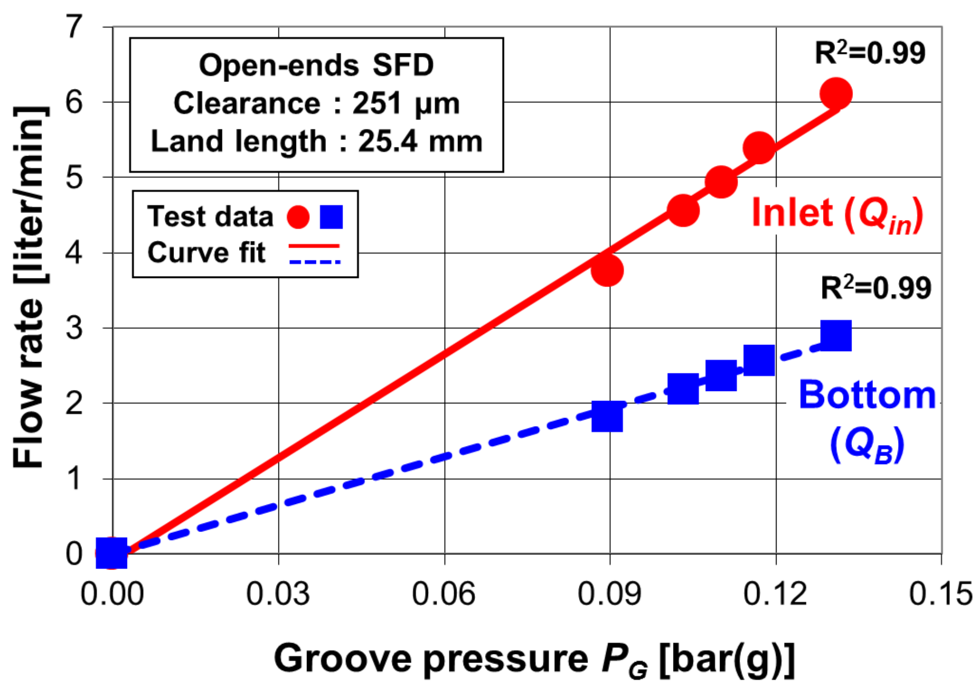

Fig.9 Oil flow rates at inlet (Q_{in}) and through bottom land (Q_B), versus static gauge pressure (P_G) recorded at the central groove.

CHAPTER V

IDENTIFICATION OF TEST STRUCTURE PARAMETER

This chapter presents the identification of the test system structure parameters $\mathbf{(K, C, M)_s}$ by performing static load tests and unidirectional dynamic load tests without oil in the film lands. The test system structural stiffness ($\mathbf{K_s}$), damping ($\mathbf{C_s}$), and residual mass ($\mathbf{M_s}$) are estimated by following the parameter identification procedure detailed in Appendix A and Ref. [38].

Before conducting static load tests, the BC weight including the weights of sensors and attachments is measured in a scale, M_{BC} ~16.4 ±0.1kg (36.1 lbm). The four main supporting rods act like cantilever beams and contribute approximately one-fourth of their masses (4 x 0.11 kg) [39]. Thus, the estimated system mass (M_{BC}) is 16.9 kg.

1. Static load tests

Figure 10 shows a top view of the set up for static load tests. The displacement sensor located 180˚ away from the static loader (45˚ apart from the X and Y axes) records the BC displacements as the static loader pulls the BC along θ=45˚. Figure 11 depicts the applied loads and the ensuing BC displacements. The slope of the load versus displacement curves shows the BC mechanical support structural stiffness ($K_{s\text{-}45}$) ~9.0 ±0.2MN/m (51.4 klb$_f$/in).

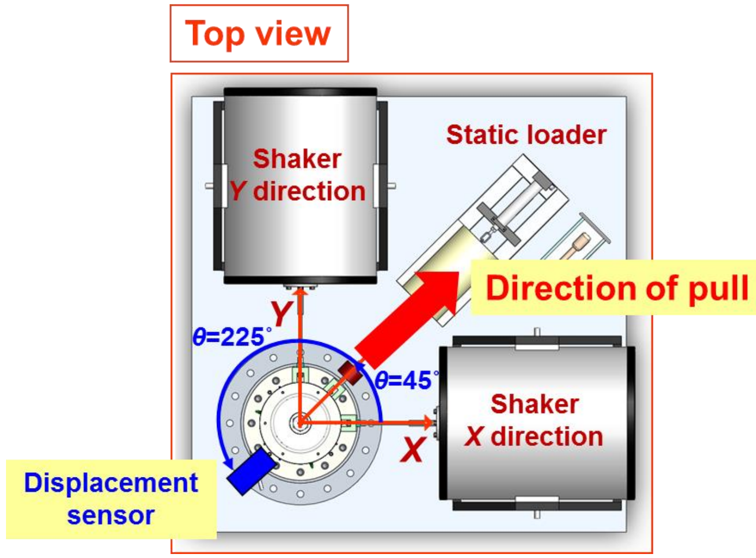

Fig.10 Schematic top view of the set up for static load tests.

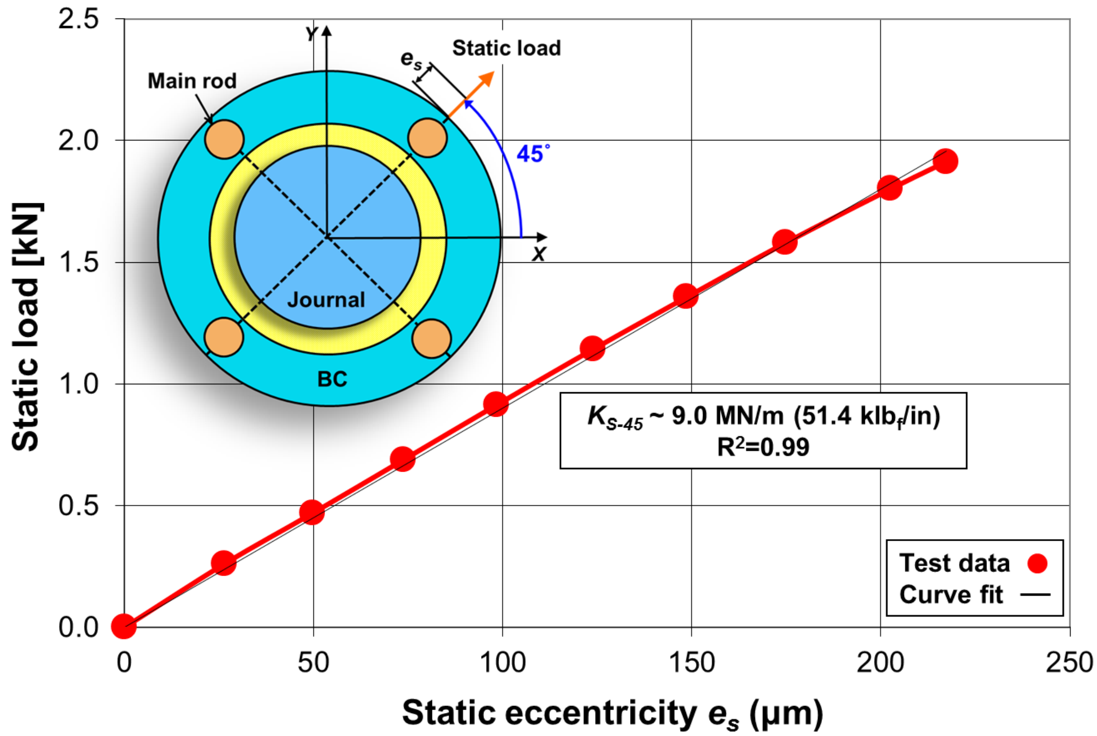

Fig.11 Applied static load versus BC-structural displacement (45°) of the bearing cartridge (four main rods). SFD nominal clearance *c*=251.5 μm.

2. Unidirectional dynamic load tests

Single frequency unidirectional dynamic load tests are carried to estimate the structural stiffness ($\mathbf{K_s}$), damping ($\mathbf{C_s}$), and residual mass ($\mathbf{M_s}$) of the dry test system. A shaker applies a single frequency periodic load along the *X*-axis, and over a frequency ranging from 10 Hz to 230 Hz. The data acquisition system records the applied force F_X and ensuing relative displacement of the BC (*X, Y).* After the tests are completed, identical tests are performed with a dynamic load along the *Y*-direction.

Figure 12 presents the magnitude of the experimentally derived flexibility functions $(G_{\alpha\beta})_{\alpha,\beta=X,Y}$ and the respective model curve fits versus excitation frequency. Note that a flexibility matrix is the inverse of the impedance matrix $\mathbf{G_s} = \mathbf{H_s}^{-1}$. The impedance matrix is $\mathbf{H_s} = \left[-\omega^2 \mathbf{M_s} + \mathbf{K_s} + i\omega \mathbf{C_s}\right]$. Note that the flexibility functions account for the BC residual mass (M_s) other than the effective mass of the BC (M_{BC}).

The structural dynamic force coefficients are identified from forced excitations spanning a frequency range from f_{start}=10 Hz to f_{end}=100 Hz. The SFD force coefficients will be estimated over an identical frequency range. Note in Figure 12 the measured flexibility functions show a near straight line over the selected frequency range because of the dominant forces from the structure with stiffness (K_s). Forces arising from the residual mass (M_s) and the structural damping (C_s) are relatively small. The magnitudes of measured cross coupled flexibility functions are close to zero, $|G_{XY}| \sim |G_{YX}| \sim 0$.

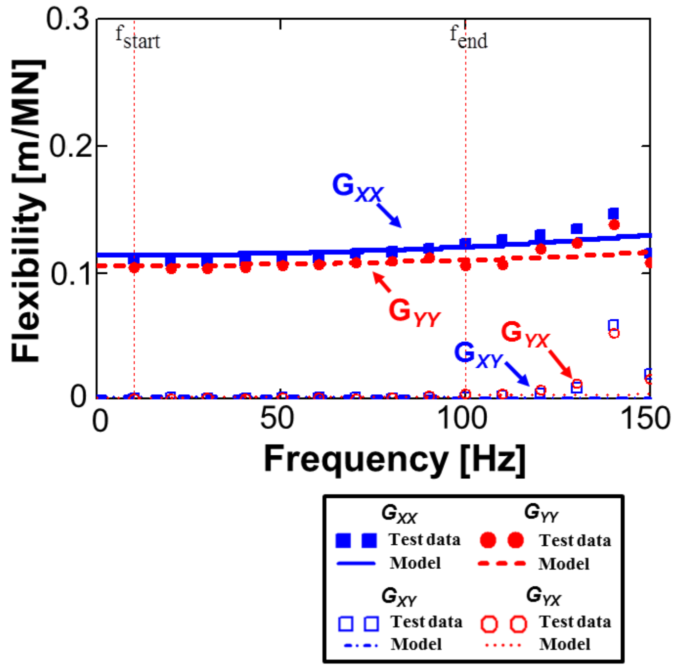

Fig.12 Dry test system: Magnitude of flexibility functions $(G_{\alpha\beta})_{\alpha,\beta=X,Y}$ versus excitation frequency. Unidirectional dynamic load tests. Test data and model fits for frequency range 10 Hz to 100 Hz.

Figure 13 presents the real and imaginary parts of the structural system impedances $(H_{\alpha\alpha})_{\alpha=X,Y}$ and the model curve fits for tests with frequencies ranging from f_{start}=10 Hz to f_{end}=100 Hz. The imaginary part of the impedance $Im(H)$ is not viscous. As a result, the correlation factor (R^2) between the test data and the physical model ($\sim C\omega$) is low.

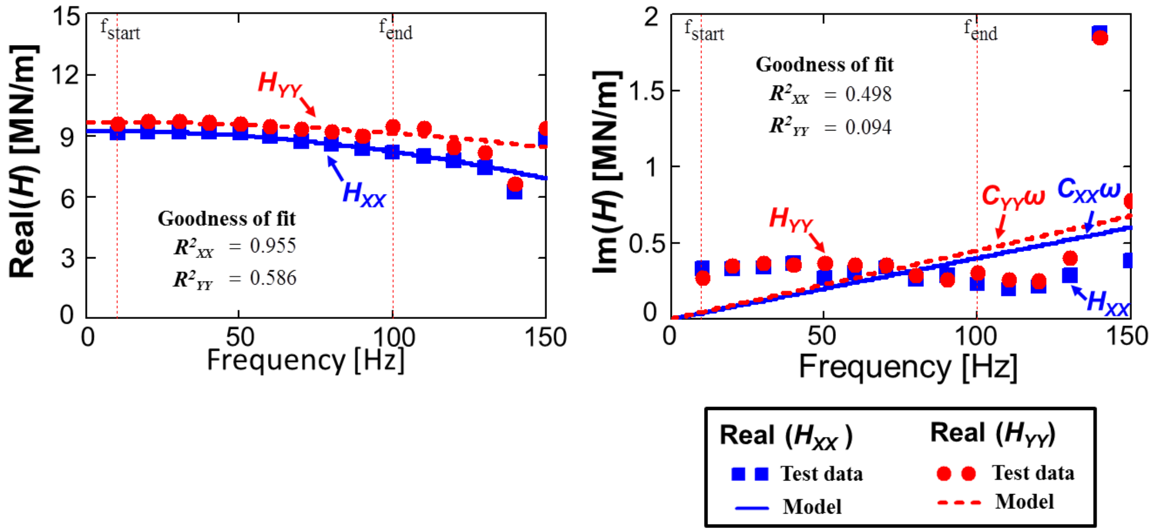

Fig. 13 Dry test system: Real and imaginary parts of the system direct impedances (H_{XX}, H_{YY}) versus excitation frequency. Unidirectional dynamic load tests. Test data and model fits for frequency range 10 Hz to 100 Hz.

Table 2 shows the identified structural force coefficients for the dry system, i.e., without oil in the film lands, as estimated by the IVF method [38] over the frequency range 10 Hz – 100 Hz. Note the effective mass (M_{BC}) is 16.3 kg (36.0 lbm) whereas the estimated M_{BC} is 16.9 kg[2]. Improved correlation between the experimental results and the physical model is shown when using[3] M_{BC}=16.3 kg as the effective mass.

The identification reveals that the test system, including the BC and four support rods, has a structural stiffness $K_{s\text{-}YY}$ 4% higher than $K_{s\text{-}XX}$ (see Table 2). Furthermore, the cross-coupled structural stiffnesses ($K_{s\text{-}XY}$, $K_{s\text{-}YX}$) are less than 1% of the direct stiffnesses. The estimated damping ratio (ζ) is ~3% or less, which is typical of a steel structure.

Also note that the structural stiffness $K_{s\text{-}45}$ estimated from static pull load tests has a 3~5% difference from that obtained with the unidirectional dynamic load tests ($K_{s\text{-}XX}$,$K_{s\text{-}YY}$). The difference between the $K_{s\text{-}45}$ and $K_{s\text{-}XX}$ is within the uncertainty range

[2] Derived from the measurement of the BC weight plus the estimation for the rods' mass contribution.
[3] Estimation of mass contribution of supporting rod is based on a simple elastic beam model [5].

(±0.2MN/m), however, the difference of the $K_{s\text{-}45}$ and $K_{s\text{-}YY}$ is not. This is most likely due to the stiffness difference of the test rig along the *X* and *Y* directions. Note that the SFD dynamic force coefficients are independent of the system structural stiffness.

Table 2. Structural parameters of dry test system derived from unidirectional load tests along *X* and *Y* directions. Parameters identified over frequency range 10 Hz – 100 Hz

Frequency range 10 - 100 Hz						
Structural parameter			**Direct**		**Cross-coupled**	
			XX	***YY***	***XY***	***YX***
Stiffness	K_s	[MN/m]	9.26 (±0.2)	9.68 (±0.2)	-0.03	-0.05
Damping	C_s	[kN.s/m]	0.64 (±0.2)	0.72 (±0.2)	0.06	-0.02
Residual mass	M_s	[kg]	2.7 (±0.7)	1.4 (±0.6)	-0.3	-0.7
System Mass	M_{BC}	[kg]	16.33			
Natural frequency	f_n	[Hz]	119.82	122.51		
Damping ratio	ξ_s		0.03	0.03		

CHAPTER VI

IDENTIFICATION OF LUBRICATED DAMPER SYSTEM PARAMETERS

This chapter details the procedure to perform circular orbit tests with a wet (lubricated) system and the test results leading to identify the SFD dynamic force coefficients $\mathbf{(K, C, M)_{SFD}}$.

1. Circular orbit tests

Multiple sets of circular orbit tests with ISO VG 2 grade lubricant were performed for seven orbit amplitudes (r=0.08c~0.71c) and four static eccentricity (e_s=0.0c~0.76c) conditions. Table 3 lists the SFD configuration, operating conditions, and the lubricant properties for the circular orbit tests with the lubricated system.

The static loader renders the centered condition (e_s=0.0c) and three static eccentricities (e_s=0.25c 0.51c, 0.76c), 45˚ away from the X and Y directions. At each static eccentric position (e_s), two shakers impose single frequency loads on the BC to produce clockwise and counter-clockwise circular orbits. Note that the shakers maximum load capacity (2,200N) limits the maximum excitation frequency to less than ~100 Hz for circular orbits with moderately large amplitudes, r/c = 0.61 and 0.71. Appendix A presents the recorded excitation forces for the circular orbit tests and ensuing journal amplitude motions and their discrete Fourier coefficients.

Table 3. Open ends SFD configuration: geometry, operating conditions and lubricant properties.

SFD configuration	
Journal diameter, D	12.7 cm (5.0 in)
Land length, L_F	2.54 cm (1.0 in)
Damper axial length (two lands + groove), $L=2L_F+L_G$	6.35 cm (2.5 in)
Radial land clearance, c	251.5 μm (9.9 mil)
Groove Axial length, L_G	1.27 cm (0.5 inch)
Groove Depth, d_G	0.96 cm (0.38 inch)
Operating conditions	
Orbit amplitude, r	0.08c - 0.71c
Static eccentricity, e_s	0.00c - 0.76c
Identification frequency range	10 - 100 Hz
Lubricant supply pressure, P_{in}	0.59 bar(g) (8.5 psig)
Groove pressure, P_G	0.12 bar(g) (1.6 psig)
Inlet flow rate, Q_{in}	5.03 LPM (1.33 GPM)
Effective mass, M_{BC}	16.3 kg (36.0 lbm)
Lubricant properties (ISO VG 2)	
Supply temperature, T_{in}	25 °C (77 °F)
Lubricant viscosity @ T_{in} , μ	2.96 cP (4.29 Reyns)
Lubricant density, ρ	785 kg/m^3 (49 lb/ft^3)
Maximum squeeze film Reynolds number (Re_s), at ω=100Hz	10.5

Figure 14 presents the amplitude of the experimental flexibility functions $(G_{\alpha\beta})_{\alpha,\beta=X,Y}$ for small amplitude BC motions r=0.08c at a centered condition (e_s=0.0c) and the physical model curve fits. Note that $\mathbf{G}=\mathbf{H}^{-1}$, where the impedance matrix $\mathbf{H}$ is $\mathbf{H}=\left[-\omega^2(\mathbf{M_{SFD}}+\mathbf{M_s})+(\mathbf{K_{SFD}}+\mathbf{K_s})+i\,\omega(\mathbf{C_{SFD}}+\mathbf{C_s})\right]$. $\mathbf{M_{SFD}}$, $\mathbf{K_{SFD}}$, and $\mathbf{C_{SFD}}$ denote the SFD added mass, stiffness, and damping matrices. The flexibility functions $G_{\alpha\beta}$ depicted include the effect of the SFD parameters $(\mathbf{K}, \mathbf{C}, \mathbf{M})_{\mathbf{SFD}}$ as well as the structural parameters $(\mathbf{K}, \mathbf{C}, \mathbf{M})_{\mathbf{s}}$. Since the effective mass of the BC (M_{BC}) is not accounted in any flexibility function G, the crests of the G functions do not evidence an actual resonance (natural frequency) of the lubricated test system.

Figure 14 (b) shows a comparison of the flexibility function estimated from a lubricated test system and the one from a dry system. At zero excitation frequency (0 Hz), the magnitude of the flexibility for the lubricated system is similar to that observed for the dry case indicating the SFD has no stiffness (K_{SFD}≈0). On the other hand, the magnitude of the lubricated system flexibility increases significantly with frequency up to 130 Hz compared to the dry system, thus evidencing a substantial amount of added mass (M_{SFD}) and damping (C_{SFD}).

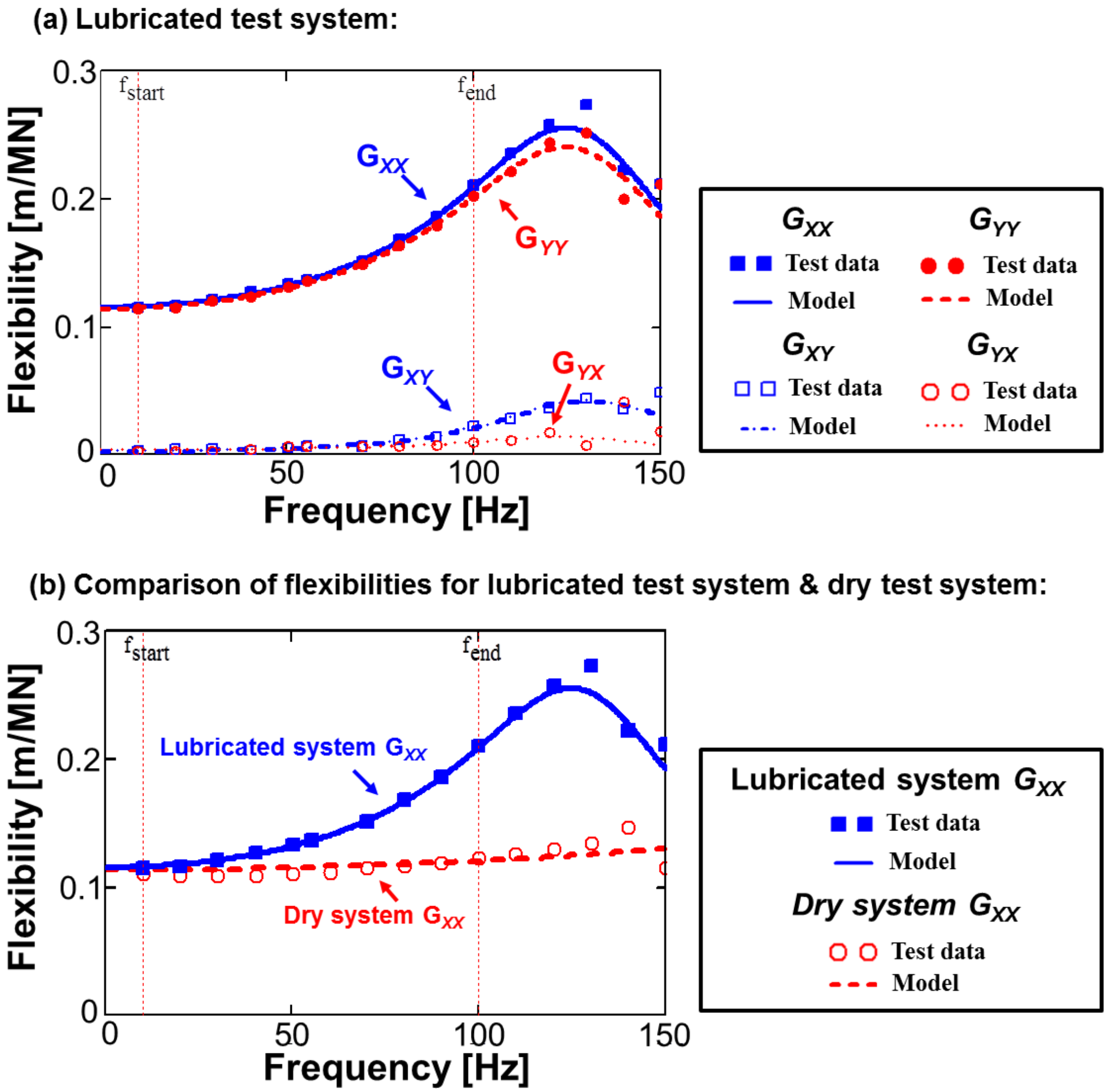

Fig.14 Lubricated test system: Magnitude of flexibility functions versus excitation frequency. (a) Lubricated test system: circular centered orbit dynamic load test with wet condition (*r/c*=0.08) and (b) Comparison of flexibilities for lubricated test system & dry test system. Test data and model fits over frequency range 10 Hz to 100 Hz.

Figure 15 presents the real part of the lubricated system impedances, Re(H), and the respective physical model curve fits over the frequency range f_{start}=10 Hz to f_{end}=100 Hz. For circular orbit amplitudes (r/c) below 50% of the film clearance, Re(H) shows high correlation factors ($R^2 > 0.95$) indicating the goodness fit between the data measured and physical model. Re(H) for the circular orbit tests with r/c=0.08 to 0.51 shows downward parabolic curves, Re(H)≅(K_s+K_{SFD})-ω^2(M_s+M_{SFD}), i.e., a positive added mass M_{SFD}. However, the Re(H) test data for CCOs with amplitudes $r/c\geq 0.6$ are virtually constant at ~8 MN/m, which imply a negligible fluid inertia effect, (M_s+M_{SFD})≈0; hence requiring of another mathematical model to estimate the physical parameters. As a result, for $r/c\geq 0.6$ the real part of the impedance is modeled as a stiffness only, i.e., $\mathrm{Re}(\mathbf{H}) = \left[\left(\mathbf{K_s} + \mathbf{K_{SFD}}\right)\right]$.

Figure 16 depicts the imaginary part of the impedance, Im(H), and the model curve fits over the frequency range 10 - 100 Hz. The imaginary part shows a constant slope for all the circular orbit tests demonstrating the SFD provides viscous damping. Furthermore, the slopes tend to increase with increasing orbit amplitudes and journal eccentricities, thus evidencing that the direct damping coefficient is a function of both the orbit amplitude (r) and the static eccentricity (e_s).

Appendix B shows the real and imaginary parts of the direct (H_{XX}, H_{YY}) and cross-coupled (H_{XY}, H_{YX}) dynamic impedances obtained from the circular orbit tests with three static eccentricity conditions (e_s=0.25c, 0.51c, and 0.76c) and with small to moderately large circular orbit amplitudes (r/c=0.08 – 0.61). Overall, the real and imaginary parts of cross-coupled dynamic impedances, Re(H_{XY}) and Im(H_{XY}), are more than one order of magnitude smaller than the corresponding Re(H_{XX}) and Im(H_{YY}). Expectedly, the respective physical model correlates poorly against Re(H_{XY}) and Im(H_{XY}).

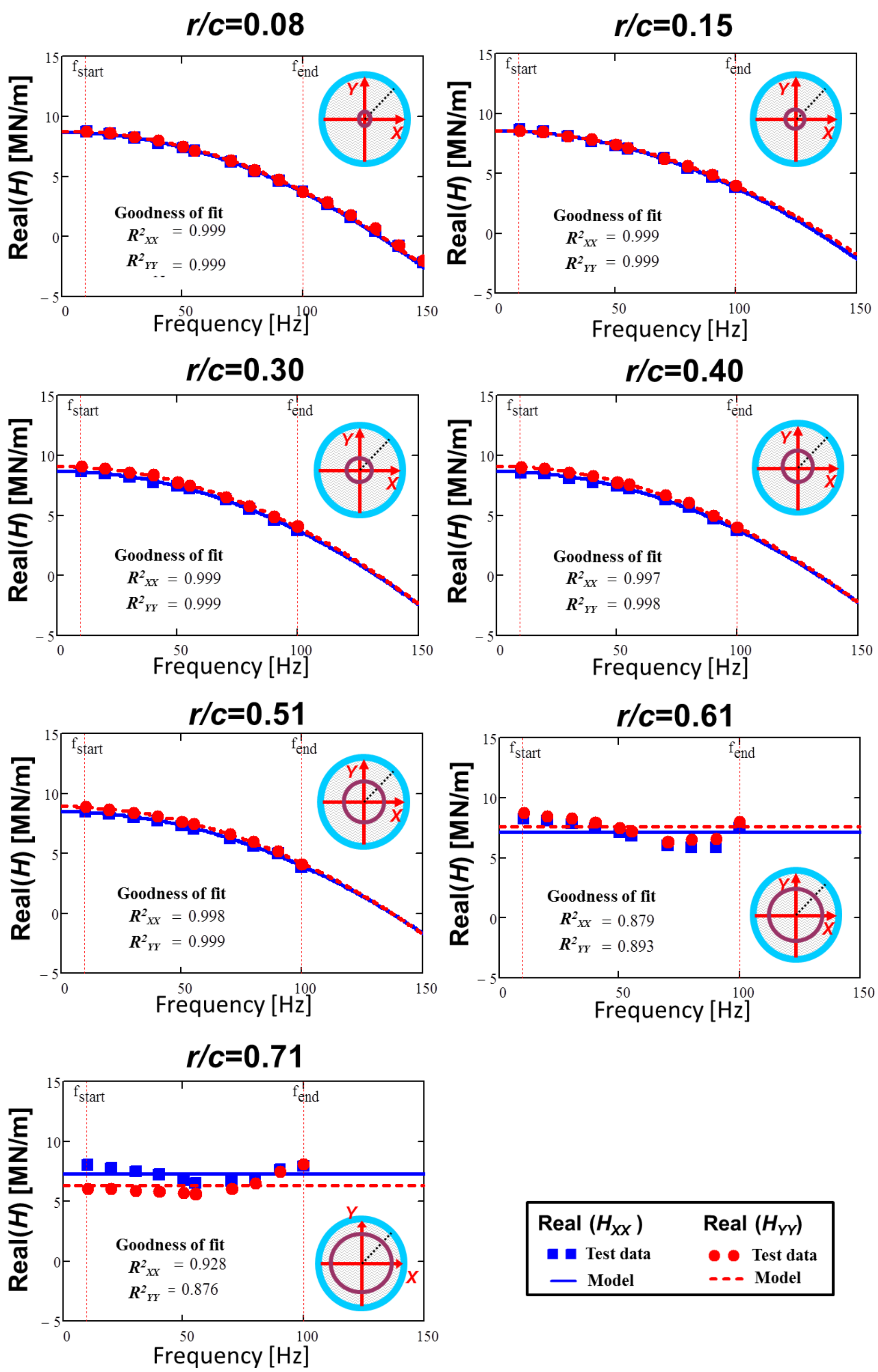

Fig.15 Real part of the test system direct impedances (H_{XX}, H_{YY}) versus excitation frequency. Tests with circular orbits with amplitudes *r/c*=0.08 - 0.71 and centered condition (e_S=0.0*c*). Test data and model fits. Open-ends grooved SFD with *c*=251.5 μm and two 25.4 mm length film lands.

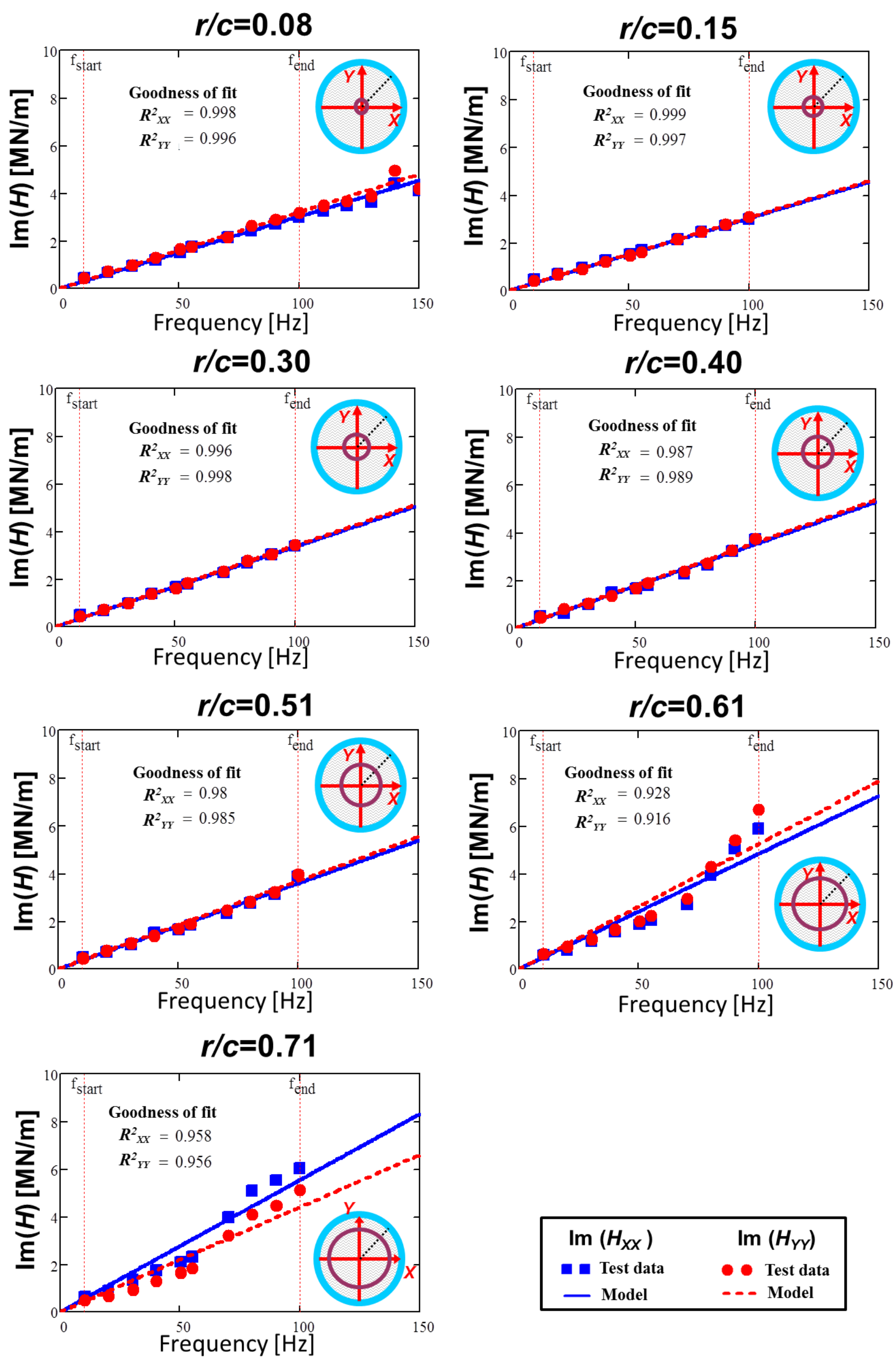

Fig.16 Imaginary part of the test system direct impedances (H_{XX}, H_{YY}) versus excitation frequency. Tests with circular orbits with amplitudes *r/c*=0.08 - 0.71 and centered condition (e_S=0.0*c*). Test data and model fits. Open-ends grooved SFD with *c*=251.5 μm and two 25.4 mm length film lands.

Figures 17 and 18 depict the identified SFD direct and cross-coupled force coefficients (damping, inertia and stiffness) obtained from the circular orbit tests for increasing orbit amplitudes (r/c) and at the centered condition (e_s = 0.0c) and three static eccentric positions (e_s = 0.25c, 0.51c, 0.76c). Note that the estimated dynamic force coefficients are valid within the specified frequency range, 10 to 100 Hz, only.

The SFD direct damping coefficients (C_{XX}, C_{YY}) remain nearly constant for orbit radii $r/c \leq 0.51$. Both C_{XX} and C_{YY} increase with the static eccentricity (e_s). For static eccentricities $e_s/c<0.51$, the cross-coupled damping coefficients (C_{XY}, C_{YX}) are at least an order of magnitude lower than the direct damping coefficients (C_{XX}, C_{YY}). Overall, the identified SFD C_{XX} and C_{YY} are more or less the same, thus evidencing an isotropic SFD. On the other hand, the SFD cross-coupled damping coefficients (C_{XY}, C_{YX}) are nearly invariant to the size of the orbit radius; albeit they increase with the static eccentricity to become as large as 40% of the direct damping at e_s/c=0.76.

The added mass coefficients (M_{XX}, M_{YY}) decrease slightly as the orbit amplitude increases up to r/c~0.51 and drop dramatically when the orbit amplitude increases above r/c~0.61. Recall that at the moderately large amplitudes, r/c=0.61 and 0.71, the SFD added masses are assumed zero based on the observation of the impedances Re(H) (see Figure 15). These added mass coefficients do increase with an increasing static journal eccentricity. At e_s/c=0.76, the fluid film added mass is as large as the mass of the BC ~17 kg. In addition, the SFD cross-coupled added masses are an order of magnitude lesser than M_{XX} and M_{YY} and increase moderately with the static eccentricity up to e_s/c~0.25. However, M_{XY} and M_{YX} quickly increase to ~20% of the direct added mass at $e_s/c \geq 0.51$.

The SFD direct stiffness coefficients (K_{XX}, K_{YY}) are nil when the orbit amplitudes (r/c) are smaller than 0.51c whereas the cross-coupled stiffness coefficients (K_{XY}, K_{YX}) are more or less zero, K_{XY}, $K_{YX} \approx 0$, for all test conditions. However, similar to the added mass coefficients, the direct stiffnesses show a notable magnitude, ~34.6% of the structural stiffness ($K_{s\text{-}XX}$, $K_{s\text{-}YY}$) for operation with large orbit amplitudes, r>0.61c. SFDs do not generate stiffness coefficients, however, the estimated SFD direct stiffness

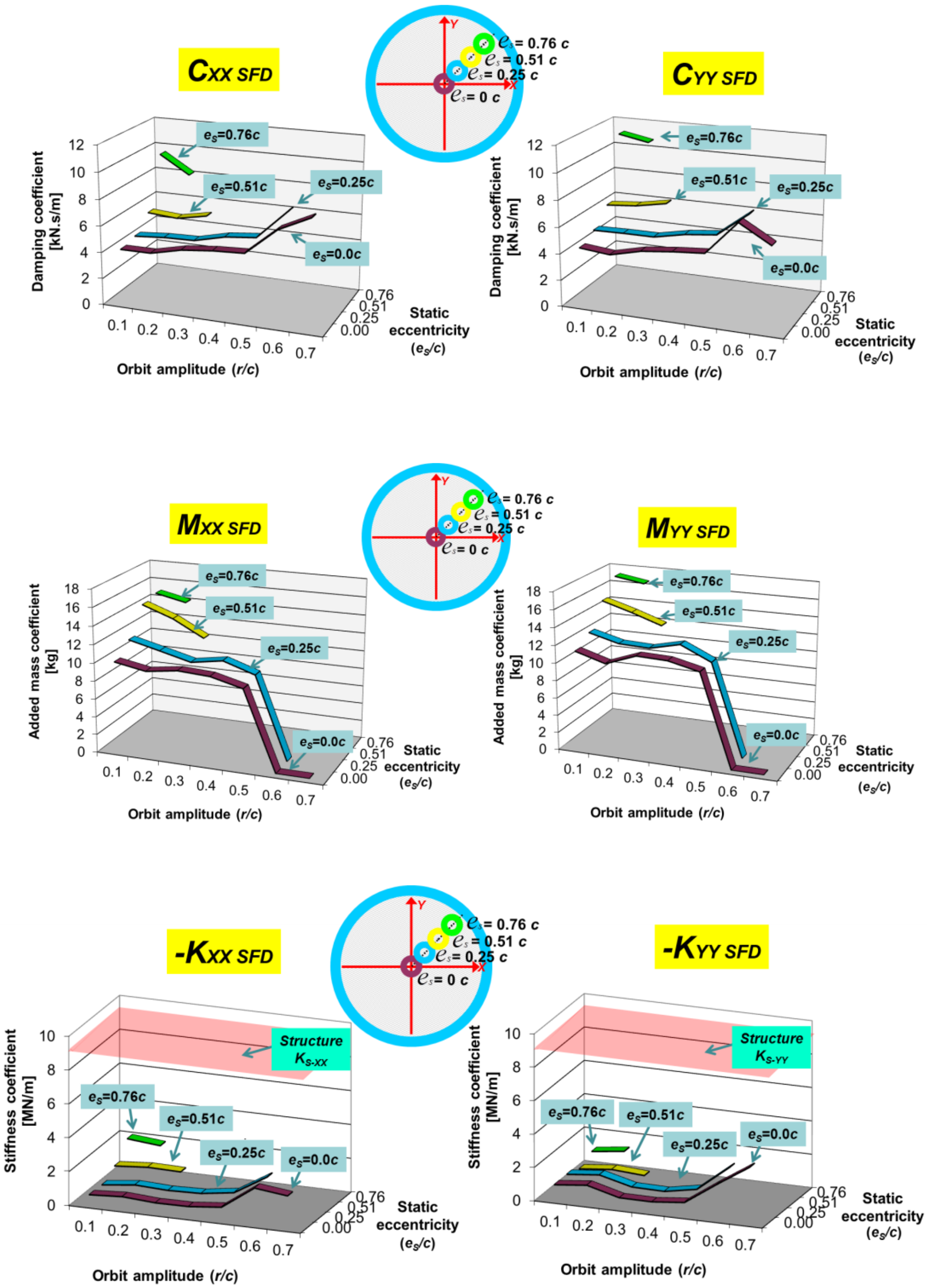

Fig.17 SFD direct dynamic force coefficients (*C, K, M*)$_{SFD}$ versus orbit amplitude (*r/c*) at the centered condition and three static eccentricities (e_s = 0*c*, e_s = 0.25*c*, e_s = 0.51*c* and e_s = 0.76*c*). Frequency range 10-100 Hz, Open-ends SFD with *c*=251.5 µm and two 25.4 mm film lands.

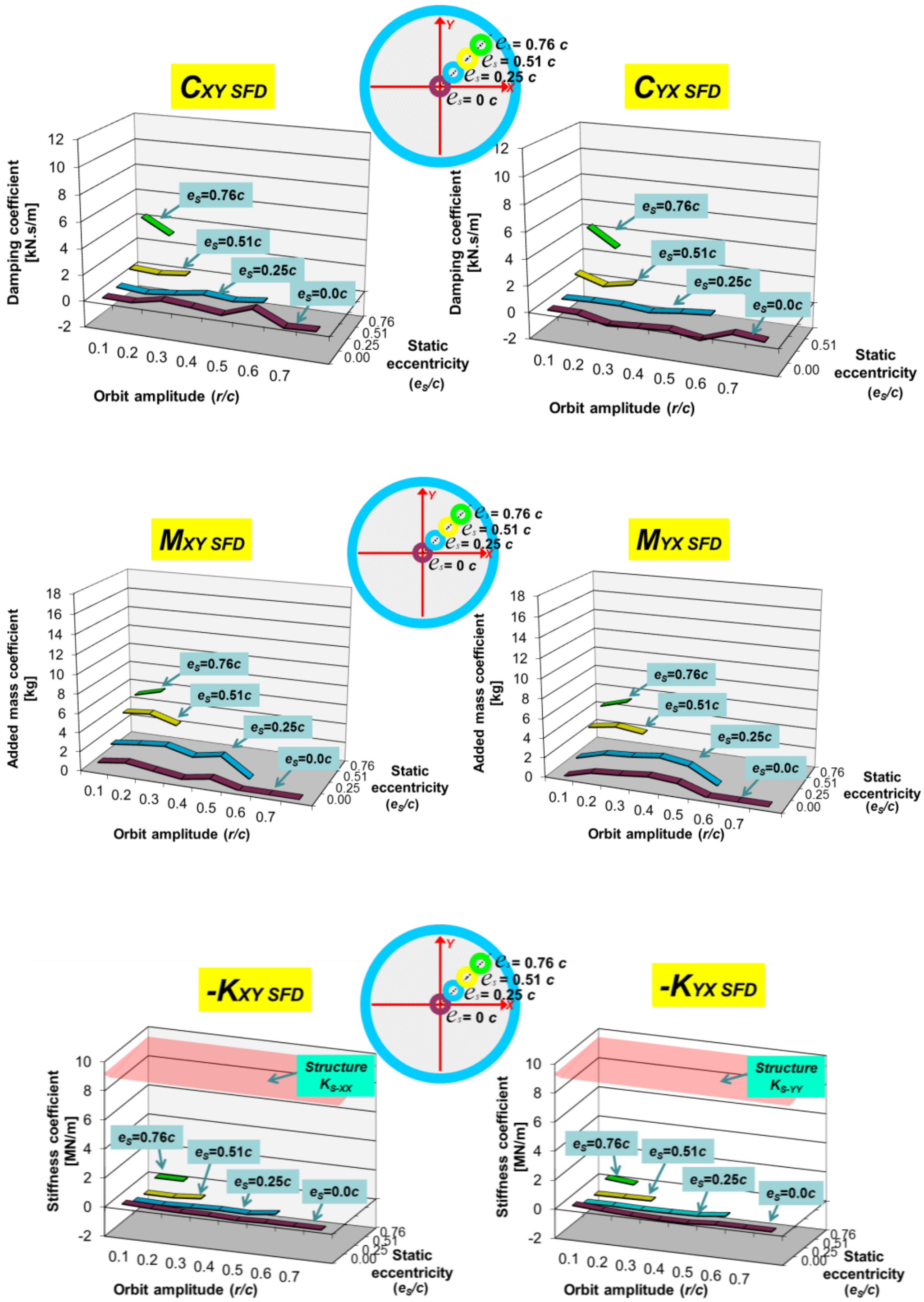

Fig.18 SFD cross-coupled dynamic force coefficients (*C, K, M*)$_{SFD}$ versus orbit amplitude (*r/c*) with centered condition and three static eccentricity (e_s = 0*c*, e_s = 0.25*c*, e_s = 0.51*c* and e_s = 0.76*c*). Frequency range 10-100 Hz, Open-ends SFD with *c*=251.5 μm and two 25.4 mm film lands.

coefficients (K_{XX}, K_{YY}) reveal themselves as a by-product of the identification process. Recall that for r/c>0.61, the identification process sets Re(H)~K as a stiffness only (mass negligible).

Prior art [4] presents the experimental SFD force coefficients for an identical SFD configuration but with a smaller nominal clearance, c_S=141 μm. The test results in Ref. [4] are compared with the current ones obtained with a radial clearance c=251 μm. Table 4 lists the distinct operating conditions for the two test SFDs.

Table 4. SFD configuration and operating conditions for two film clearances

Parameter	Large c SFD	Small c_s SFD [4]
Radial clearance	c=251 μm	c_s=141 μm
Whirl orbit amplitude, r	20 μm	14 μm
Static groove pressure, P_G	0.12 bar(g)	0.72 bar(g)
Inlet flow rate, Q_{in}	5.03 LPM	4.92 LPM
Frequency range	10-100 Hz	50-250 Hz

Figure 19 shows comparisons between the SFD direct damping and added mass estimated from both SFDs differing in clearance but with identical parrallel film land lengths and central groove. The estimated SFD direct damping (C_{XX}, C_{YY}) and added mass (M_{XX}, M_{YY}) coefficients for the small film clearance (c_s) [4] are ~4.9 and ~2.3 times larger than the coefficients obtained with a larger clearance (c) configuration, the current one. Note that based on classical lubrication theory [1], direct damping and inertia coefficients are proportional to $1/c^3$ and $1/c$, respectively.

Since both dampers have identical lengths, the theoretical ratio of direct damping and the ratio of added mass coefficients scale as $(c_s/c)^3$=5.7 and (c_s/c)=1.8, respectively. The experiments' derived ratios show a modest agreement with the theoretical ratios. The strong interaction between the film lands and the central groove may explain the differences.

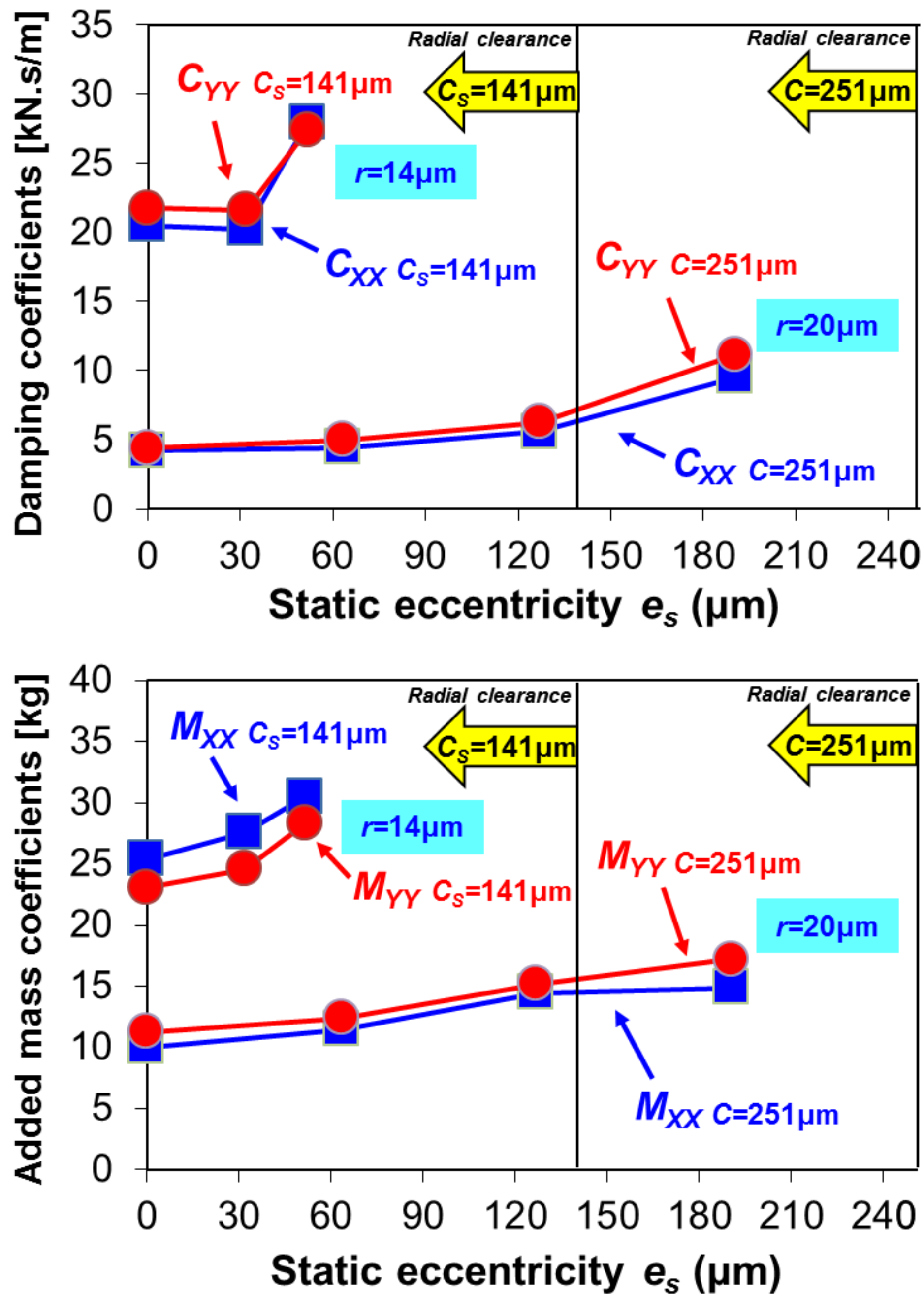

Fig.19 Open ends SFD: Comparison of direct damping $(C)_{SFD}$ and added mass $(M)_{SFD}$ mass coefficients versus static eccentricity (e_s) for amplitude with nominal clearances of c=141 μm [4] and c=251 μm. Orbit amplitudes r=14 μm and 20 μm. Damper with two 25.4 mm length film lands.

2. Effective force coefficients for circular orbit motions

Effective stiffness $(K_{i\text{-}eff})_{i=X,Y}$ and damping $(C_{i\text{-}eff})_{i=X,Y}$ coefficients for circular orbit motions are [1]

$$K_{X-eff} = K_{XX} + C_{XY}\omega - M_{XX}\omega^2 \ ; \ K_{Y-eff} = K_{YY} + C_{YX}\omega - M_{YY}\omega^2 \tag{2}$$

$$C_{X-eff} = -\frac{K_{XY}}{\omega} + C_{XX} + M_{XY}\omega \ ; \ C_{Y-eff} = -\frac{K_{YX}}{\omega} + C_{YY} + M_{YX}\omega \tag{3}$$

where $(K_{ij}, C_{ij}, M_{ij})_{i,j=X,Y}$ are the SFD stiffness, damping, and added mass coefficients, respectively.

Since the SFD shows evidence of isotropic character ($K_{XX} \approx K_{YY}$, $M_{XX} \approx M_{YY}$, etc), then average coefficients are shown below. Figure 20 shows as 3D surface plots the SFD effective stiffness and damping coefficients, $K_{avg-eff} = \frac{1}{2}\left(K_{X-eff} + K_{Y-eff}\right)$ and $C_{avg-eff} = \frac{1}{2}\left(C_{X-eff} + C_{Y-eff}\right)$, estimated from the circular orbit tests for increasing orbit amplitudes (r/c) and static eccentricities (e_s/c).

Since the damper (K_{XX}, K_{YY}) and (C_{XY}, C_{YX}) are small for $r/c \leq 0.51$ and $e_s/c=0$, the SFD effective stiffness coefficient is mainly influenced by the added mass term ($M_{XX}\omega^2$). Thus, $-K_{avg\text{-}eff}$ increases with increasing excitation frequency while remaining relatively constant with increasing orbit amplitude to $r/c \leq 0.51$. Note that a negative effective stiffness ($K_{avg\text{-}eff} < 0$) indicates an outward radial force. At the orbit amplitudes of $r/c=0.61$ and 0.71, $K_{avg\text{-}eff}$ shows invariant values throughout the excitation frequencies since an inertial effect is assumed to be negligible ($M_{SFD} \approx 0$) for circular orbit amplitudes $r/c \geq 0.6$.

The effective damping coefficient ($C_{avg\text{-}eff}$) increases with increasing orbit amplitudes (r). The effective damping coefficient shows a slight increase with excitation frequency (10 – 100 Hz) and with increasing static eccentricity due to the increase of the cross-coupled added mass term ($M_{XY}\omega$). An increase of $C_{avg\text{-}eff}$ indicates an increase of the tangential force opposing the journal whirl motion.

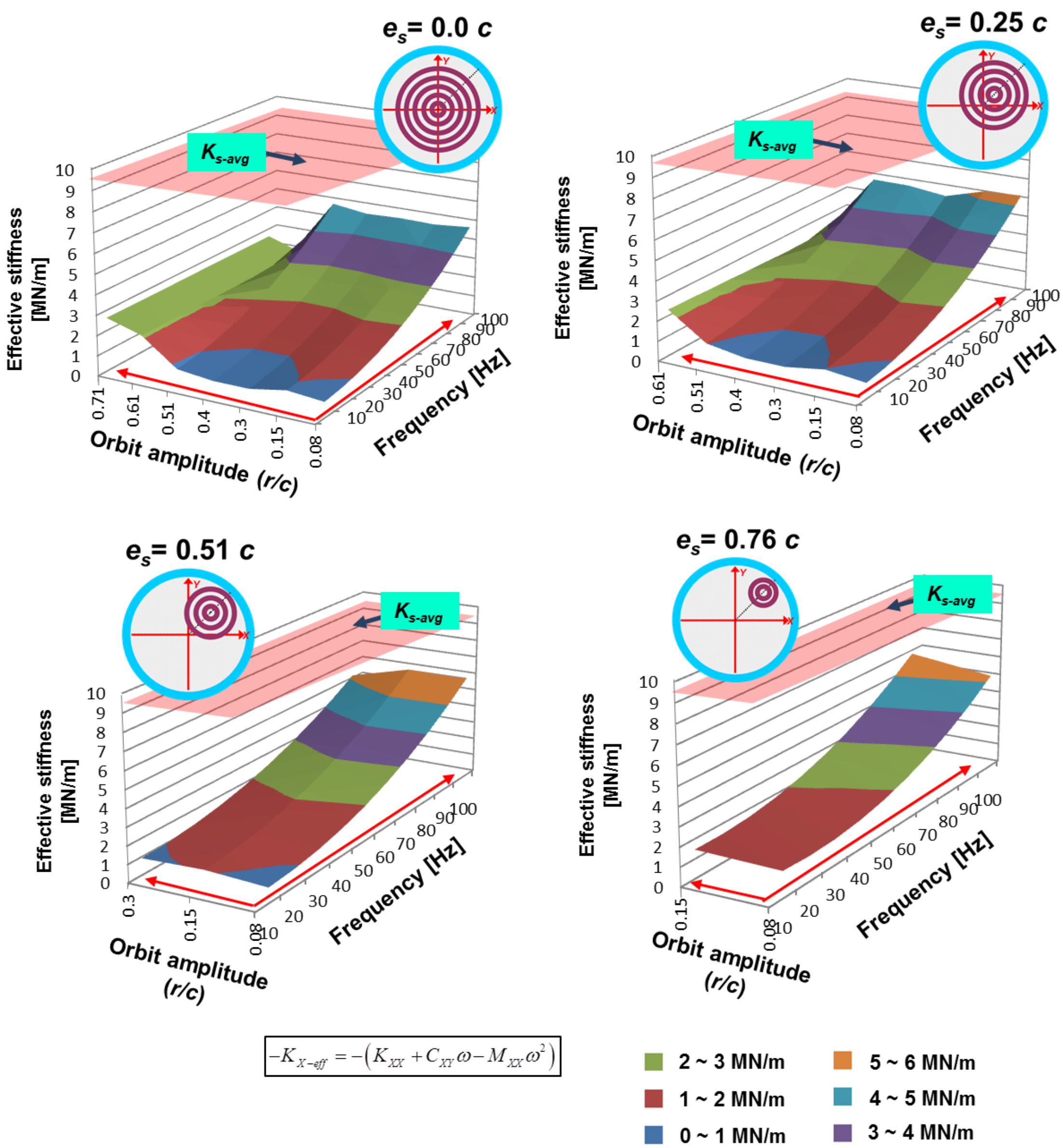

Fig. 20a SFD average effective dynamic stiffness (-$K_{avg\text{-}eff}$) coefficient versus orbit amplitude (*r/c*) at the centered condition and three static eccentricities (e_s = 0.0*c*, e_s = 0.25*c*, e_s = 0.51*c* and e_s = 0.76*c*) and excitation frequency ranging from 10 to 100 Hz, Open-ends SFD with *c*=251.5 μm and two 25.4 mm film lands.

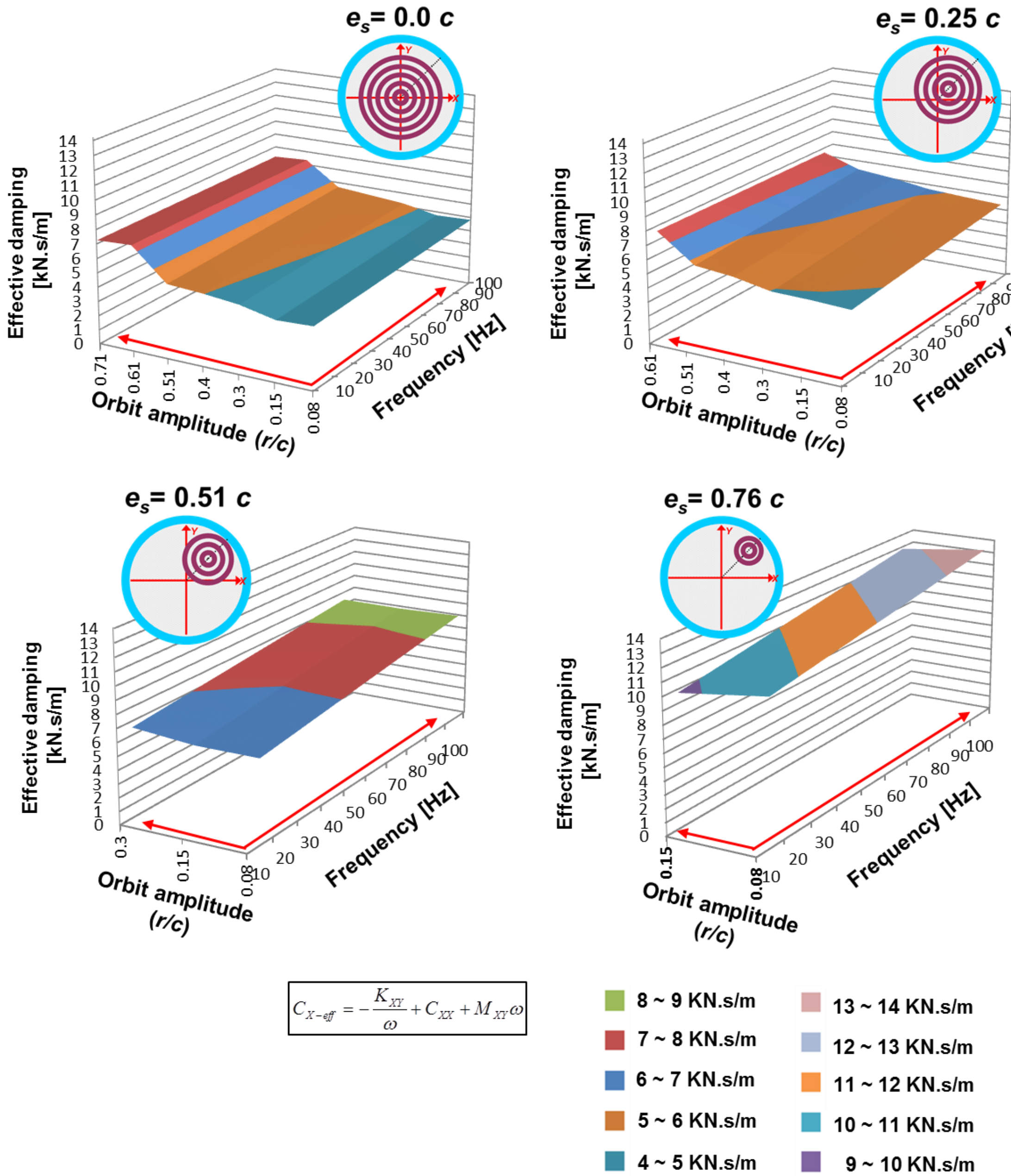

Fig. 20b SFD average effective damping ($C_{avg\text{-}eff}$) coefficient versus orbit amplitude (r/c) at the centered condition and three static eccentricities ($e_s = 0.0c$, $e_s = 0.25c$, $e_s = 0.51c$ and $e_s = 0.76c$) and excitation frequency ranging from 10 to 100 Hz, Open-ends SFD with c=251.5 μm and two 25.4 mm film lands.

CHAPTER VII

MEASUREMENT OF DYNAMIC PRESSURES IN THE DAMPER FILM LANDS AND IN THE CENTRAL GROOVE

This chapter presents the measured dynamic pressure profiles in the film lands and in the central groove recorded during test with circular orbit motions. Figure 21 and 22 depict the disposition of six piezoelectric dynamic pressure sensors on the circumferential positions θ=120°, 165°, 240°, and 285° estimated counter-clockwise from the X-axis. A pair of pressure sensors, positioned at 120°, is installed in the top and bottom film lands at the half way of its axial length, ½ L_F. Another pair of sensors, positioned at θ=240°, measures the dynamic pressure in the film lands as well. Two sensors located at the central groove (θ=165°, 285°), 120° apart, measure dynamic pressures in the central groove. Recall that all the pressure sensor tips are flushed with the BC inner surface to ensure a smooth surface.

In all measurements with circular orbits of increasing amplitude (r) and static eccentricities (e_s/c), the lubricant flow rate is set to 5.03 LPM (1.33 GPM) maintaining a lubricant supply pressure P_{in} to 0.59 bar(g) (8.5 psig) and a groove pressure P_G of ~0.12 bar(g) (1.6 psig). Note that the friction forces (hydraulic resistance R_o) on the lubricant through flow path and discharge of a lubricant into the central groove may be the main reason[4] for a static pressure drop from P_{in}=0.59 bar(g) to P_G =0.12 bar(g) (see Figure 8).

---

[4] Currently, a physics based explanation for the large static pressure drop, ΔP~0.47 bar(g), is not available.

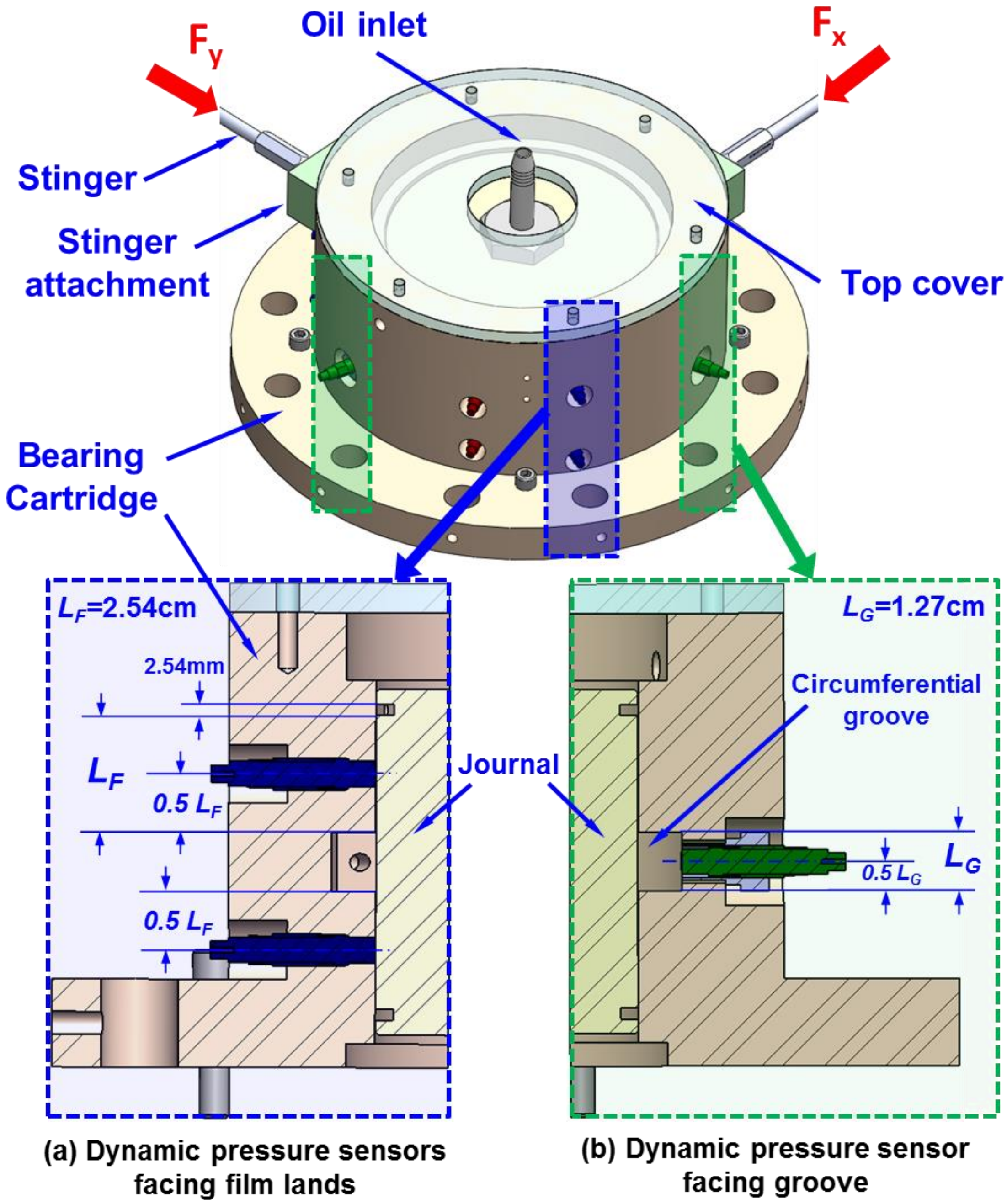

Fig. 21 Location of dynamic pressure sensors in the BC. Cross-section view of pressure sensor dispositions at (a) two film lands and (b) central groove.

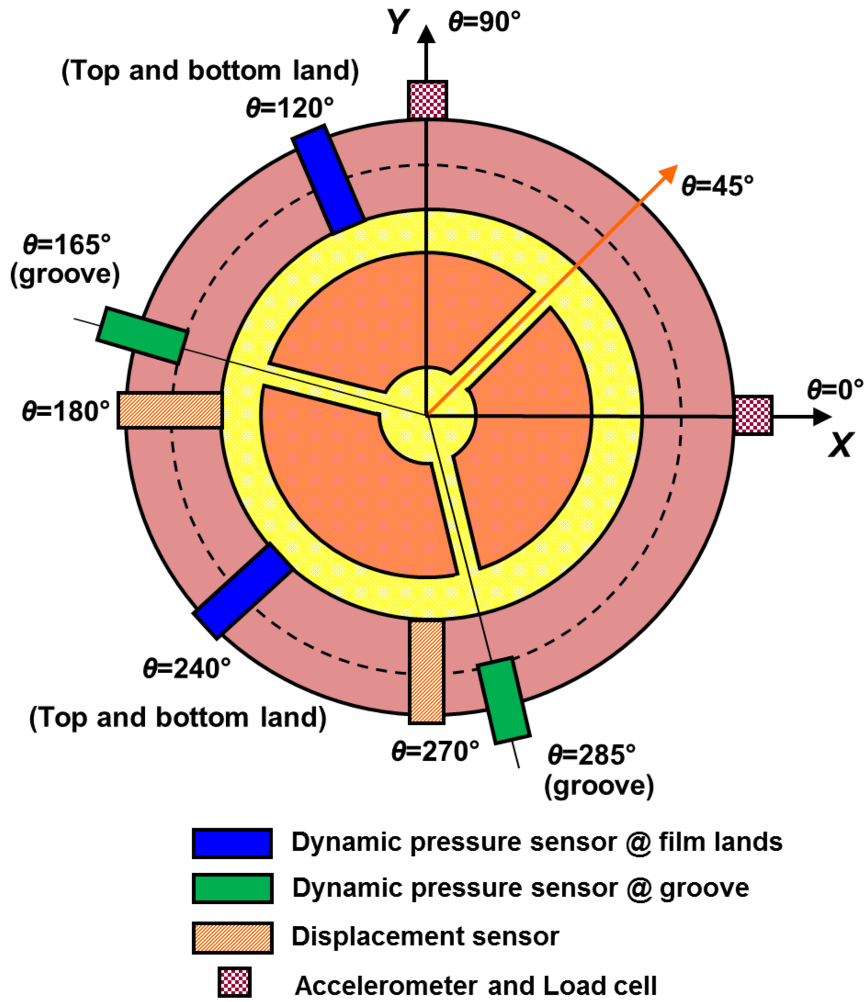

Fig. 22 Schematic view of disposition of dynamic pressure sensors, displacement sensors, accelerometer and load cell in the BC (exaggerated clearance for illustrative purpose.

Figure 23 shows the measured dynamic peak-to-peak (p-p) pressures in the feed groove and in the film lands for circular centered orbit tests with increasing orbit radii (r/c=0.08 to 0.71). Both film lands and groove p-p pressures increase with increasing orbit amplitudes. Clearly, the groove pressures (165°, 285°) are not nil, showing the same order of magnitude as the dynamic pressures in the film lands at θ=120°. The magnitude of the dynamic pressure in the top film land are lesser than those in the bottom film land. The difference indicates the journal and the BC may not have been perfectly aligned.

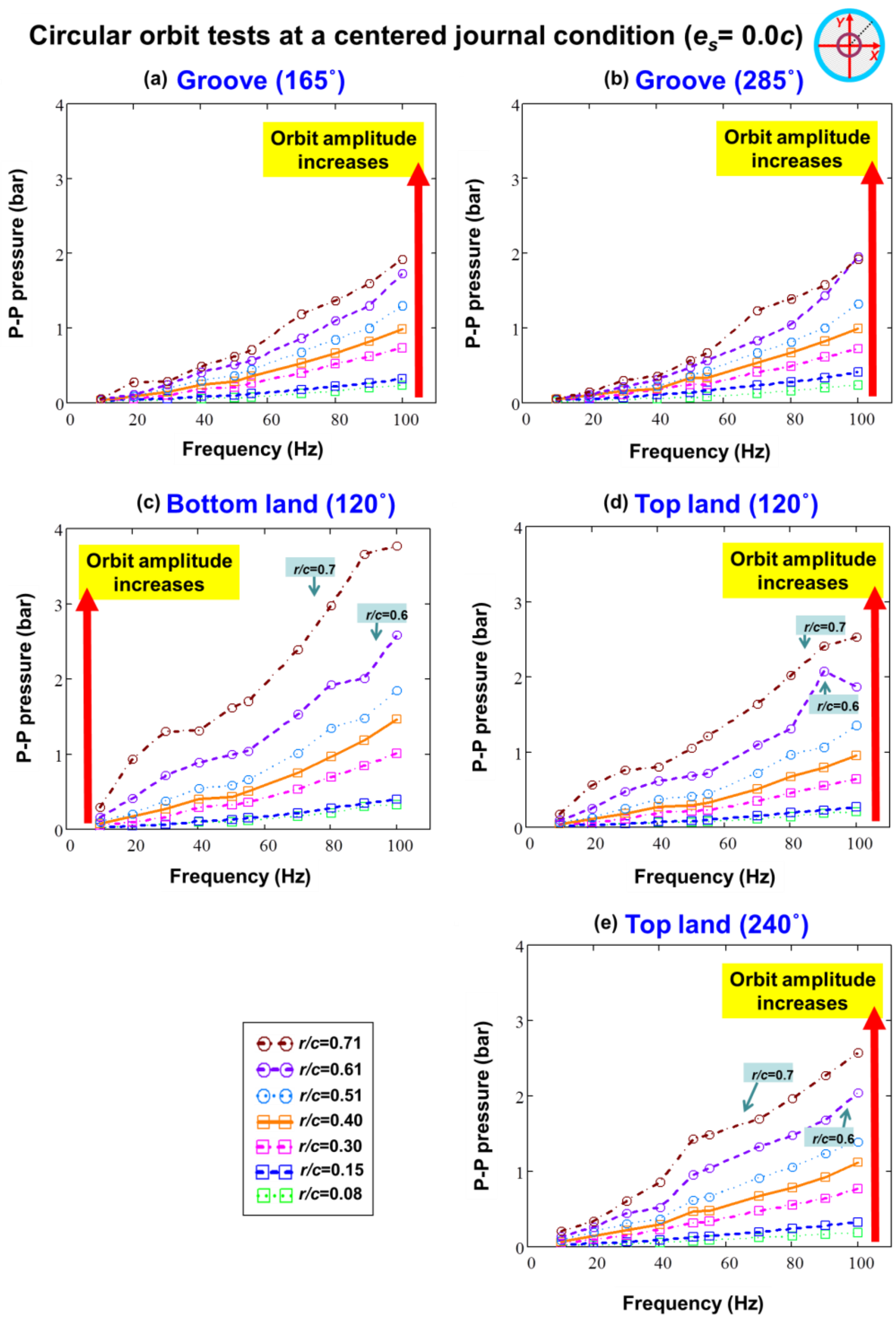

Fig. 23 Peak-peak dynamic pressures versus excitation frequency. Tests with circular centered (e_S=0) orbit amplitudes r=0.08c to r=0.71c: at (a) groove (165˚), (b) groove (285˚), (c) bottom film lands (120˚), (d) top film lands (120˚), and (e) Top land (240°). Open-ends SFD with c=251.5 μm and two 125.4 mm length film lands.

Figure 24 shows the pressure profiles in the groove and the film lands at a whirl frequency 100 Hz for circular orbit tests with orbit radii r/c=0.08 – 0.71 and at the centered condition (e_s/c=0.0). Clearly, the magnitude of the dynamic pressures in the groove as well as in the film lands increases with an increasing in orbit amplitude. Note that the groove pressures at 165° and 285° show identical magnitudes. The measured dynamic pressures show a single frequency waveform until the orbit amplitude reaches r=0.51c. For larger orbit amplitudes, r>0.61c, the pressure waveforms show both sudden spikes and a flat zone. The fluctuations are not perceivable for small amplitudes of motion (r<0.51c). In general, the amplitude of the lubricant dynamic pressure in the deep groove pressure is lower (yet significant) than in the film lands.

Figure 25 depicts the measured squeeze film dynamic pressures in the bottom film land (120°) at a whirl frequency of 100 Hz for a CCO with r/c=0.61. The solid and dash lines indicate the dynamic pressures and the dimensionless film thicknesses (h/c) during three periods of journal whirl motion, respectively. As the film thickness increases, a negative dynamic pressure drags air into the film land. As a result, a mixture of air and oil evolves in the film land and the compressibility of the ensuing air-oil mixture renders a *flat* pressure zone during a fraction of the squeeze motion of the journal (when there is decrease in film thickness). As explained in Refs [27,28,31], the *flat* zone in the dynamic pressure indicates air entrainment, in particular, when an abrupt increase of pressure due to the collapse of air bubbles is observed immediately after. Incidentally, differences in pressure profiles are noticeable between consecutive periods of whirl motion.

Figure 26 shows waterfall plots of the dynamic pressures in the bottom film land versus time with amplitudes ranging from r=0.08c to r=0.71c at a whirl frequency of 100 Hz. Clearly, the onset of uniform pressure zone is observed at orbit amplitude r/c=0.61. This zone increases with an increasing orbit amplitude.

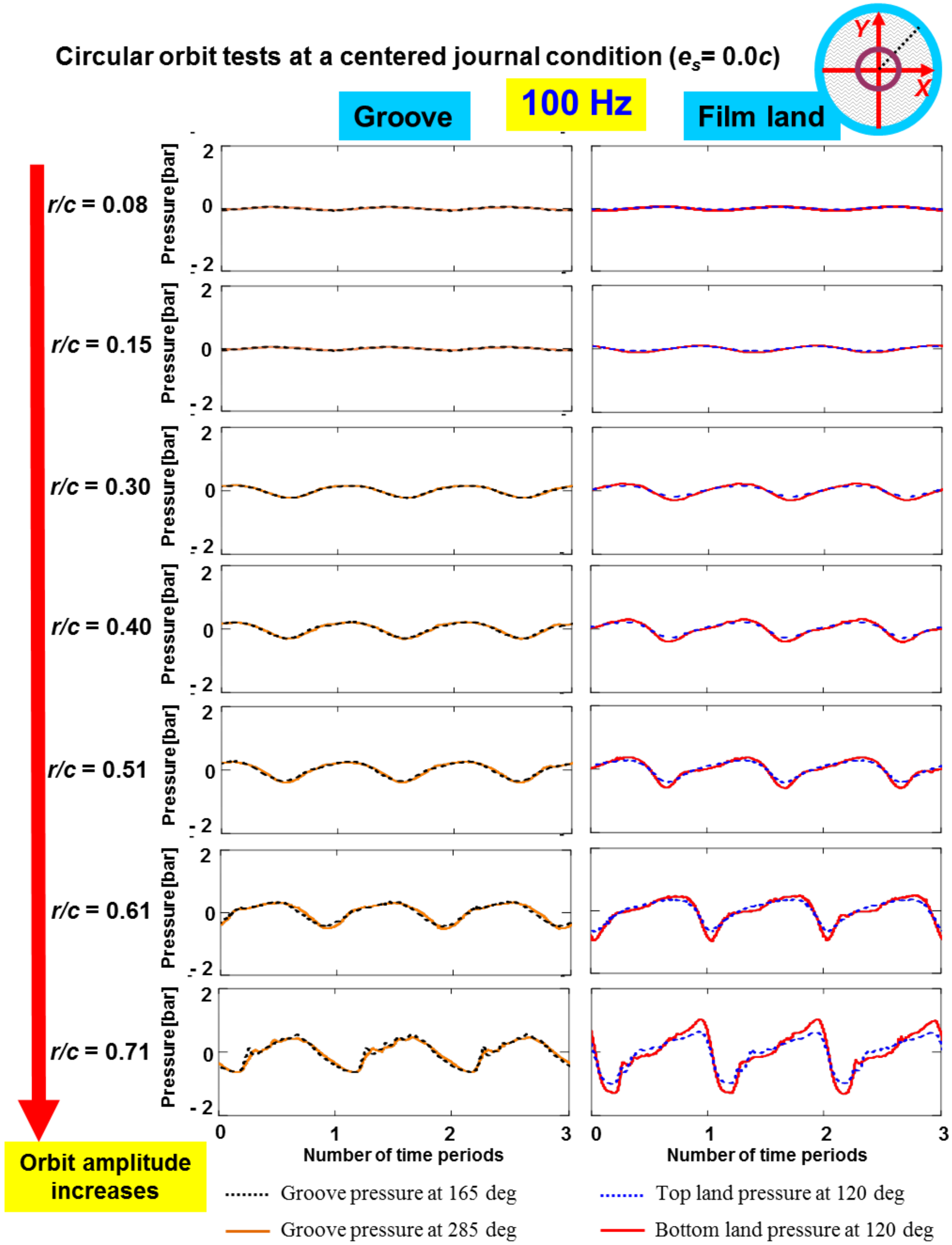

Fig. 24 Measured dynamic pressures in the groove and the thin film lands versus number of time periods. Tests with circular centered (e_S=0) orbit, amplitudes r=0.08c to r=0.71c at a whirl frequency 100 Hz. Open-ends SFD with c=251.5 μm and two 25.4 mm length film lands.

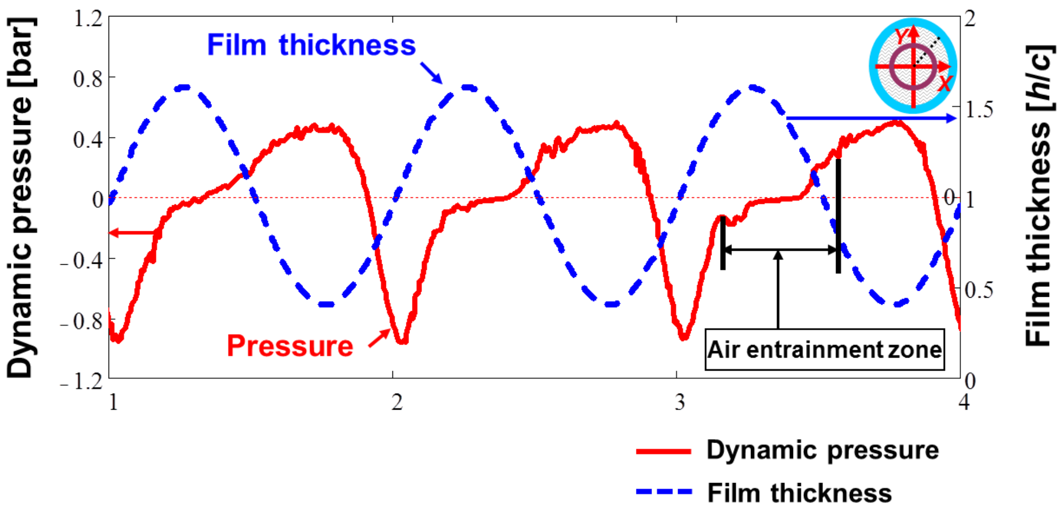

Fig. 25 Dynamic pressure and dimensionless film thickness (*h/c*) versus time periods. Test with circular centered (e_S=0.0*c*) orbit amplitude *r/c*=0.61 at a whirl frequency of 100 Hz. Measurement at bottom land (120°). Open-ends SFD with *c*=251.5 μm and two 25.4 mm length film lands.

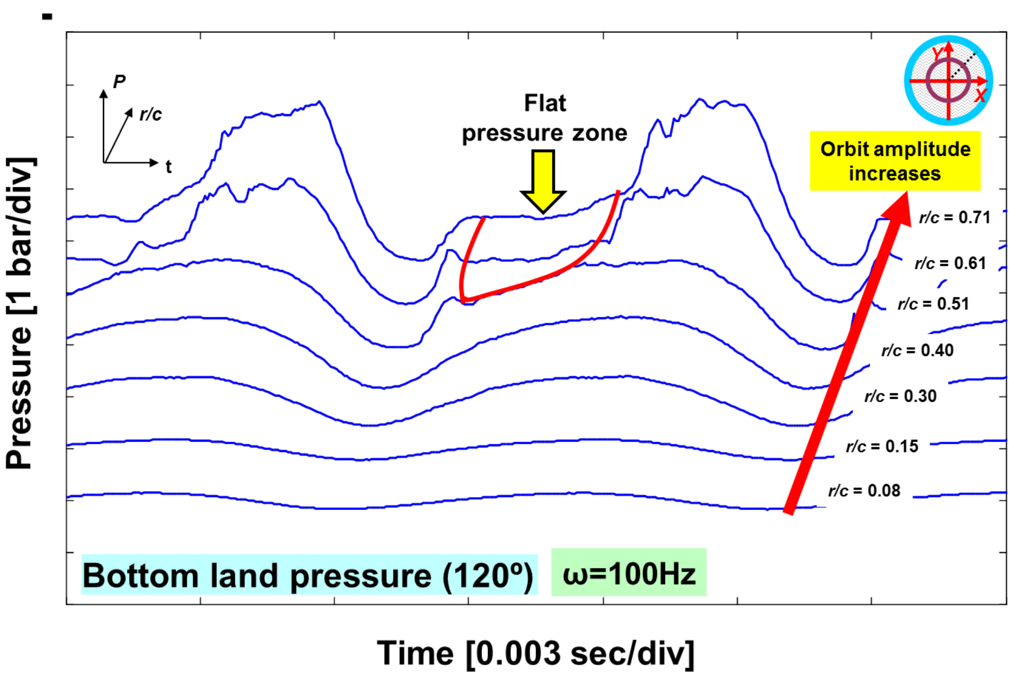

Fig. 26 Waterfall-like plot of lubricant dynamic pressures in the film lands versus time period. Tests with circular centered (e_S=0.0*c*) orbit amplitudes *r/c*=0.08 to 0.71 at a whirl frequency of 100 Hz. Measurement at bottom lands (120°). Open-ends SFD with *c*=251.5 μm and two 25.4 mm length film lands.

The SFD dynamic pressure can be construed as the superposition into contribution of fluid viscous and inertia effects. The fluid viscous and inertial contributions of the dynamic pressure are proportional to the whirl frequency and whirl frequency square, respectively. Thus, peak-to-peak (p-p) dynamic pressure could be expressed as

$$P_{p-p} \cong \underbrace{a\omega}_{\text{Viscous}} + \underbrace{b\omega^2}_{\text{Inertial}} \tag{4}$$

where a and b are the constants.

To better understand the evolution of the film dynamic pressures, consider a normalized pressure based on classical (viscous) lubrication theory by eliminating the contribution of lubricant viscosity μ, circular orbit amplitude r and whirl frequency ω [40]

$$\overline{P} = \frac{P}{P^*} = \frac{P}{6\mu\omega\overline{r}\left(\frac{L}{c}\right)^2\left(1-\overline{r}^2\right)^{-\frac{3}{2}}} \tag{5}$$

where $\overline{r}$ $=r/c$ is denoted a dimensionless orbit radius. Now, the normalized p-p dynamic pressures $\overline{P}$ could be expressed as

$$\overline{P} \cong \underbrace{g}_{\text{Viscous}} + \underbrace{q\omega}_{\text{Inertial}} = \overline{P}_{viscous} + \overline{P}_{inertial} \tag{6}$$

where g and q are the constants.

Figure 27 reproduces data in Figure 23 by plotting the pressures $\overline{P}$ versus excitation frequency for circular orbit tests with r/c=0.08 to 0.71. The results show that the p-p $\overline{P}$ in the grooves (165˚, 285˚) increases with an increasing excitation frequency (ω). More specifically, $\overline{P}$ is proportional to the whirl frequency ($\overline{P}$ ~ω). Importantly enough, at each whirl frequency, the magnitudes of the normalized pressures at the groove throughout the circular orbit tests r/c=0.08 – 0.71 reveal more or less the same range value. In other words, the normalized pressures converge to a line with the same slope regardless of the orbit size. This trend indicates that the dynamic pressures in the groove (d_G = 38c) are mainly affected by contribution of fluid inertia rather than viscous effects.

A relatively large $\overline{P}$ at low frequencies ($\omega \leq 20$ Hz) is of minor importance, since the actual p-p pressures are small (see Figure 24).

Likewise, the normalized pressures $\overline{P}$ at the film lands (120˚, 240˚) tend to converge to a unique slope for circular orbit amplitudes $r/c<0.5$; albeit $\overline{P}$ shows a slight increase with increasing orbit amplitude. Pressures $\overline{P}$'s measured at the film lands (120˚, 240˚) show a large deviation from a single slope for $r/c>0.61$. A deviation of $\overline{P}$ from a single slope line indicates that the contribution of fluid viscous $(\overline{P}_{viscous})$ on dynamic pressure increases with increasing orbit amplitude and thus resulting in a large increase of viscous damping for $r/c>0.61$ (see Figure 17).

In general, the magnitude of the normalized pressures at the bottom film land are higher than those at the top film land. The reasoning behind the difference is a slight unevenness of the damper clearance at the location 120˚. That is, the bottom land film clearance is slightly smaller than at the top; thus generating higher dynamic pressures. The magnitudes of the normalized pressures measured at the top land at locations 120˚ and 240˚ are similar except at whirl frequencies from 10 Hz to 30 Hz.

Appendix C shows the peak-to-peak dynamic pressures and normalized pressures $\overline{P}$ for the CCO tests with three static eccentricities $e_s=0.25c$, $0.51c$, and $0.76c$. The pressure profiles at the three static eccentricities also show similar trends as with those found at the centered condition, i.e., a pronounced fluid inertia effect in the groove dynamic pressure and distinct fluid viscous and inertia effects in the film lands.

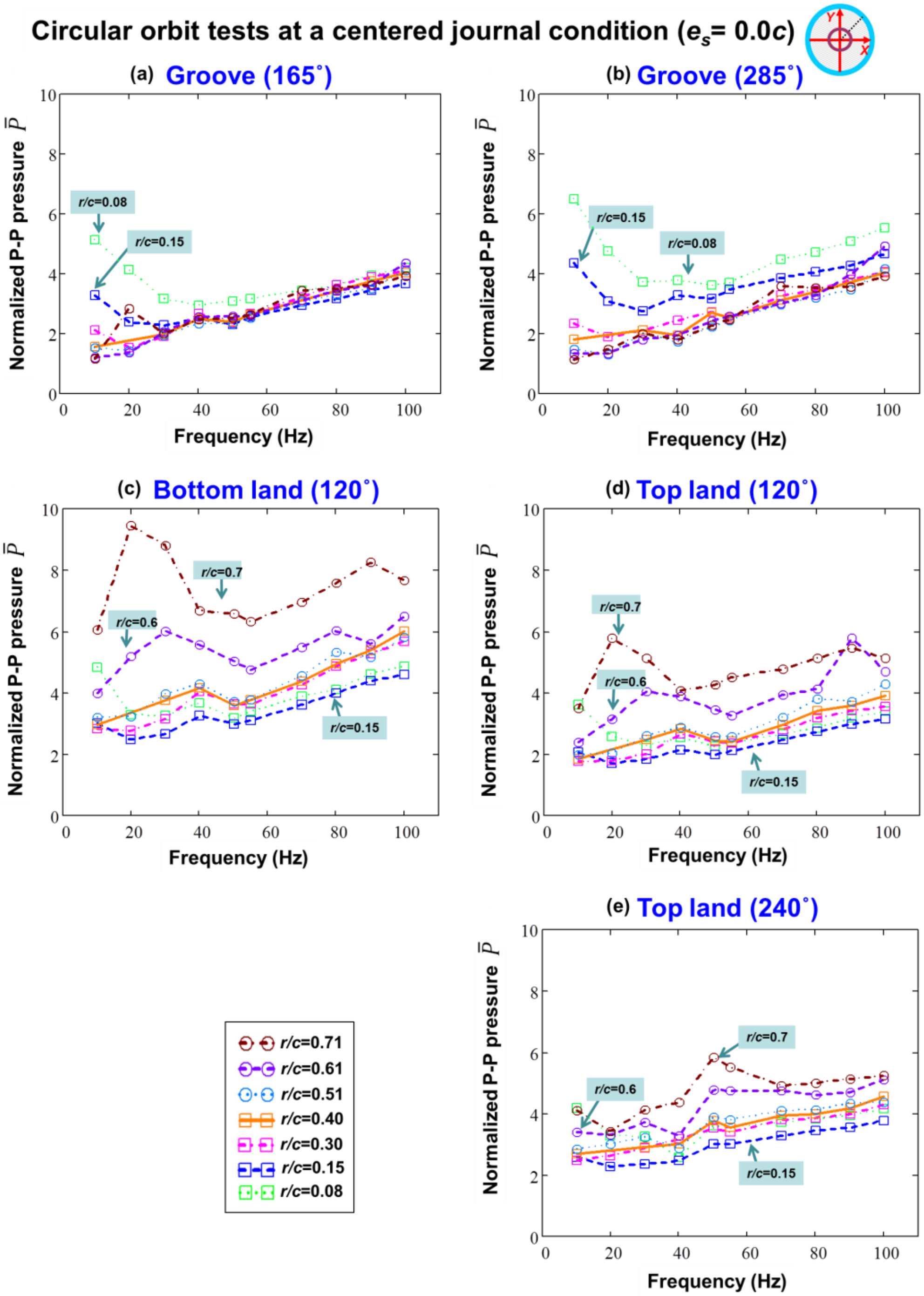

Fig. 27 Normalized peak-to-peak dynamic pressures versus whirl frequency ranging 10 – 100 Hz. Tests with circular centered (e_S=0.0c) orbit amplitudes r=0.08c to r=0.71c: at (a) Groove (165°), (b) Groove (285°), (c) Bottom land (120°), (d) Top land (120°), and (e) Top land (240°). Open-ends SFD with c=251.5 μm and two 25.4 mm length film lands.

CHAPTER VIII

COMPARISON BETWEEN EXPERIMENTAL RESULTS AND PREDICTION

This chapter presents a comparison between the experimentally identified dynamic force coefficients and predictions based on a computational physical program developed by San Andrés [41].

Figure 28 shows a schematic view of a SFD geometry noting the SFD coordinates. The center of the BC and the journal are denoted as O_B and O_J, respectively. The fixed coordinate Θ is the sum of attitude angle ϕ and the relative θ, i.e., $\Theta = \phi + \theta$. The attitude angle $\phi = \omega t$ is goes through the BC center (O_B) and the journal center (O_J), which also passes through the maximum and minimum film thickness. Note that the origin of the relative angular coordinate θ is located at the maximum film thickness. Furthermore, the distance between the BC center (O_B) and the journal center (O_J) is termed as the static journal eccentricity e_s, and the dynamic eccentricity (journal orbit amplitude) is denoted as r.

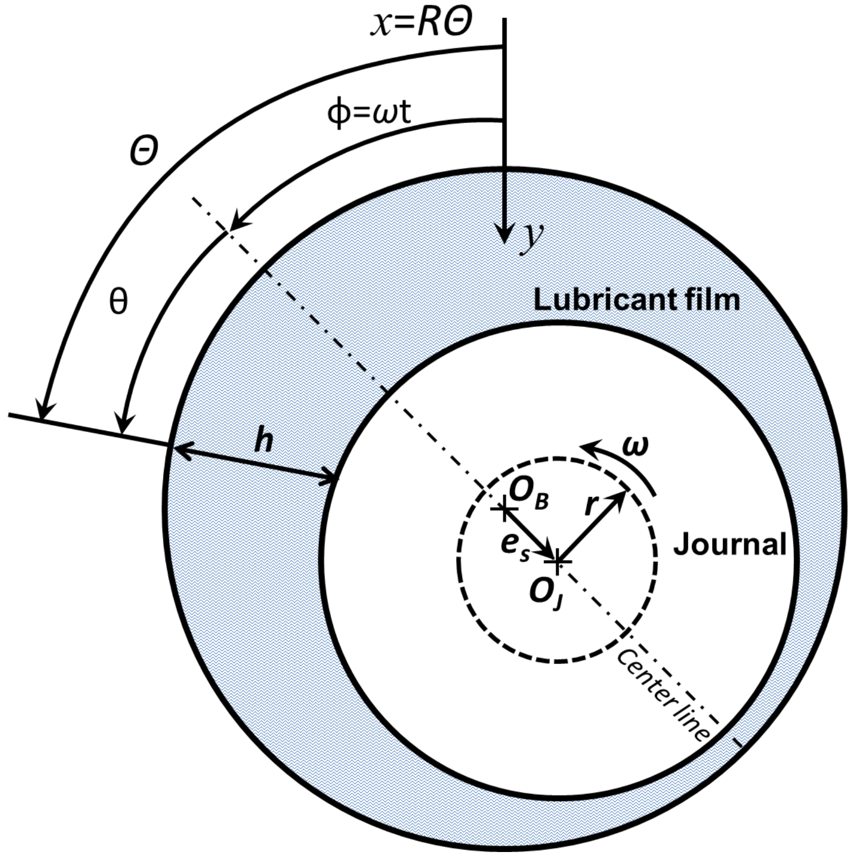

Fig. 28 Schematic view of a SFD with journal describing a circular orbit [1]

A FORTRAN® computational tool code [41], solves the modified Reynolds equation using the Finite Element method. The modified Reynolds equation includes temporal fluid inertia effects and governs the generation of lubricant pressure in both the film lands and in the groove,

$$\frac{\partial}{R\partial\Theta}\left(h^3\frac{\partial P}{R\partial\Theta}\right)+\frac{\partial}{\partial z}\left(h^3\frac{\partial P}{\partial z}\right)=12\mu\frac{\partial h}{\partial t}+\rho h^2\ \frac{\partial^2 h}{\partial t^2} \tag{7}$$

The terms on the left hand side represent the flow induced by pressure gradients. The first and second terms on the right hand side denote the flow induced by the change in film thickness respect to time (squeeze motion) and the temporal fluid inertia acceleration, respectively. Note that Eq. (5) introduces fluid inertia as a first order effect, thus this equation will not accurately predict SFD force coefficients for large amplitude journal motions [1].

The film thickness (h) is

$$h_{(\Theta,z,t)} = c_{(z)} + e_{X_{(t)}} \cos\left(\Theta\right) + e_{Y_{(t)}} \sin\left(\Theta\right) \tag{8}$$

and

$$\begin{aligned} e_{X_{(t)}} &= r\cos\left(\omega t\right) + e_s \cos(45^\circ) \\ e_{Y_{(t)}} &= r\sin\left(\omega t\right) + e_s \sin(45^\circ) \end{aligned} \tag{9}$$

where $c_{(z)}$ denotes the clearance along the axial direction.

Table 5 lists the input parameters for predictions of the SFD dynamic force coefficients. The user exercised an option available in the computational program [41]. This is an *orbit analysis* [42] estimating SFD force coefficients by first delivering the instantaneous damper reaction forces for a specified journal amplitude motion and static eccentricity in a one cycle of single frequency whirl motion. Note that the *orbit analysis* replicates the actual test procedure to estimate the SFD force coefficients. This analysis able to model with accuracy the test SFD delivering reliable force coefficients which is valid for any motions over a certain frequency range.

Figure 29 shows the predicted SFD direct damping and inertia force coefficients versus the effective groove clearance (d_η+c). The predictions refer to a circular orbit amplitude of r/c=0.08 at a centered journal position (e_s=0), where cross-coupled force coefficients are nil. The SFD direct damping and inertia force coefficients estimated from a CCOs test (r/c=0.08, e_s=0) are overlaid with the predictions. To match the predictions to test data, an effective groove depth d_η ~1.5c and 2.0c is used. Thus, d_η = 1.75c (439μm) is chosen to predict the SFD dynamic force coefficients for all condition where the actual groove depth is d_G=38c.

Prior research [4] with the same damper configuration, but with a smaller film clearance c_s=141μm, delivers an effective groove depth $d_{\eta s}$=1.6c_s (226μm). Different radial clearances, c and c_s, cause a difference on the estimated effective groove depths (d_η and $d_{\eta s}$).

Table 5. List of inputs for prediction of open ends SFD dynamic force coefficients.

SFD Geometry - three feed holes 120° apart	
Journal Diameter, D	12.7 cm (5.0 in)
Land Length, L_F	2.54 cm (1.0 in)
Radial Land Clearance, c	251.5 μm (9.9 mil)
Damper Axial Length (two lands + groove), L	6.35 cm (2.5 in)
Feed orifice Diameter, ϕ	2.54 mm (0.1 inch)
Groove Axial length, L_G	1.27 cm (0.5 inch)
Groove Depth, d_G	0.96 cm (0.38 inch)
Effective groove Depth, d_η	1.75 c
Operating conditions	
Ambient pressure, P_a	0 bar(g) (0 psig)
Groove pressure, P_G	0.12 bar(g) (1.6 psig)
Static eccentricity, e_S	0.0 - 0.76 c
Lubricant properties	
Supply temperature, T_{in}	25 °C (77 °F)
Lubrincant viscosity @ T_{in} , μ	2.96 cP (4.29 Reyns)
Lubricant density, ρ	785 kg/m^3 (49 lb/ft^3)
Lubricant cavitation pressure, P_c	-1.01 bar(g) (-14.65 psig)

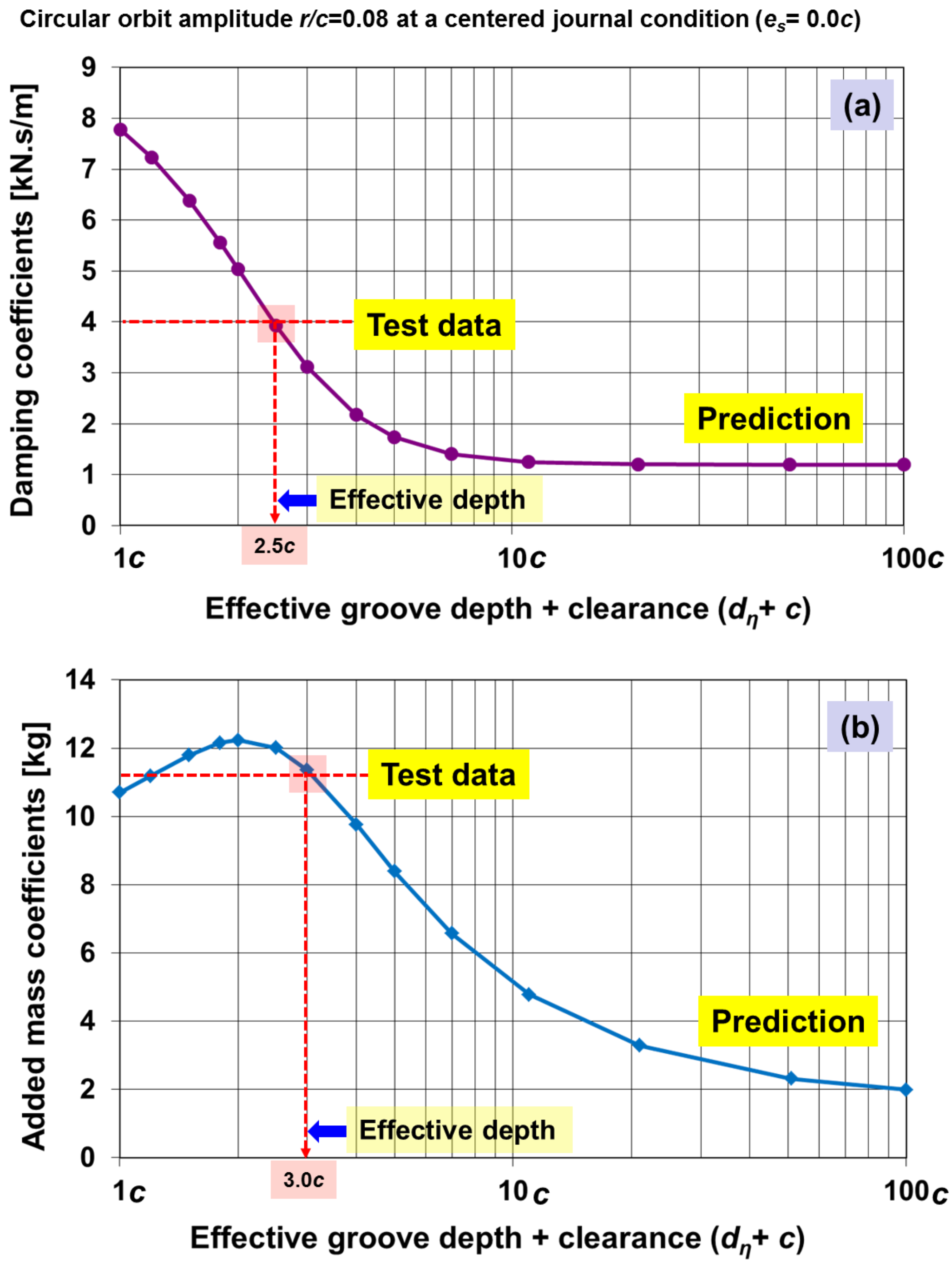

Fig. 29 Predicted SFD dynamic force coefficients versus effective groove depth + clearance: (a) SFD direct damping coefficients $(C_{XX}=C_{YY})_{SFD}$ and (b) SFD added mass coefficients $(M_{XX}=M_{YY})_{SFD}$. Test data compared with predictions.

1. Predictions and experimental results

Figures 30 and 31 depict the experimentally identified SFD damping and inertia coefficients and predictions versus static eccentricity for circular orbit amplitudes from r=0.08c to r=0.51c. The predictions and the experimental data show the SFD damping coefficients increase with static eccentricity. The predicted direct damping coefficients for orbit amplitudes r/c=0.08 and 0.15 display excellent agreement with the test derived coefficients with varying static eccentricities (e_s), up to ~51% of radial eccentricity. However, the SFD damping coefficients are over predicted more than ~28% at static eccentricity e_s/c=0.76. Also, predictions of theses coefficients at centered condition (e_s=0.0) tend to deviate from the experimental results with increasing orbit amplitudes. In addition, the experimentally driven SFD dynamic force coefficients (C_{XX}, C_{YY}) tend to diverge with each other as eccentricities increase indicating that the magnitude of damping generated from SFD depends on its direction.

Overall, the predictions of SFD added mass (M_{XX}, M_{YY}) agree well with the experimental results. However, the experimentally estimated SFD added mass increase more than the predictions with increasing static eccentricities. This discrepancy may be due to not accounting the convective inertia effect in the physical model and also neglecting the effect of the feeding orifices. Also, the predictions show M_{XX} is higher than M_{YY}, however, the test derived added masses show vice versa. In general, the predictions of SFD force coefficients, damping and added mass, agree well with the test results.

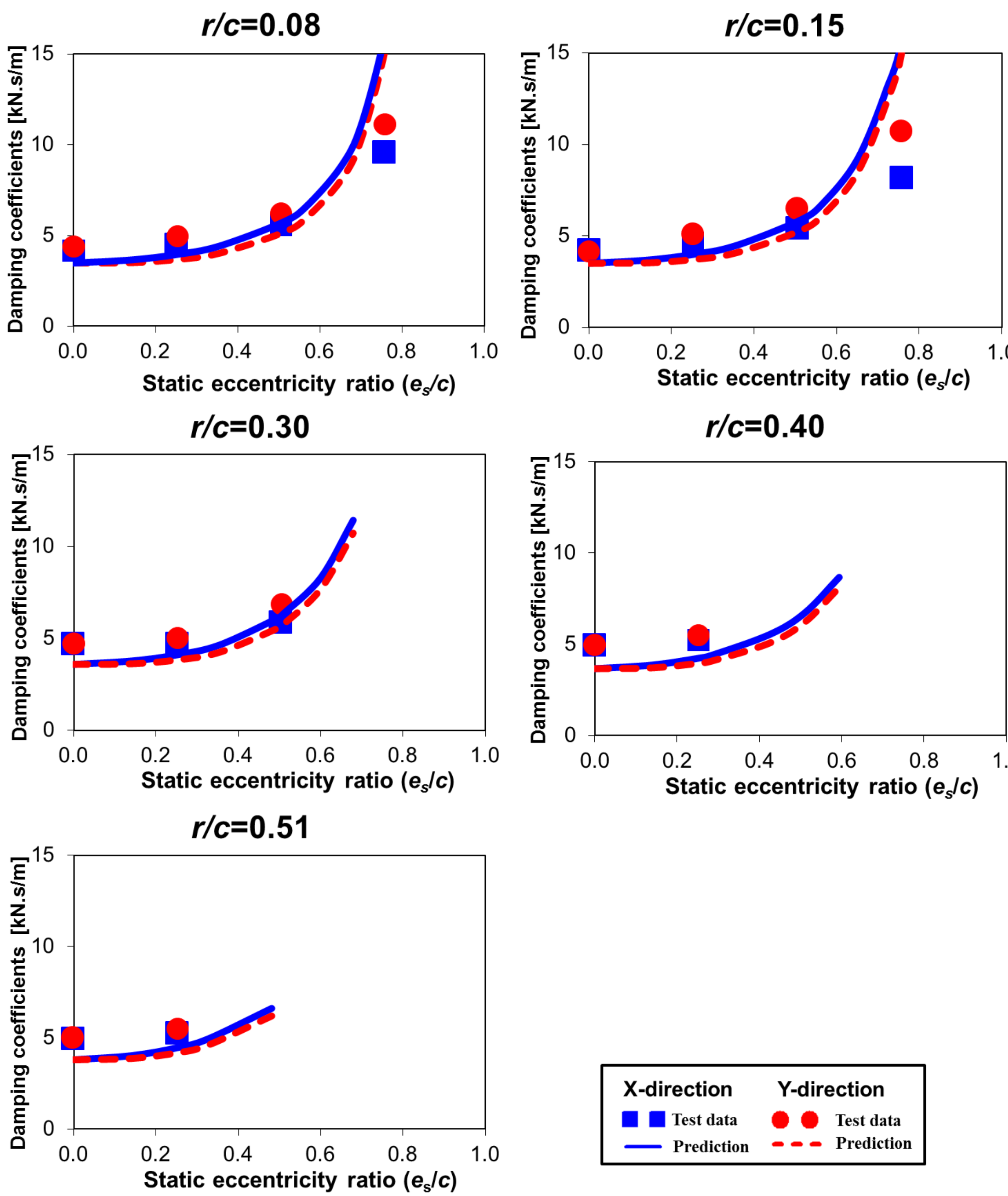

Fig. 30 Open ends SFDs: Direct damping $(C_{XX}, C_{YY})_{SFD}$ coefficients versus static eccentricity (e_s). Circular orbit amplitudes from r=0.08c to 0.51c. One inch film lands length with 0.251 *mm* film radial clearance and effective groove depth $d\eta$=1.75c.

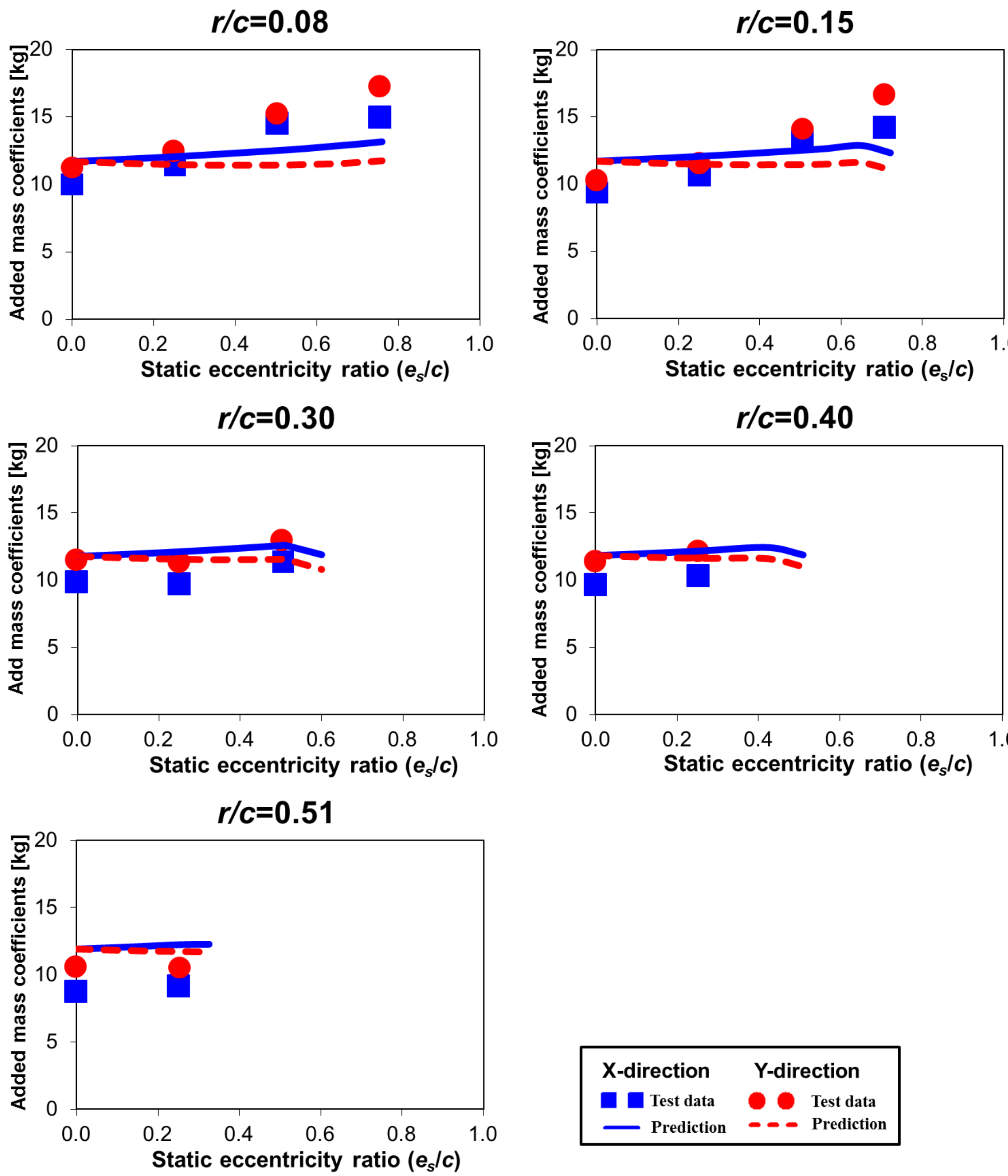

Fig. 31 Open ends SFDs: Direct added mass $(M_{XX}, M_{YY})_{SFD}$ coefficients versus static eccentricity (e_s). Circular orbit amplitudes from r=0.08c to 0.51c. One inch film lands length with 0.251 *mm* film radial clearance and effective groove depth $d\eta$=1.75c.

CHAPTER IX

EVALUATION OF THE LINEARIZED REPRESENTATION FOR SFD FORCES

In the experiments, the SFD (actual) reaction force ($\mathbf{F_{SFD}}$) from the squeeze film alone is determined from

$$-\mathbf{F_{SFD}} = \mathbf{F} - (\mathbf{M_s}\ddot{\mathbf{z}} - \mathbf{C_s}\dot{\mathbf{z}} - \mathbf{K_s}\mathbf{z}) - M_{BC}\mathbf{a} \tag{10}$$

where $\mathbf{F}=(F_X, F_Y)^T$ is the shakers external load vector, and $\mathbf{z}=(z_X, z_Y)^T$ is the vector of BC displacements relative to the journal motion. ($\mathbf{K_s}$, $\mathbf{C_s}$, $\mathbf{M_s}$) are matrices of structural stiffness, damping and residual mass coefficients.

An approximate (linearized) SFD reaction force $\mathbf{F_{SFD_L}}$ is built by using the identified SFD force coefficients ($\mathbf{K_{SFD}}$, $\mathbf{C_{SFD}}$, $\mathbf{M_{SFD}}$), i.e.,

$$-\mathbf{F_{SFD_L}} \cong \mathbf{M_{SFD}}\ddot{\mathbf{z}} + \mathbf{C_{SFD}}\,\dot{\mathbf{z}} + \mathbf{K_{SFD}}\mathbf{z} \tag{11}$$

Figure 32 depicts the comparison between the experimental $\mathbf{F_{SFD}}$ and the *linearized* $\mathbf{F_{SFD_L}}$ for operation at a whirl frequency of 100 Hz. For small orbit amplitude motions at r/c=0.08 and at a centered condition, e_s/c=0.0, see Figure 32 (a), the actual and *linearized* SFD reaction forces are similar in terms of their magnitude and phase.

As the static eccentricity increases to e_s/c=0.75 with a fixed orbit amplitude r/c=0.08, both SFD reaction forces increase, see Figure 32 (b). There are no significant magnitude differences between $\left|\mathbf{F_{SFD}}\right|$ and $\left|\mathbf{F_{SFD_L}}\right|$.

Figure 32 (c) shows the forces for an orbit amplitude r/c=0.71 at a centered condition (e_s/c=0.0). The SFD force magnitude at r/c=0.71 is at least six times the force magnitude for the small orbit r/c=0.08 at a centered condition. The differences between $\left|\mathbf{F_{SFD}}\right|$ and $\left|\mathbf{F_{SFD_L}}\right|$ are significant at the largest orbit radii.

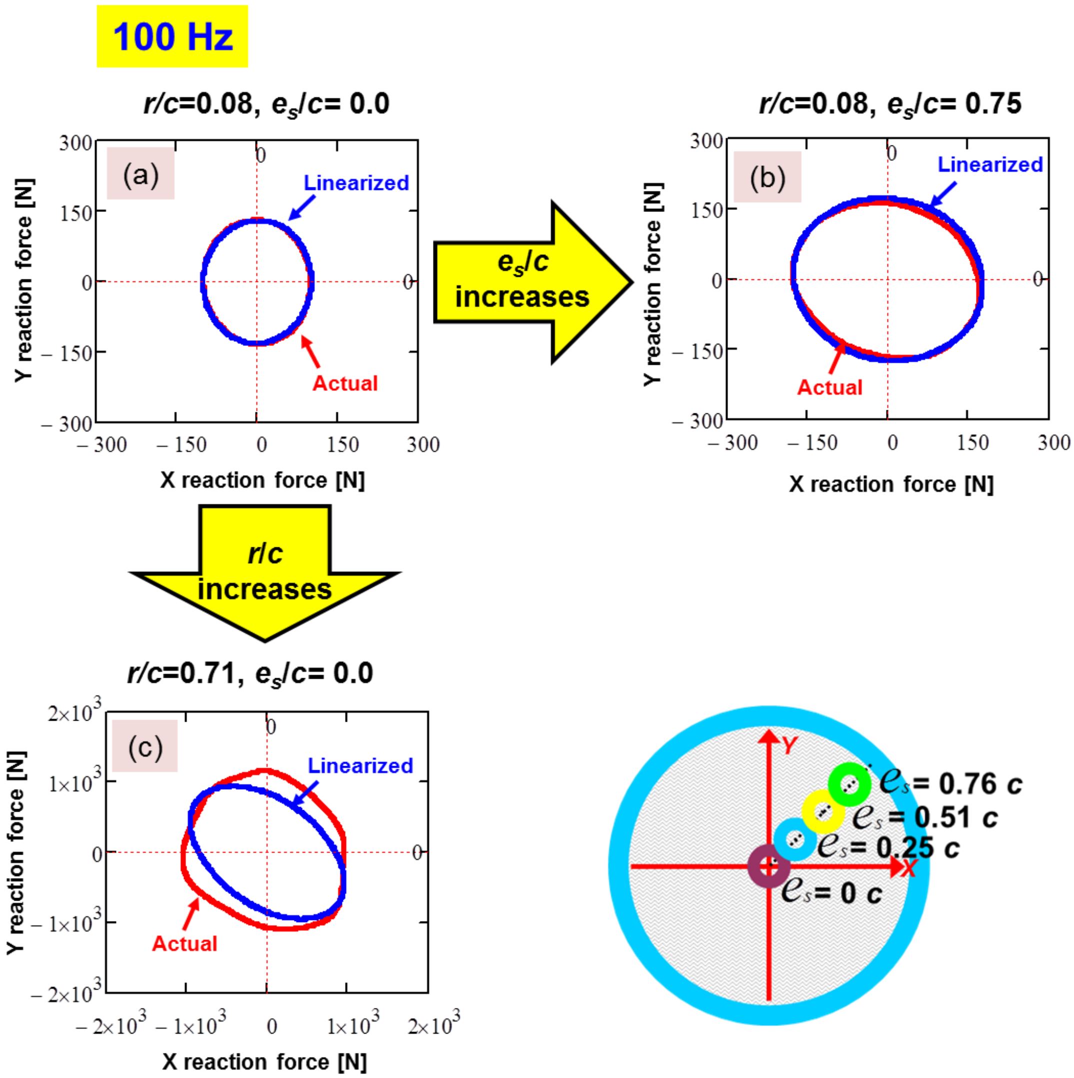

Fig. 32 Open ends SFDs: Actual (test) and linearized SFD reaction forces for operation at (a) r=0.08c and e_s/c=0.00, (b) r=0.08c and e_s/c=0.75, (c) r=0.71c and e_s/c=0.00. A whirl frequency of 100 Hz. One inch film lands length with 0.251 *mm* film radial clearance. Note different scales for the force magnitudes.

The goodness of the identified SFD force coefficients is quantified by comparing the work performed by $\mathbf{F_{SFD}}$ and $\mathbf{F_{SFD_L}}$ over one period of whirl motion. The mechanical work (or energy dissipated) over a full period of whirl motion equals

$$E_{DIS} = \oint_0^{T=2\pi/\omega} (F_{SFD_X}\dot{x} + F_{SFD_Y}\dot{y})dt \tag{12}$$

where (F_{SFD_X}, F_{SFD_Y}) are the components of $\mathbf{F_{SFD}}$, and ($\dot{x}$, $\dot{y}$) denote the velocity components of journal along the *X* and *Y* directions. Note that a negative work indicates the SFD dissipates energy.

Figure 33 shows the mechanical energy dissipation of the SFD as determined from the actual and linearized forces $(-E_{DIS}, -E_{DIS_L})$ at a whirl frequency of 100 Hz. The test SFD mechanical energy dissipation increases with increasing orbit amplitude (*r/c*). However, the SFD energy dissipation from the actual forces shows a higher energy dissipation than the estimated energy based on the linearized force at the moderately large orbit amplitudes *r/c*>0.6.

Figure 34 depicts the difference between linear-nonlinear energy dissipations. The dissipated energy difference ratio is

$$E_{diff} = 1 - \frac{E_{DIS_L}}{E_{DIS}} \tag{13}$$

E_{diff} increases with increasing static eccentricity (e_s) and orbit amplitude (r); albeit the difference is more prominent for moderately to large orbit amplitudes; at *r/c*>0.6, E_{diff} ~23%. These differences indicate that experimentally identified SFD forced coefficients (K_{SFD}, C_{SFD}, M_{SFD}) obtained from large orbit amplitudes *r/c*>0.6 do not accurately represent the actual SFD system. However, for most test conditions, *r/c*≤0.4 and e_s/c≤0.25, E_{diff} is less than ~5%, thus showing the SFD force coefficients represent well the actual forced response of the test system.

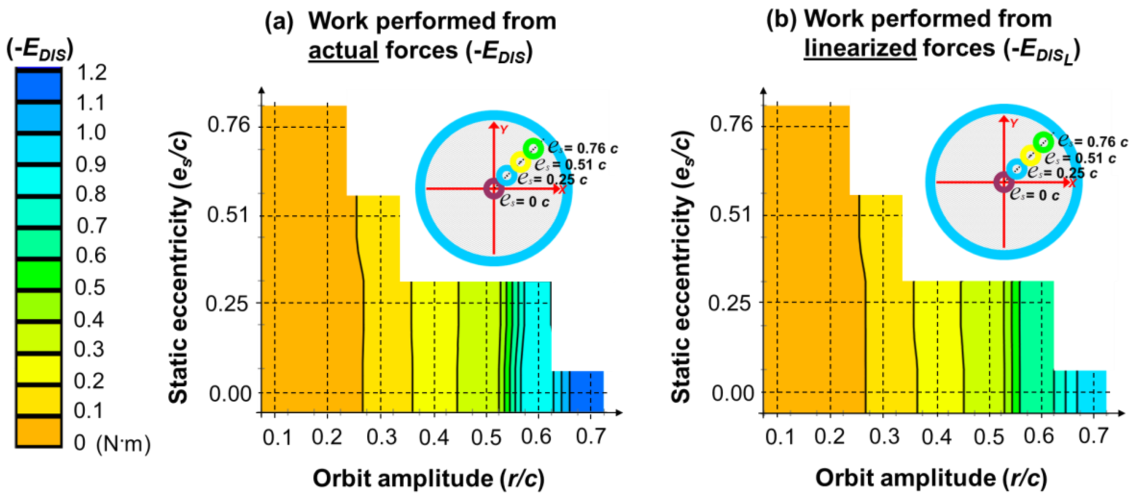

Fig. 33 Open ends SFDs: SFD mechanical work performed from the (a) actual forces (F_{SFD}) and (b) linearized forces (F_{SFD_L}). Circular orbit amplitudes from r=0.08c to 0.71c and static eccentricities from e_s/c=0.00 to 0.76. A whirl frequency of 100 Hz. One inch film lands length with 0.251 *mm* film radial clearance.

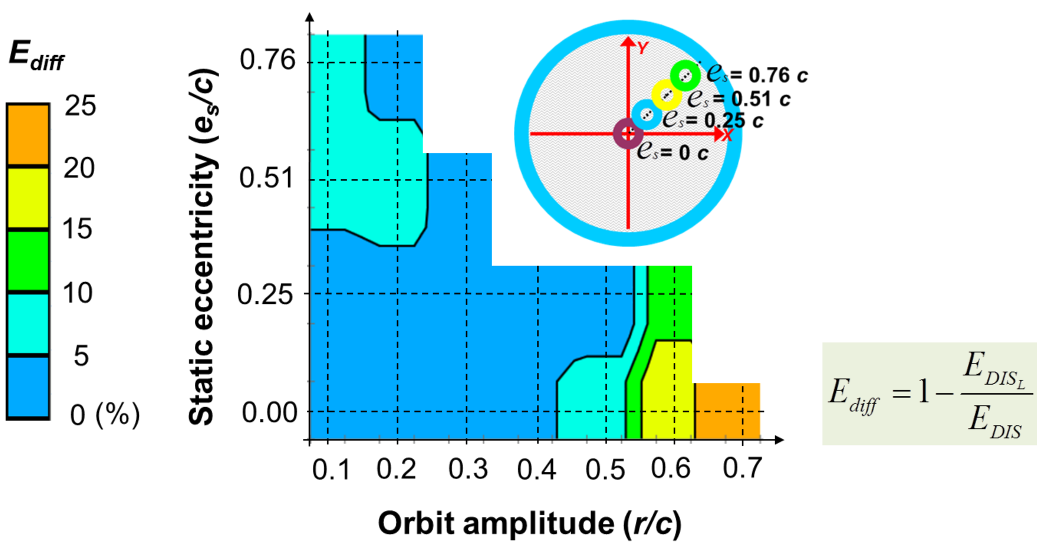

Fig. 34 Open ends SFDs: difference ratios between the actual SFD energy dissipation (E_{DIS}) and linearized SFD energy dissipation (E_{DIS_L}). Circular orbit amplitudes from r=0.08c to 0.71c and static eccentricities from e_s=0.00c to 0.76c. A whirl frequency of 100 Hz. One inch film lands length with 0.251 *mm* film radial clearance.

CHAPTER X

CONCLUSIONS AND RECOMMENDATION

The research describes tests on a SFD for eight increasing orbit amplitudes (r=0.08c to ~0.71c) with whirl frequency ranging from 10 – 100 Hz and with four static eccentricities (e_s/c=0, 0.25, 0.51, 0.76) and a parameter identification of the SFD dynamic force coefficients.

The estimated SFD force coefficients and measured dynamic pressures, as well as the predictions based on a computational analysis, extend the knowledge of SFD dynamic forced performance. The following conclusions are drawn from the experiments.

(a) The direct damping coefficients (C_{XX}, C_{YY}) increase with both the orbit amplitude (r) and the static eccentricity (e_s); albeit C_{XX} and C_{YY} show a large increase for orbit radii r/c>0.51.

(b) Cross-coupled damping coefficients (C_{XY}, C_{YX}) are at least one order of magnitude lower than the C_{XX} or C_{YY} for circular centered orbit tests with e_s/c<0.51. However, the cross-coupled damping coefficients increase to become as large as 40% of the direct damping coefficient for operating at a static eccentricity e_s/c=0.76.

(c) The direct added mass coefficients (M_{XX}, M_{YY}) increase with increasing journal eccentricity (e_s) and decrease slightly with orbit amplitudes to r/c~0.51. However, M_{XX} and M_{YY} show a notable drop when the orbit amplitude exceeds r/c~0.61. At e_s/c=0.76 and r/c≤0.15, the SFD added mass is as large as the BC ~17 kg. Cross-coupled added masses (M_{XY}, M_{YX}) are small though increasing with the static eccentricity. These coefficients are insensitive to the amplitude of circular orbit.

(d) For small to moderate orbit radii r/c<0.61, the effective dynamic stiffness coefficient ($K_{X-eff} \cong -M_{XX}\omega^2$) decreases with an increase in excitation frequency.

For large orbit $r/c \geq 0.61$, K_{X-eff} shows invariant values throughout the excitation frequencies. Note that an inertial effect is assumed to be negligible ($M_{SFD} \approx 0$) for circular orbit amplitudes $r/c \geq 0.6$. The $K_{X\text{-}eff}$ remains relatively constant for increasing amplitudes of journal circular motion.

(e) Comparison between the SFD direct damping and added mass estimated from both SFDs differing in clearance (c=251 μm, c_s=141 μm) but with identical film land lengths and groove show modest agreement with the theoretical ratios due to the strong interaction between the film lands and the central groove.

(f) The effective damping coefficient ($C_{X-eff} = -\dfrac{K_{XY}}{\omega} + C_{XX} + M_{XY}\omega$) increases with both increasing orbit amplitudes (r) and/or static eccentricity (e_s) whereas shows little dependency with excitation frequency. $C_{X\text{-}eff}$ increases with e_s due to the increase of the cross-coupled added mass term ($M_{XY}\omega$).

(g) Measured dynamic pressures in the central groove are not nil and are of the same order of magnitude as the dynamic pressures in the film lands. This indicates that the damper film lands are not effectively separated by the central groove.

(h) Peak-to-peak dynamic pressures in the film lands and the groove increase with both increasing orbit amplitude (r/c) and whirl frequency (ω). Furthermore, the dynamic pressures in the groove with groove depth (d_G = 38c) are mainly affected by fluid inertia rather than viscous effects. On the other hand, the dynamic pressures in both the film lands show that the contribution of fluid viscous ($\overline{P}_{viscous}$) on pressures increases with increasing orbit amplitudes.

(i) Comparison between test derived SFD damping coefficients with predictions based on effective groove depth shows excellent agreement with static eccentricities to e_s/c~0.51, but tends to deviate above e_s >0.51c.

(j) The predictions of SFD added masses agree well with the experimental results; albeit the predictions of SFD added masses tend to underpredict the test data at e_s/c>0.51.

(k) Mechanical energy dissipation estimated from both the actual and *linearized* SFD forces increases with increasing orbit amplitude (r/c). At moderately large orbit amplitudes r/c>0.6, the SFD energy dissipation from the actual forces (E_{DIS}) shows a higher energy dissipation than E_{DIS_L}.

(l) Comparison between the mechanical work of SFD estimated from both the actual and *linearized* SFD forces show that identified SFD forced coefficients (K_{SFD}, C_{SFD}, M_{SFD}) represent well the actual SFD system with the operating condition of $e_s/c \leq 0.25$ and $r/c \leq 0.40$.

The present work provides benchmark test data and advances knowledge of SFDs operating with moderately large journal whirl motions (r/c) and large static eccentricities (e_s/c).

A comprehensive study of a wide range of SFD configurations is underway. In particular, future work aims to include circular orbit tests with sealed ends SFDs with large journal whirl motions (r/c) and large static eccentricities (e_s/c).

REFERENCES

[1] San Andrés, L., 2012, "Squeeze Film Damper: Operation, Models and Technical Issues," Modern Lubrication Theory, Notes 13, Texas A&M University Digital Libraries, http://repository.tamu.edu/handle/1969.1/93197 [02/05/2013].

[2] Vance, J., Zeidan, F., and Murphy, B., 2010, *Machinery Vibration and Rotordynamics*, John Wiley & Sons, Inc., New York.

[3] San Andrés, L., 2012, "Damping and Inertia Coefficients for Two Open Ends Squeeze Film Dampers with A Central Groove: Measurements and Predictions," ASME J. Tribol., **134**(10), 102506.

[4] Seshagiri, S., 2011, "Identification of Force Coefficients in Two Squeeze Film Dampers with a Central Groove," M.S. Thesis, Texas A&M Univ., College Station, TX., USA.

[5] Mahecha, P., 2011, "Experimental Dynamic Forced Performance of a Centrally Grooved, End Sealed Squeeze Film Damper," M.S. Thesis, Texas A&M Univ., College Station, TX., USA.

[6] Diaz, S., and San Andrés, L., 2001, "Air Entrainment versus Lubricant Vaporization in Squeeze Film Dampers: an Experimental Assessment of their Fundamental Differences" ASME J. Eng. Gas Turbines Power, **123**, pp. 1-7.

[7] Zeidan, F. Y., and Vance, J. M, 1989, "Cavitation Leading to a Two Phase Fluid in a Squeeze Film Damper," STLE Tribol. Trans., **32,** pp. 100-104.

[8] Zeidan, F. Y., and Vance, J. M, 1990, "A Density Correlation for a Two Phase Lubricant and Its Effect on the Pressure Distribution," STLE Tribol. Trans., **33,** pp. 641-647.

[9] Della Pietra, L., Adiletta, G., 2002, "The Squeeze Film Damper over Four Decades of Investigations. Part I: Characteristics and Operating Features," Shock Vib. Dig., **34**(1), pp. 3-26.

[10] Adiletta, G., Della Pietra, L., 2002, "The Squeeze Film Damper over Four Decades of Investigations. Part II: Rotordynamics Analysis with Rigid and Flexible Rotors," Shock Vib. Dig, **34**(2), pp. 97-126.

[11] San Andrés, L., 1985, "Effects of Fluid Inertia Effect on Squeeze Film Damper Force Response," Ph.D. Dissertation, Texas A&M University, College Station, TX

[12] San Andrés, L., and Vance, J., 1987. "Experimental Measurement of The Dynamic Pressure Distribution in a Squeeze Film Bearing Damper Executing Circular Centered Orbits," ASLE Trans., **30**(3), pp. 373-383

[13] Tichy, J.A., 1987, "A Study of the Effect of Fluid Inertia and End Leakage in the Finite Squeeze Film Damper," ASME J. Tribol., **109**(1), pp. 54-59.

[14] San Andrés, L., 1992, "Analysis of Short squeeze Film Dampers with a Central Groove," ASME, J. Tribol., **114**(4), pp. 659-664

[15] Ramli, M. D., Roberts, J.B., and Ellis, J., 1987, "The Determination of Squeeze Film Dynamic Coefficients from Experimental Transient Data," ASME J. Tribol., **109**(1), pp.153-163.

[16] Arauz, G. L., San Andrés, L., 1994, "Effect of a Circumferential Feeding Groove on the Dynamic Force Response of a Short Squeeze Film Damper", ASME J. Tribol., **116**(2), pp. 369-376

[17] Qingchang, T., Ying, C., and Lyjiang, W., 1997, "Effect of a Circumferential Feeding Groove on Fluid Force in Short Squeeze Film Dampers," Tribol. Int., **30**(6), pp. 409-416

[18] Tiwari, R., Lees, A.W., Friswell, M.I., 2004, "Identification of Dynamic Bearing Parameters: A Review," Shock Vib. Dig., **36**(2), pp. 99-124.

[19] Fritzen, C. P., 1985, "Identification of Mass, Damping, and stiffness Matrices of Mechanical System," ASME J. Vib., Acoust., **108**, pp. 9-16

[20] San Andrés, L., and Delgado, A., 2007, "Identification of Force Coefficients in a Squeeze Film Damper With a Mechanical Seal – Part I: Unidirectional Load Tests," ASME, J. Eng. Gas Turbines Power, **129**(3), pp. 858-864.

[21] San Andrés, L., and Delgado, A., 2007, "Identification of Force Coefficients in a Squeeze Film Damper with a Mechanical Seal – Centered Circular Orbit Tests," ASME, J. Tribology, **129**(3), pp. 660-668.

[22] San Andrés, L., and Delgado, A., 2012, "A Novel Bulk-Flow Model for Improved Predictions of Force Coefficients in Grooved Oil Seals Operating Eccentrically," ASME J. Eng. Gas Turbines Power, **134**(5), 052509

[23] Gehannin, J., Arghir, M., and Bonneau, O., 2010, "Complete Squeeze-Film Damper Analysis Based on the "Bulk Flow" Equations," STLE Tribol. Trans., **53**(1), pp. 84-96.

[24] Defaye, C., Arghir, M., and Bonneau, O., 2006, "Experimental Study of the Radial and Tangential Forces in a Whirling Squeeze Film Damper," STLE Tribol. Trans., **49**(2) pp. 271-278.

[25] Zeidan, F. Y, and Vance, J. M, 1989, "Cavitation Leading to a Two Phase Fluid in a Squeeze Film Damper," STLE Tribol. Trans., **32**, pp. 100-104.

[26] Zeidan, F. Y, and Vance, J. M, 1990, "A Density Correlation for a Two Phase Lubricant and Its Effect on the Pressure Distribution," STLE Tribol. Trans., **33**, pp. 641-647

[27] San Andrés and Diaz, S., L., 2003, "Flow Visualization and Forces from a Squeeze Film Damper Operating with Natural Air Entrainment," ASME J. Tribol., **125**, pp. 325-333

[28] Diaz, S., and San Andrés, L., 1999, "Reduction of the Dynamic Load Capacity in a Squeeze Film Damper Operating with a Bubbly Lubricant," ASME J. Eng. Gas Turbines Power, **121**, pp. 703-709.

[29] Diaz, S., and San Andrés, L., 2001, "A Model for Squeeze Film Dampers Operating with Air Entrainment and Validation with Experiments," ASME J. Tribol., **123**(1), pp. 125-133.

[30] Brennen, C., 1995, *Cavitation and Bubble Dynamics*, Oxford Engineering Series 44, Oxford University Press, New York.

[31] Diaz, S., and San Andrés, L., 1998, "Effect of Bubbly Flow on the Dynamic Pressure Fields of a Test Squeeze Film Damper," ASEM Fluids Engineering Division Summer Meeting, Washington, DC, June, Paper FEDSM98-5070

[32] Tao, L., Diaz, S., San Andrés, and Rajagopal, K., 2000, "Analysis of Squeeze Film Dampers Operating With Bubbly Lubricants," ASME J. Tribol., **122**, pp. 205-210.

[33] Mendez, T. H., Ciaccia, M. A., Torres, J. E. and Diaz, S. E., 2009, "On the Numerical Prediction of Finite Length Squeeze Film Dampers Performance with Free Air Entrainment," ASME J. Eng. Gas Turbines Power, **132**(1), 012501

[34] Torres, J. E., and Diaz, S. E., 2010, "Finite Length Squeeze Film Dampers with Air Entrainment: Non-Dimensional Maps and Their Applicability," ASME paper GT2010-22561

[35] Zhang, J., Roberts, J.B., and Ellis, J., 1994, "Experimental Behavior of a Short Cylindrical Squeeze Film Damper Executing Circular Centered Orbits," ASME J. Tribol., **116**(3), pp. 528-534.

[36] San Andrés, L., and De Santiago, O., 2004, "Forced Response of a Squeeze Film Damper and Identification of Force Coefficients from Large Orbital Motions," ASME J. Tribol., **126**(2), pp. 292-300.

[37] San Andrés, L., 2011, "Experimental and Predicted Force Coefficients for Long and Short SFDs: Open and Sealed ends," Annual Report (Y III) to Pratt & Whitney UTC, January.

[38] San Andrés, L., 2012, "Experimental Identification of Bearing Force Coefficients," Modern Lubrication Theory, Notes 14, Texas A&M University Digital Libraries, http://repository.tamu.edu/handle/1969.1/93197 [02/05/2013].

[39] San Andrés, L., 2009, Monthly Progress Report #12 to Pratt & Whitney UTC, Technical Report No. 12, November 2009.

[40] San Andrés, L., 2013, "Simple Analysis on Dynamic Pressure," Personal Communication.

[41] San Andrés, L., 2010, "PW_SFD_2010," SFD Predictive Code developed for Pratt & Whitney Engines, MEEN Dept., Texas A&M University (Proprietary).

[42] San Andrés, L., 2012, "Estimation of Bearing Force Coefficients from Orbit Analysis," Personal Communication.

APPENDIX A

IDENTIFICATION OF SFD DYNAMIC FORCED COEFFICIENTS[5]

This appendix presents the procedure to identify the SFD dynamic force coefficients. Figure A.1 represents a physical model of the BC and static rod supports as a two degree of freedom mechanical system. The system comprising the four main support rods and the bearing cartridge (BC) has structural (dry) stiffness, damping and residual mass **(K,C,M)$_S$** without any lubrication in the film lands. Since the BC effective mass (M_{BC}) represents the system mass, these (**M**)$_S$ denotes a small amount of residual mass.

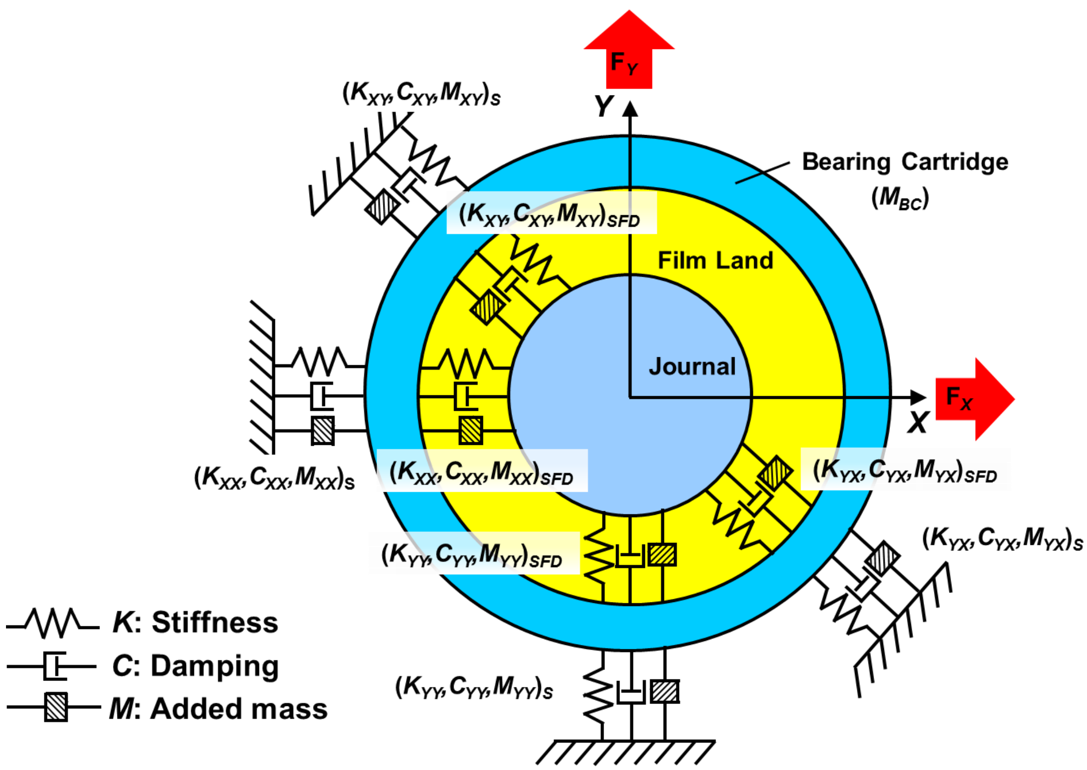

Fig. A.1 Schematic illustration of SFD physical model [2]

[5] Portions of this appendix reproduce ad-verbatim information presented in Ref. [38]

The BC effective (M_{BC}) mass, including the instrumentations and mass contribution of four main rods, is estimated before any static tests. Ensuing static load tests under dry condition serves to estimate the structure stiffness K_S.

Since the testing physical model is represented as a two degree of freedom mechanical system, two linearly independent displacement vectors (X,Y) resulting from two linearly independent excitation load vectors (F_X,F_Y) are sufficient to identify the system structural parameters. Thus, by performing unidirectional dynamic load tests, the structural parameters under dry condition are estimated $(\mathbf{K},\mathbf{C},\mathbf{M})_\mathbf{S}$.

Before conducting a dynamic load test with lubricant supplied through the damper lands, the oil flow rates at top and bottom film lands are measured to ensure equal lubricant supply through the two film lands.

Later, circular orbit tests, of increasing orbit amplitudes and for static eccentricities under a lubricated condition, serve to estimate the lubricated system coefficients $(\mathbf{K},\mathbf{C},\mathbf{M})_\mathbf{L}$. Lastly, the SFD force coefficients are determined by deducting the structural coefficients from the lubricated system coefficients,

$$(\mathbf{K},\ \mathbf{C},\ \mathbf{M})_{\mathbf{SFD}} = (\mathbf{K},\ \mathbf{C},\ \mathbf{M})_\mathbf{L} - (\mathbf{K},\ \mathbf{C},\ \mathbf{M})_\mathbf{S} \tag{A.1}$$

The shakers excite the BC with single frequency (ω) loads ($F_{X(t)}$,$F_{Y(t)}$) along the X and Y axes to induce unidirectional, circular, or elliptical BC motions. For a unidirectional dynamic load test in the X direction, excitation loads are applied at the X axis whereas no load is imposed on the Y axis. In the same fashion, excitation loads are imposed only at Y axis during the Y direction dynamic load test. Thus, the two load vectors are linearly independent

$$\mathbf{F}_1 = \begin{bmatrix} F_{X_{(t)}} \\ 0 \end{bmatrix};\ \ \mathbf{F}_2 = \begin{bmatrix} 0 \\ F_{Y_{(t)}} \end{bmatrix} \tag{A.2}$$

Performing multiple sets of circular orbit tests, centered and off centered, the single frequency loads are imposed on the BC to produce clockwise and anti-clockwise orbits. The single frequency load vectors are

$$\mathbf{F}_1 = \mathrm{Re}\left(\begin{bmatrix} F_{X_1} \\ iF_{Y_1} \end{bmatrix} e^{i\omega t}\right) = \begin{bmatrix} F_{X_1}\cos(\omega t) \\ -F_{Y_1}\sin(\omega t) \end{bmatrix}$$
$$\mathbf{F}_2 = \mathrm{Re}\left(\begin{bmatrix} F_{X_2} \\ -iF_{Y_2} \end{bmatrix} e^{i\omega t}\right) = \begin{bmatrix} F_{X_2}\cos(\omega t) \\ F_{Y_2}\sin(\omega t) \end{bmatrix} \quad \text{(A.3)}$$

The equation of motion for the dry (unlubricated) condition is

$$\begin{bmatrix} F_X \\ F_Y \end{bmatrix}_{SFD} = \begin{bmatrix} M_{BC} & 0 \\ 0 & M_{BC} \end{bmatrix}\begin{bmatrix} a_X \\ a_Y \end{bmatrix} + \begin{bmatrix} M_{XX} & M_{XY} \\ M_{YX} & M_{YY} \end{bmatrix}_S \begin{bmatrix} \ddot{Z}_X \\ \ddot{Z}_Y \end{bmatrix} + \begin{bmatrix} C_{XX} & C_{XY} \\ C_{YX} & C_{YY} \end{bmatrix}_S \begin{bmatrix} \dot{Z}_X \\ \dot{Z}_Y \end{bmatrix} + \begin{bmatrix} K_{XX} & K_{XY} \\ K_{YX} & K_{YY} \end{bmatrix}_S \begin{bmatrix} Z_X \\ Z_Y \end{bmatrix} \quad \text{(A.4)}$$

in matrix form,

$$\mathbf{F_s} - M_{BC}\,\mathbf{a} = \mathbf{M_s}\,\ddot{\mathbf{z}} + \mathbf{C_s}\,\dot{\mathbf{z}} + \mathbf{K_s}\,\mathbf{z} \quad \text{(A.5)}$$

where $\mathbf{F_s}=(F_X, F_Y)^T$ is the load vector of the forces imposed on the BC, and M_{BC} is effective mass of the BC. The $\mathbf{a}=(a_X, a_Y)^T$ is the vector of the BC acceleration measured from the accelerometers, installed in the BC along the X and Y directions, and $\mathbf{z}=(Z_X, Z_Y)^T$ is the vector of relative displacements between the BC and the journal motion.

The SFD reaction force vector is defined in a linear form as

$$-\begin{bmatrix} F_X \\ F_Y \end{bmatrix}_{SFD} = \begin{bmatrix} M_{XX} & M_{XY} \\ M_{YX} & M_{YY} \end{bmatrix}_{SFD} \begin{bmatrix} \ddot{Z}_X \\ \ddot{Z}_Y \end{bmatrix} + \begin{bmatrix} C_{XX} & C_{XY} \\ C_{YX} & C_{YY} \end{bmatrix}_{SFD} \begin{bmatrix} \dot{Z}_X \\ \dot{Z}_Y \end{bmatrix} + \begin{bmatrix} K_{XX} & K_{XY} \\ K_{YX} & K_{YY} \end{bmatrix}_{SFD} \begin{bmatrix} Z_X \\ Z_Y \end{bmatrix} \quad \text{(A.6)}$$

in other words,

$$-\mathbf{F_{SFD}} = \mathbf{M_{SFD}}\ddot{\mathbf{z}} + \mathbf{C_{SFD}}\,\dot{\mathbf{z}} + \mathbf{K_{SFD}}\mathbf{z} \quad \text{(A.7)}$$

where, $\mathbf{F_{SFD}}$, $\mathbf{M_{SFD}}$, $\mathbf{C_{SFD}}$, and $\mathbf{K_{SFD}}$ denote the SFD reaction force, and the SFD mass, damping, and stiffness matrices, respectively.

The equation of motion for the circular orbit tests with the lubricated system including the structure and SFD is

$$\mathbf{F} - M_{BC}\,\mathbf{a} = (\mathbf{M_s} + \mathbf{M_{SFD}})\ddot{\mathbf{z}} + (\mathbf{C_s} + \mathbf{C_{SFD}})\dot{\mathbf{z}} + (\mathbf{K_s} + \mathbf{K_{SFD}})\mathbf{z} \quad \text{(A.8)}$$

Transforming the equation of motions (time domain) into a frequency domain renders

$$\left[-\omega^2\,\mathbf{M_s} + \mathbf{K_s} + i\,\omega\mathbf{C_s}\right]\overline{\mathbf{Z}}_{\mathbf{s}(\omega)} = \overline{\mathbf{F}}_{\mathbf{s}(\omega)} - M_{BC}\,\overline{\mathbf{a}}_{\mathbf{s}(\omega)} \quad \text{(A.9)}$$

$$\left[-\omega^2\,\mathbf{M_{SFD}}+\mathbf{K_{SFD}}+i\,\omega\,\mathbf{C_{SFD}}\right]\overline{\mathbf{Z}}_{\mathbf{SFD}(\omega)}=\overline{\mathbf{F}}_{\mathbf{SFD}(\omega)} \tag{A.10}$$

$$\left[-\omega^2\,(\mathbf{M_{SFD}}+\mathbf{M_s})+(\mathbf{K_{SFD}}+\mathbf{K_s})+i\,\omega(\mathbf{C_{SFD}}+\mathbf{C_s})\right]\overline{\mathbf{Z}}_{(\omega)}=\overline{\mathbf{F}}_{(\omega)} \tag{A.11}$$

where $\mathbf{Z}_{(\omega)}$, $\mathbf{F}_{(\omega)}$, and $\mathbf{a}_{(\omega)}$ denote the Discrete Fourier Transformation (DFT) of the displacements, forces and accelerations with respect to time

$$\begin{aligned}\overline{\mathbf{Z}}_{(\omega)}&=DFT(\mathbf{z}_{(t)}), \quad i\omega\overline{\mathbf{Z}}_{(\omega)}=DFT(\dot{\mathbf{z}}_{(t)})\\ \overline{\mathbf{F}}_{(\omega)}&=DFT(\mathbf{F}_{(t)}), \quad \overline{\mathbf{a}}_{(\omega)}=DFT(\mathbf{a}_{(t)})\end{aligned} \tag{A.12}$$

The impedance matrix of the dry test system is defines as

$$\left[-\omega^2\,\mathbf{M_s}+\mathbf{K_s}+i\,\omega\mathbf{C_s}\right]=\mathbf{H_s} \tag{A.13}$$

and the flexibility matrix of dry condition is

$$\mathbf{G_s}=\mathbf{H_s}^{-1} \tag{A.14}$$

Then, the Instrument Variable Filter Method (IVFM) curve fits the system flexibility functions $(\mathbf{G})_{i,j=X,Y}$ within the designated frequency range to estimate the structural parameters **(K, C, M)**$_{\mathbf{S}}$. The impedance matrix of the lubricated test system is

$$\left[-\omega^2\,(\underbrace{\mathbf{M_{SFD}}+\mathbf{M_s}}_{\mathbf{M_L}})+(\underbrace{\mathbf{K_{SFD}}+\mathbf{K_s}}_{\mathbf{K_L}})+i\,\omega(\underbrace{\mathbf{C_{SFD}}+\mathbf{C_s}}_{\mathbf{C_L}})\right]=\mathbf{H} \tag{A.15}$$

By substituting the impedance matrix into Eq. (A.12) becomes

$$\mathbf{H}\overline{\mathbf{Z}}_{(\omega)}=\overline{\mathbf{F}}_{(\omega)} \tag{A.16}$$

when two linearly independent displacement vectors are ensued by two linearly independent excitation load vectors. Thus, Eq. (A.16) can be rewritten as

$$\mathbf{H}\left[\overline{\mathbf{Z}}_1 \quad \overline{\mathbf{Z}}_2\right]=\left[\overline{\mathbf{F}}_1 \quad \overline{\mathbf{F}}_2\right] \tag{A.17}$$

and reorganizing Eq. (A.17)

$$\begin{bmatrix} H_{XX} & H_{XY}\\ H_{YX} & H_{YY}\end{bmatrix}=\left[\overline{\mathbf{F}}_1 \quad \overline{\mathbf{F}}_2\right]\left[\overline{\mathbf{Z}}_1 \quad \overline{\mathbf{Z}}_2\right]^{-1} \tag{A.18}$$

First, by curve fitting the individual set of real and imaginary part of mechanical impedance matrix $\mathbf{H}_{k=1,2,..Nfreq}$ at each frequency ω_k, over designated frequency range, lubricated system parameters $(\mathbf{K, C, M})_L$ are pre-estimated [38]. Then, the IVFM curve fits the four test system flexibility functions $(\mathbf{G})_{i,j=X,Y}$ over designated frequency range and lubricated system parameters $(\mathbf{K, C, M})_L$ are estimated with reduced measurement noises. Note that the flexibility matrix is an inverse function of impedance, i.e., $\mathbf{H}^{-1}=\mathbf{G}$. Also the correlation coefficients (r^2) between the test data and the curve fit are the yardstick for how well the physical model represents [equation (A.5), (A.7), and (A.8)] the actual test system.

See Ref [38] for a more detailed (and better written) description of the parameter identification procedure.

APPENDIX B

BEARING CARTRIDGE DISPLACEMENT AND LOAD ORBITS FROM CIRCULAR ORBIT TESTS

Figures B.1 through B.4 depict the recorded amplitudes of the journal motions during the circular orbit tests with four static eccentricity conditions (e_s/c=0.0, 0.25, 0.51, 0.76) for the excitation frequencies ranging from 10 to 100 Hz. The journal orbits are fairly circular for the tests with increasing orbit amplitudes.

Figures B.5 through B.8 show the Fourier coefficients of the displacement responses (*r/c*) versus the excitation frequency. The magnitudes of the Fourier coefficients stay constant throughout the test frequency range (10 – 100 Hz).

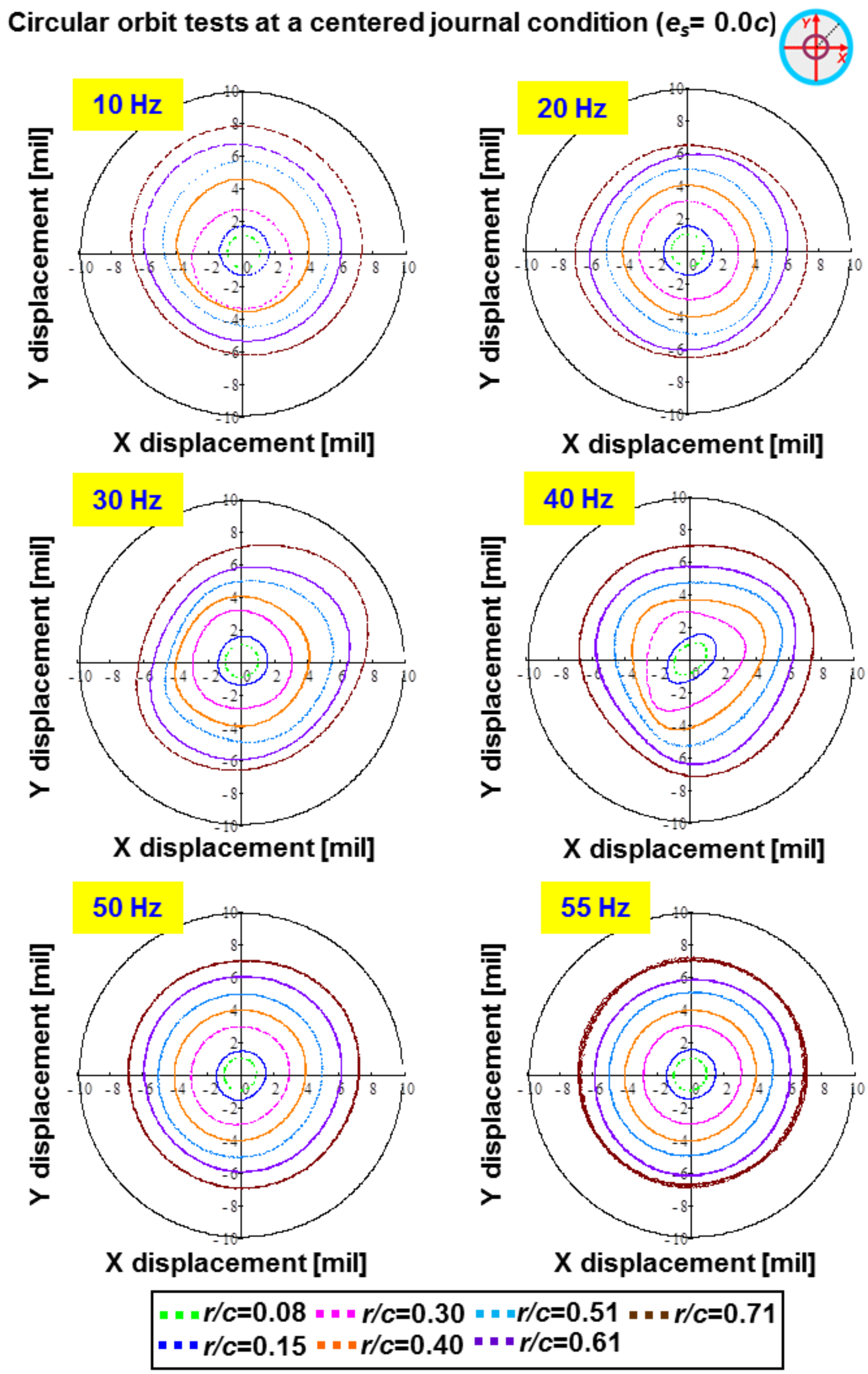

Fig. B.1 Recorded displacement orbits for tests with whirl frequencies ranging from 10 to 100 Hz. Circular centered (e_S=0.0*c*) orbits with amplitude *r*=0.08*c* to *r*=0.71*c.* Open-ends SFD with *c*=251.5 μm and two 25.4 mm length film lands.

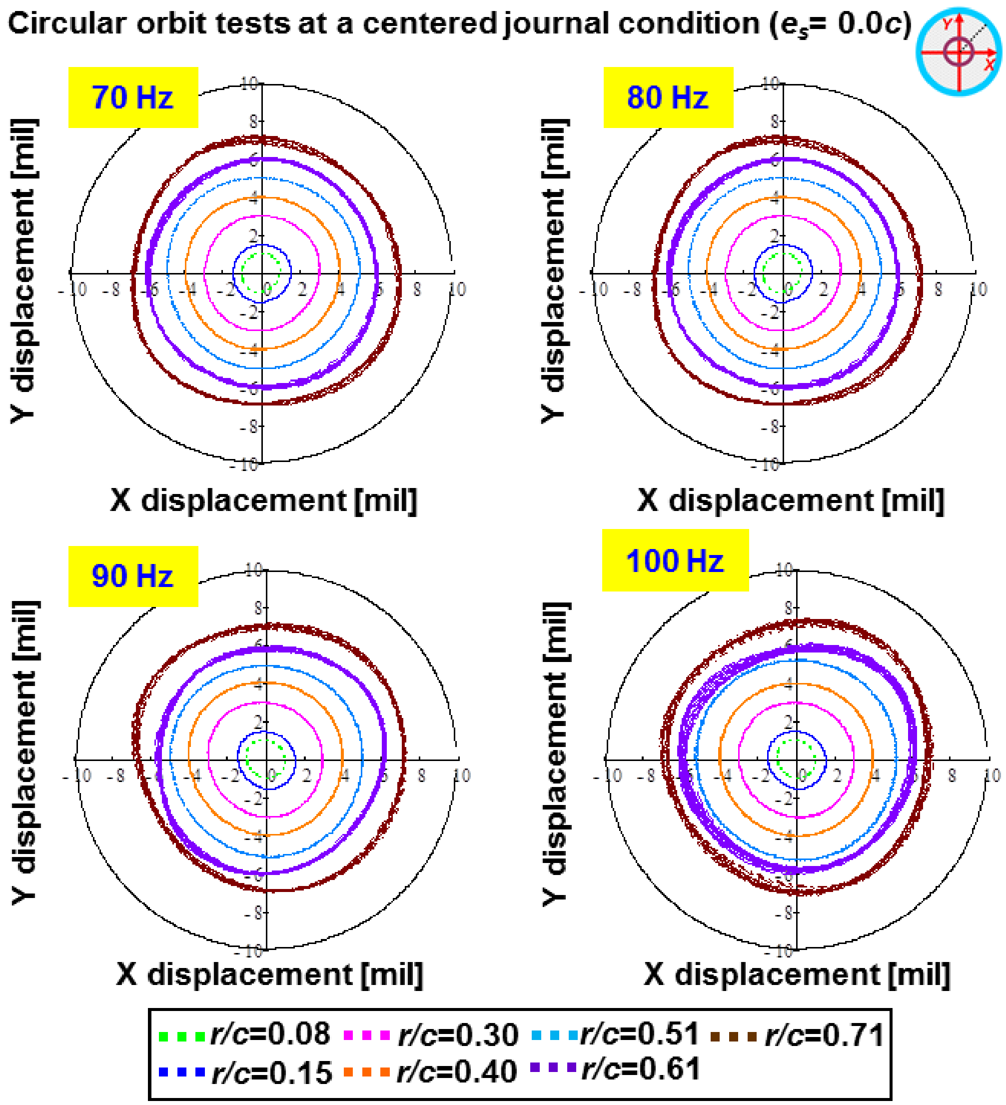

Fig. B.1 Continued.

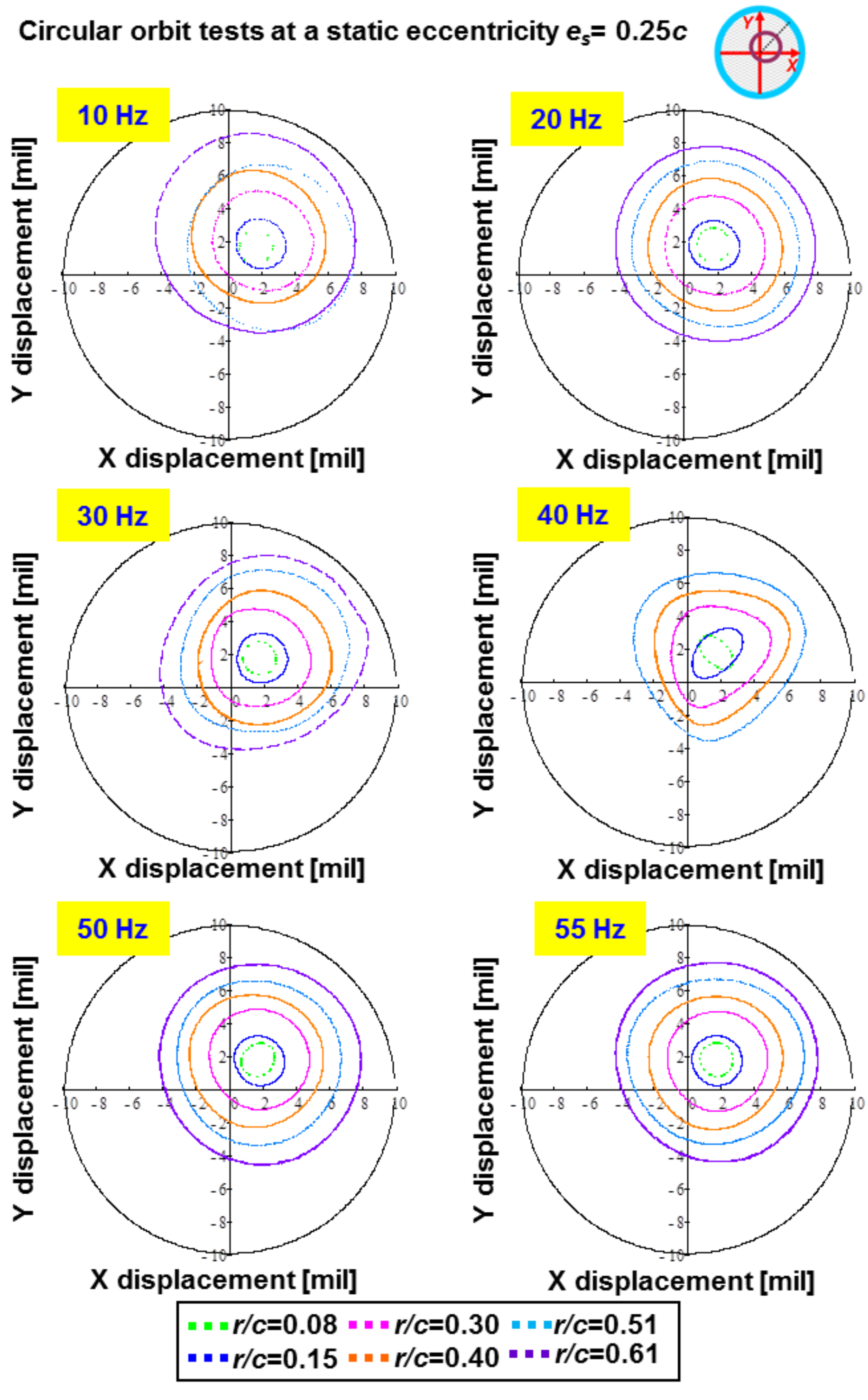

Fig. B.2 Recorded displacement orbits for tests with whirl frequencies ranging from 10 to 100 Hz. Circular orbits with amplitude r=0.08c to r=0.61c at static eccentricity (e_S=0.25c). Open-ends SFD with c=251.5 μm and two 25.4 mm length film lands.

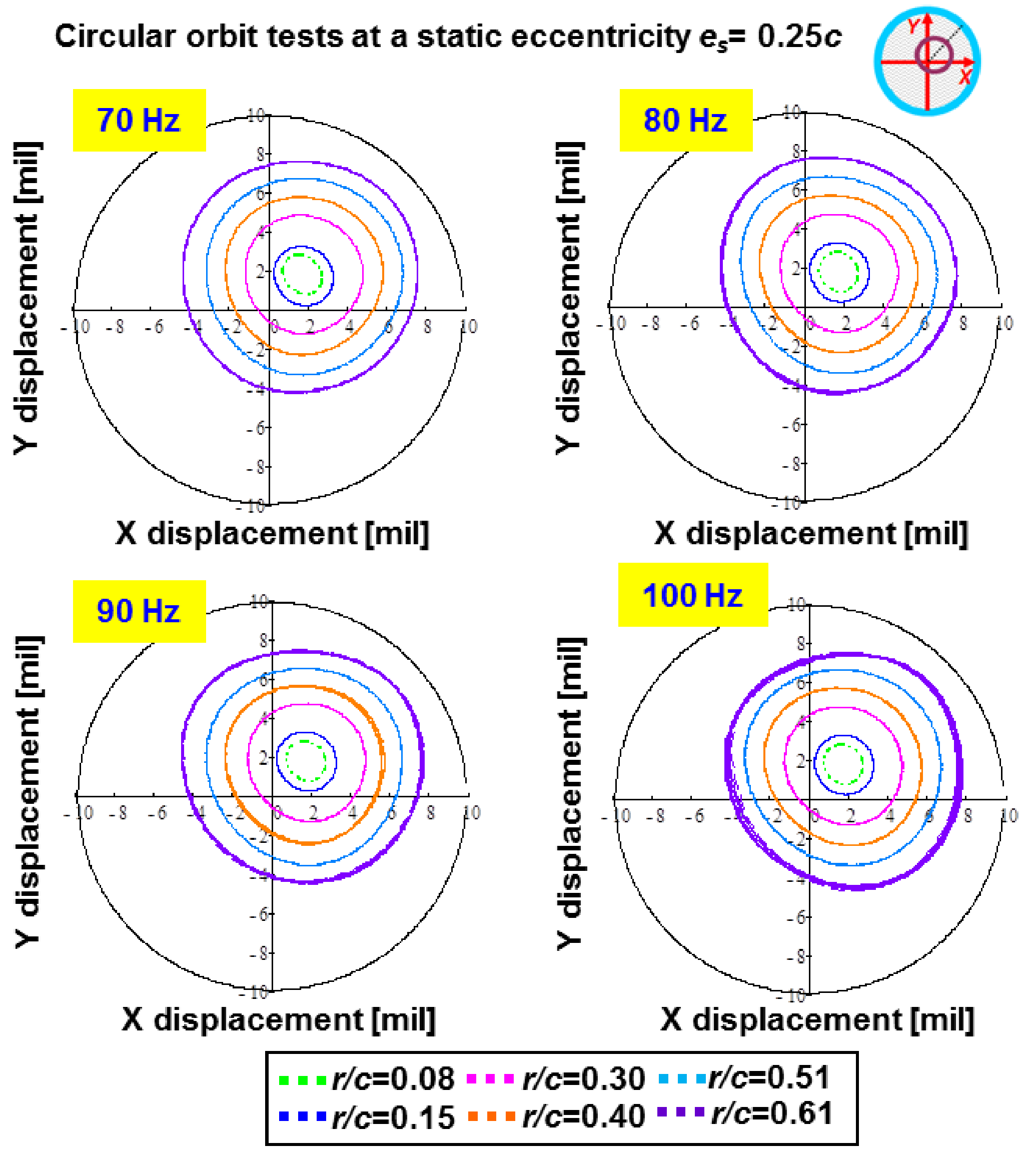

Fig. B.2 Continued.

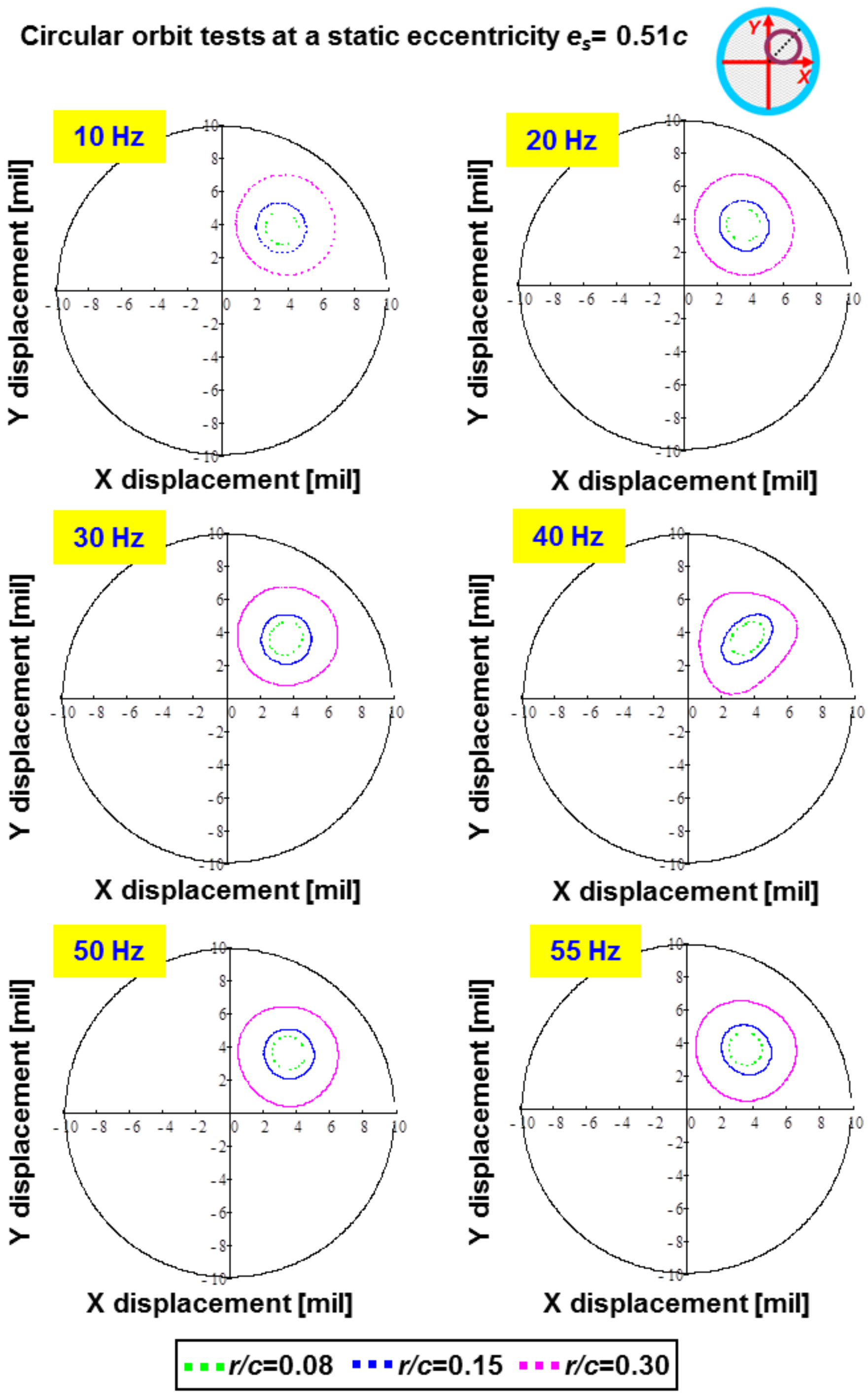

Fig. B.3 Recorded displacement orbits for tests with whirl frequencies ranging from 10 to 100 Hz. Circular orbits with amplitude r=0.08c to r=0.30c at static eccentricity (e_S=0.51c). Open-ends SFD with c=251.5 μm and two 25.4 mm length film lands.

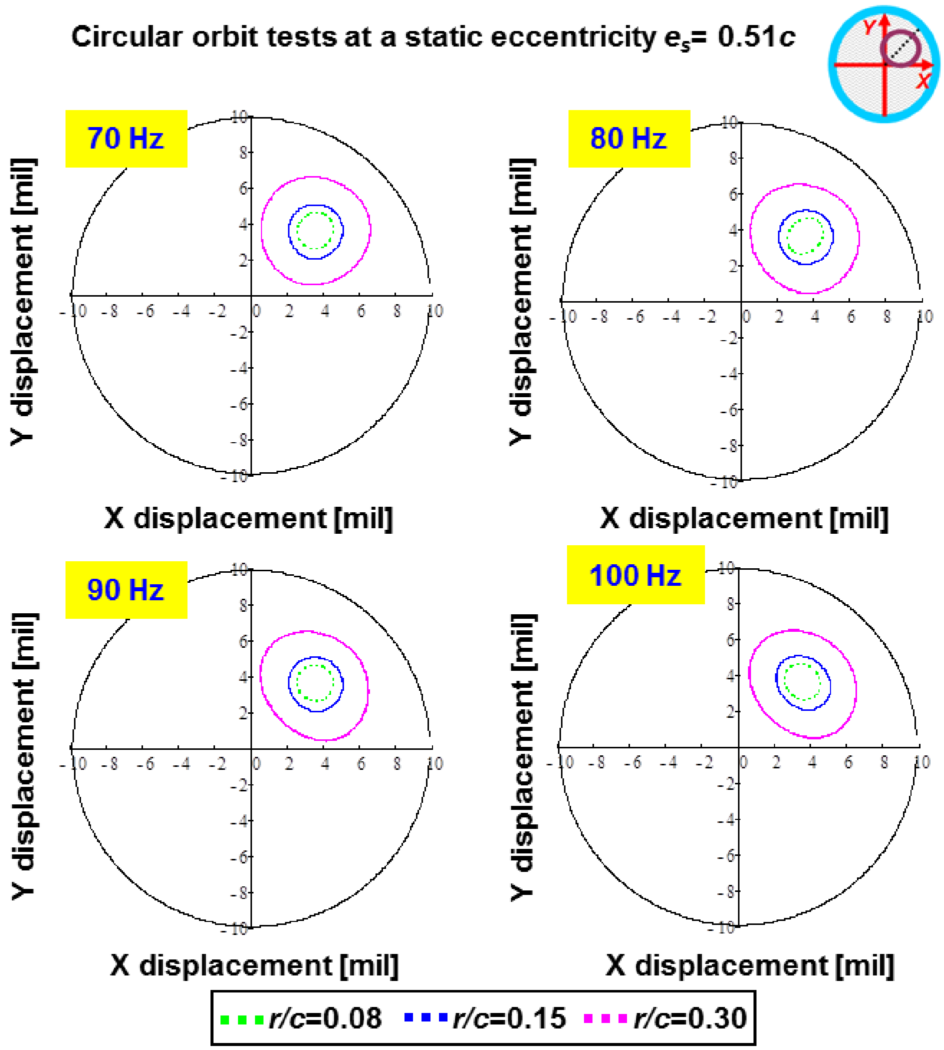

Fig. B.3 Continued.

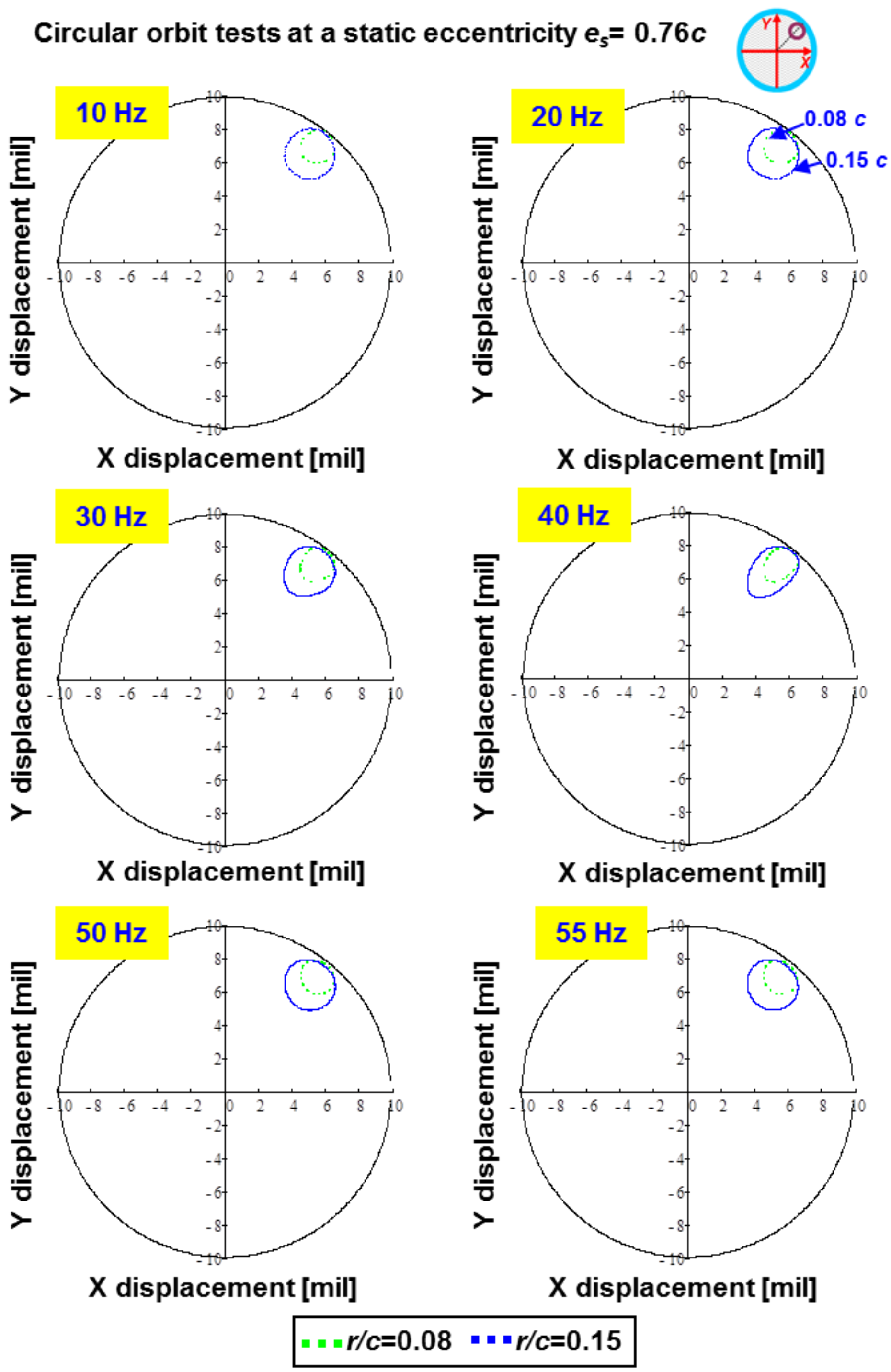

Fig. B.4 Recorded displacement orbits for tests with whirl frequencies ranging from 10 to 100 Hz. Circular orbits with amplitude *r*=0.08*c* to *r*=0.15*c* at static eccentricity (e_S=0.76*c*). Open-ends SFD with *c*=251.5 μm and two 25.4 mm length film lands.

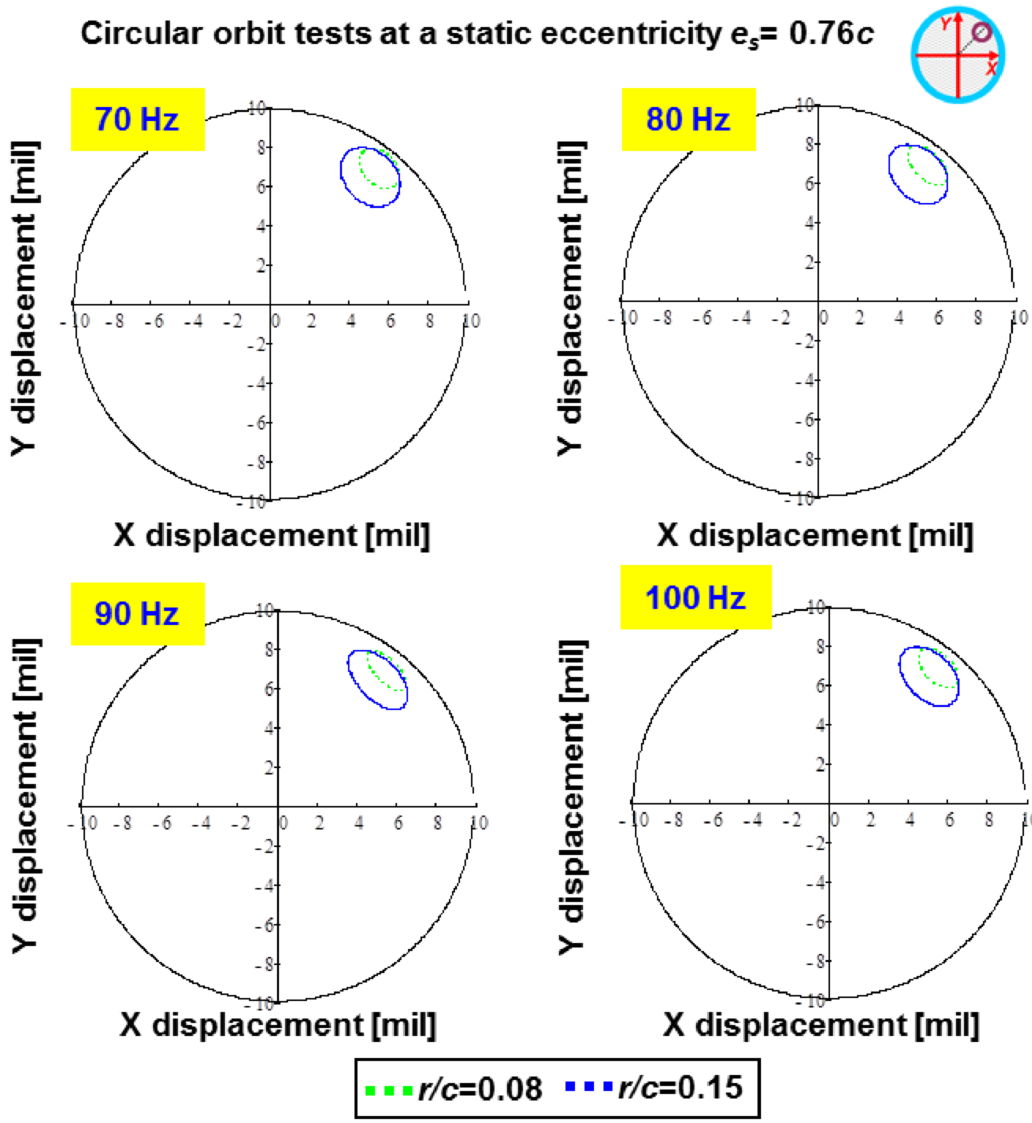

Fig. B.4 Continued.

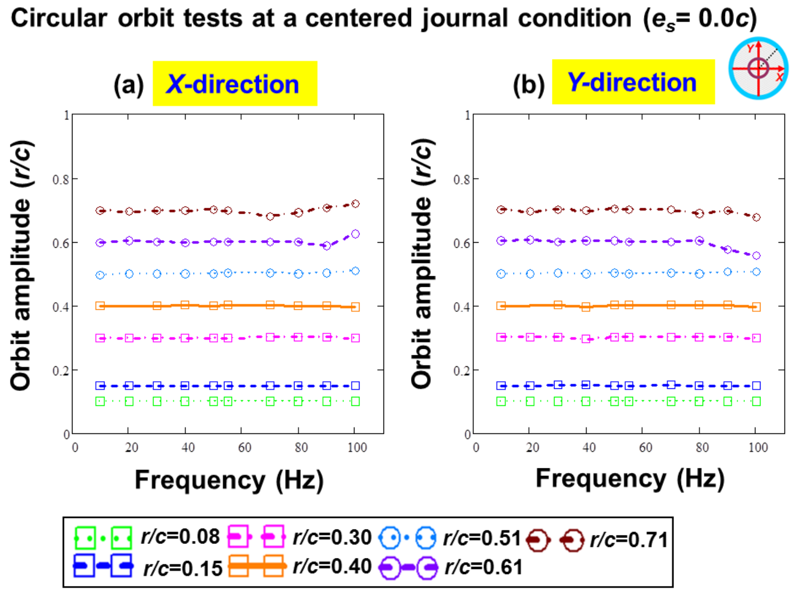

Fig. B.5 Fourier coefficients of the displacement responses versus excitation frequencies ranging from 10 to 100 Hz. Tests with the circular centered (e_s=0.0*c*) orbit amplitudes *r*=0.08*c* to *r*=0.71*c*. (a) *X*-direction, (b) *Y*-direction. Open-ends SFD with *c*=251.5 μm and two 25.4 mm length film lands.

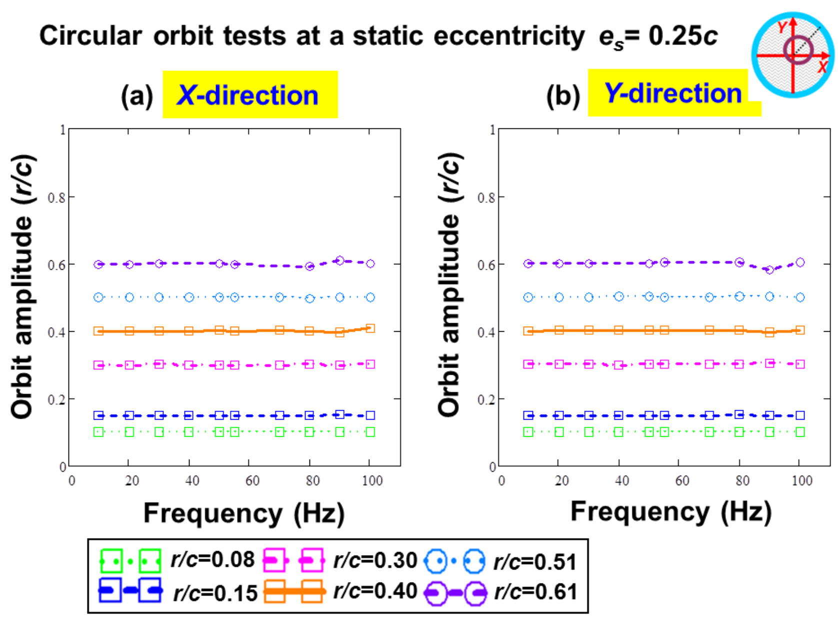

Fig. B.6 Fourier coefficients of the displacement responses versus excitation frequencies ranging from 10 to 100 Hz. Tests with the circular orbit amplitudes *r*=0.08*c* to *r*=0.61*c* at static eccentricity (e_s=0.25*c*). (a) *X*-direction, (b) *Y*-direction. Open-ends SFD with *c*=251.5 μm and two 25.4 mm length film lands.

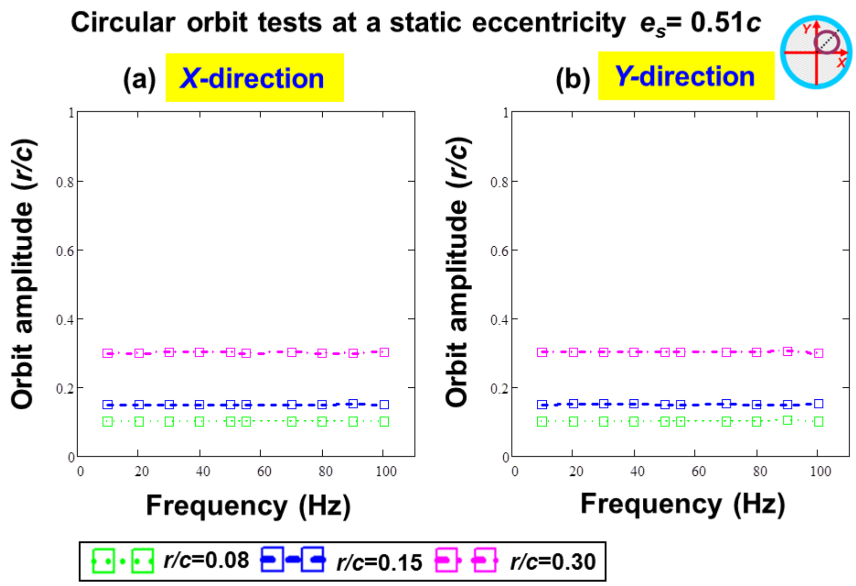

Fig. B.7 Fourier coefficients of the displacement responses versus excitation frequencies ranging from 10 to 100 Hz. Tests with the circular orbit amplitudes r=0.08c to r=0.30c at static eccentricity (e_s=0.51c). (a) *X*-direction, (b) *Y*-direction. Open-ends SFD with c=251.5 μm and two 25.4 mm length film lands.

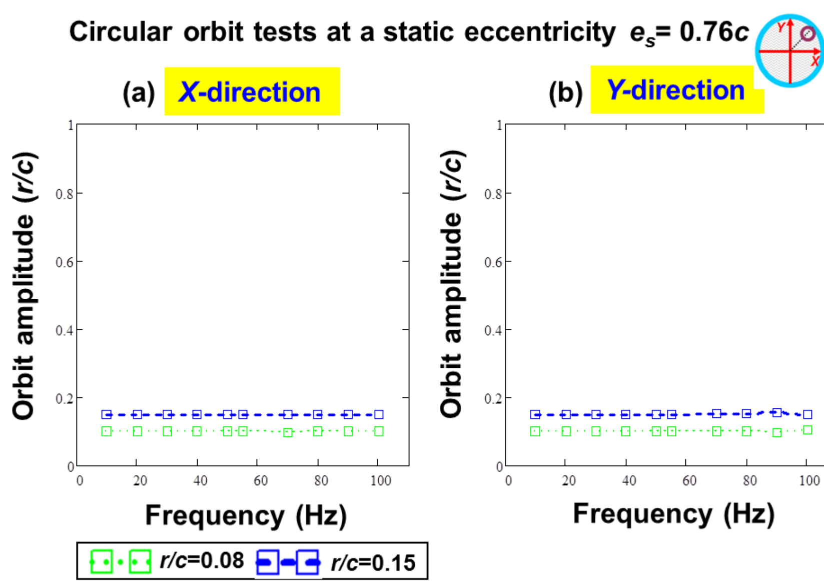

Fig. B.8 Fourier coefficients of the displacement responses versus excitation frequencies ranging from 10 to 100 Hz. Tests with the circular orbit amplitudes r=0.08c to r=0.15c at static eccentricity (e_s=0.76c). (a) *X*-direction, (b) *Y*-direction. Open-ends SFD with c=251.5 μm and two 25.4 mm length film lands.

Table B.1 presents the static load applied by the static loader, 45º away from the two shakers, to render the static eccentricity of the BC. Figures B.9 through B.12 depict the applied forces on the BC for frequencies ranging from 10 to 100 Hz during the circular orbit tests with a lubricated condition. To ensure constant orbit radii, the excitation force magnitudes are adjusted throughout the whirl frequency range (10 – 100 Hz). Unlike the circular journal orbits, the excitation forces show more elliptical orbits, which is probably due to characteristic of the test rig structural orthotropic, i.e. different stiffness along the *X* and *Y* directions of the system ($K_{S\text{-}XX}$=9.26 MN/m, $K_{S\text{-}YY}$=9.68 MN/m). Since $K_{S\text{-}YY} > K_{S\text{-}XX}$, the applied force magnitudes are higher along the *Y*-direction as shown in Figure B.9 to B.12.

Table B.1 Applied static load and ensuing static eccentricity of the BC

Static eccentricity (e_s/c)	Static Load (kN)
0.00	0.00
0.25	0.54
0.51	1.09
0.76	1.64

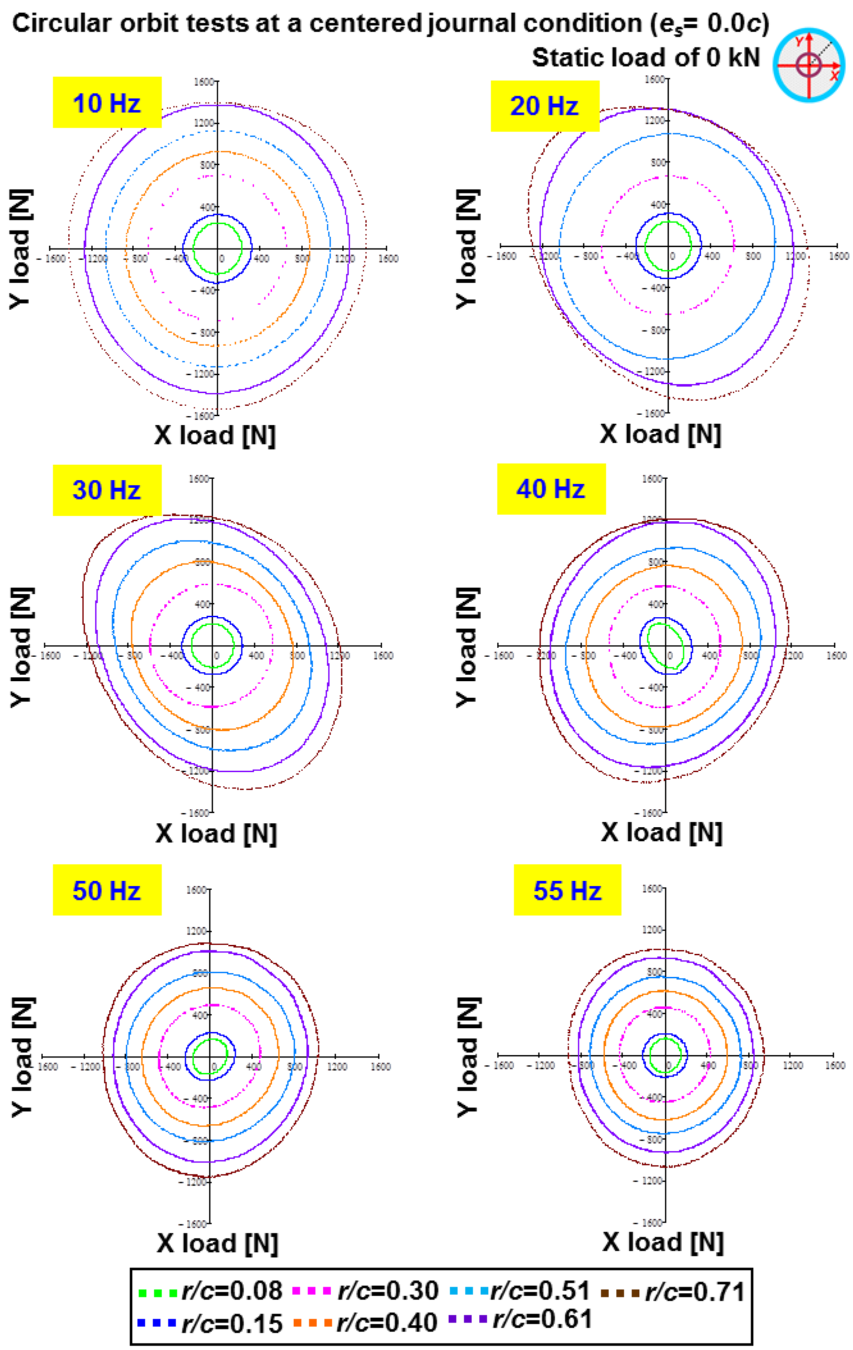

Fig. B.9 Recorded load for tests with whirl frequencies ranging from 10 to 100 Hz. Circular centered (e_s=0.0c) orbits with amplitude r=0.08c to r=0.71c. Open-ends SFD with c=251.5 μm and two 25.4 mm length film lands.

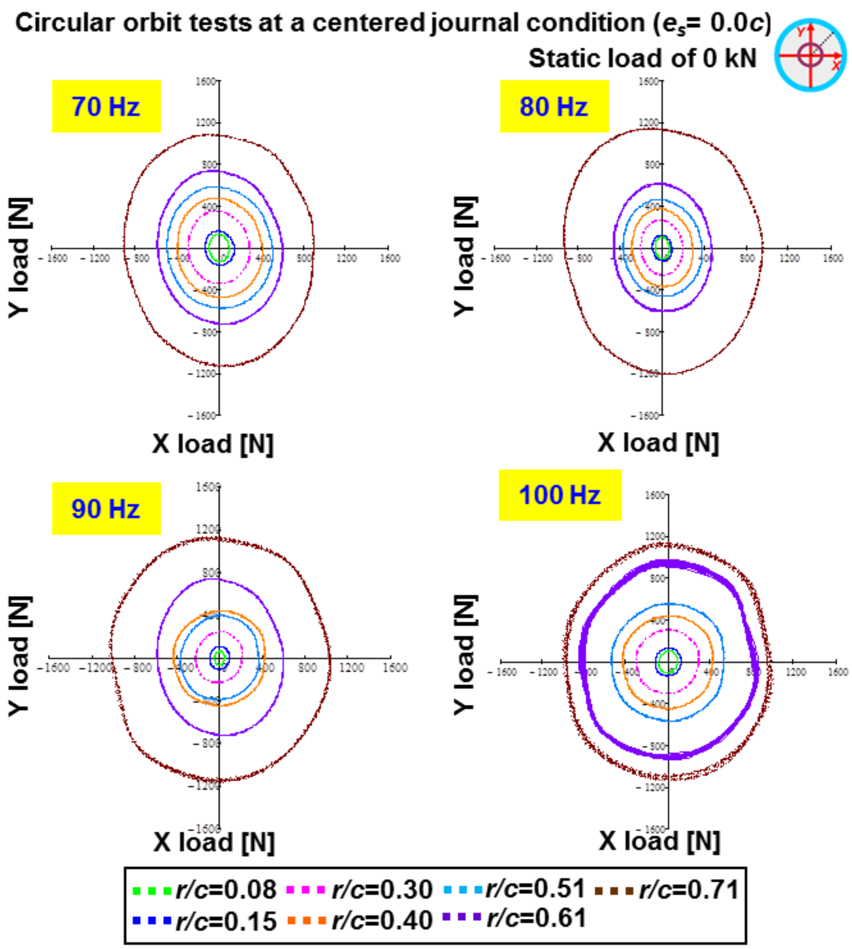

Fig. B.9 Continued.

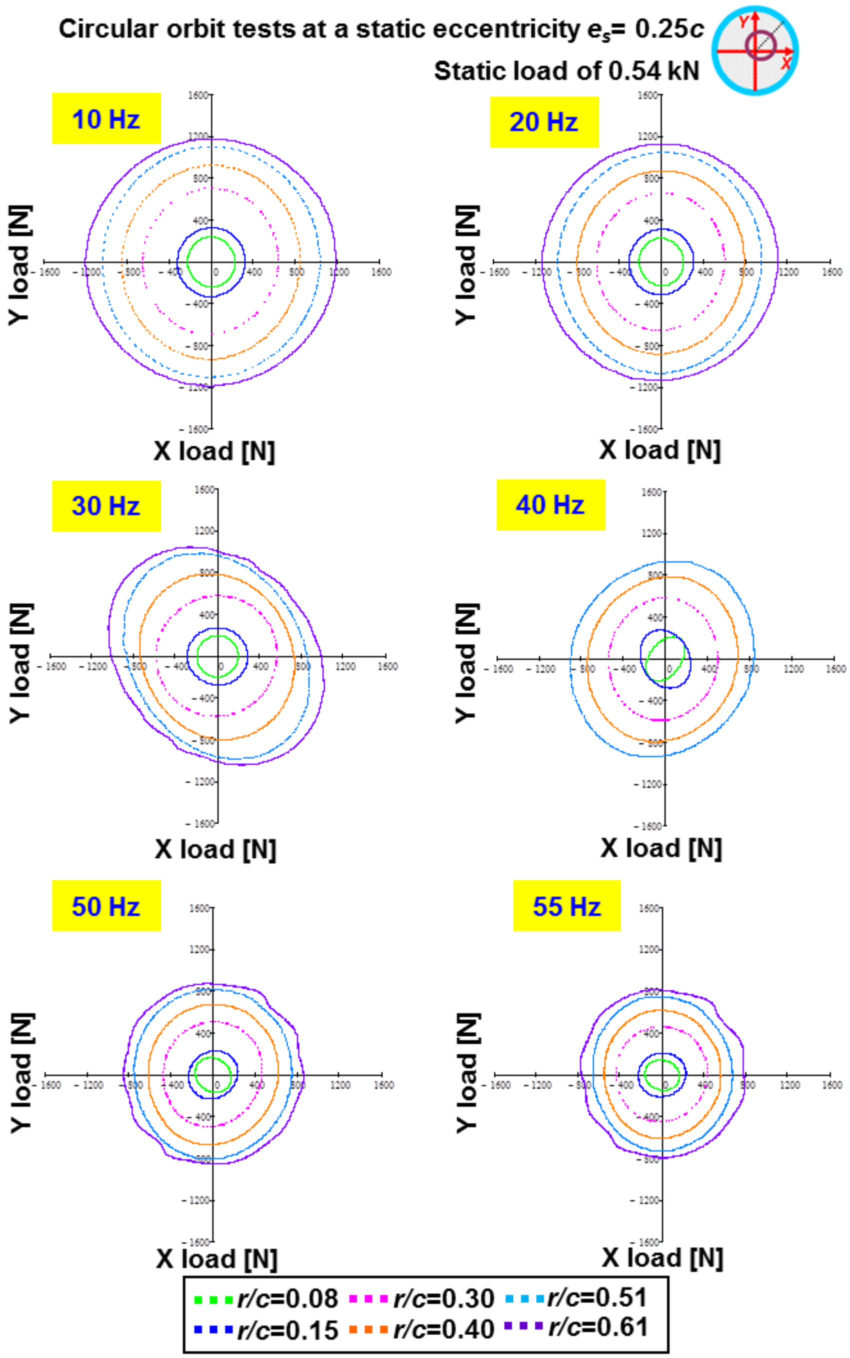

Fig. B.10 Recorded load for tests with whirl frequencies ranging from 10 to 100 Hz. Circular orbits with amplitude r=0.08c to r=0.61c at static eccentricity (e_s=0.25c). Open-ends SFD with c=251.5 μm and two 25.4 mm length film lands.

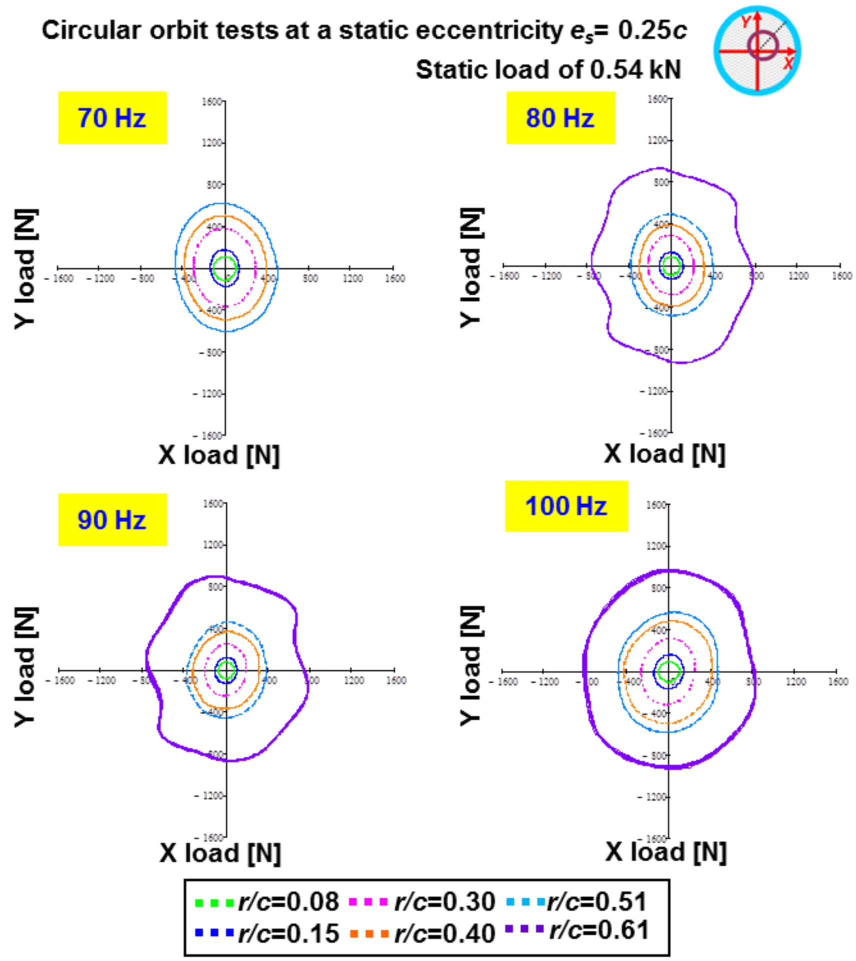

Fig. B.10 Continued.

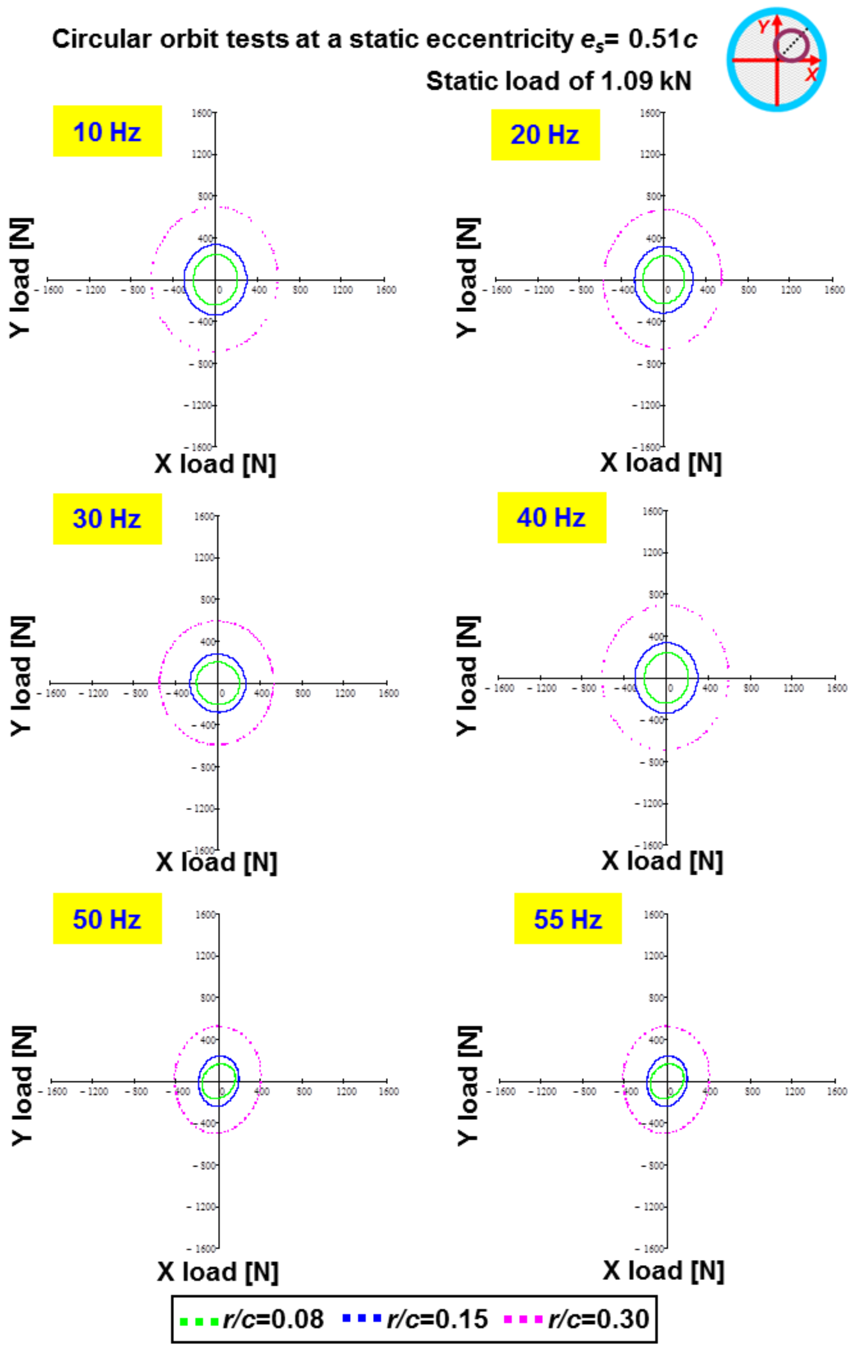

Fig. B.11 Recorded load for tests with whirl frequencies ranging from 10 to 100 Hz. Circular orbits with amplitude r=0.08c to r=0.30c at static eccentricity (e_s=0.51c). Open-ends SFD with c=251.5 μm and two 25.4 mm length film lands.

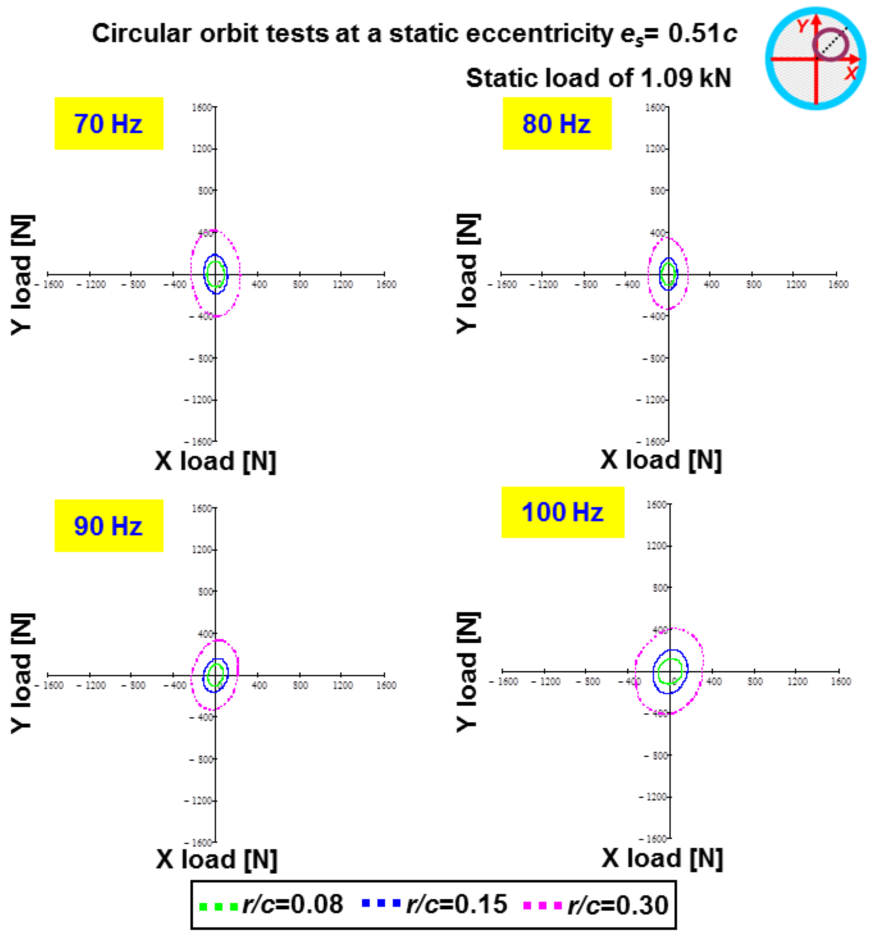

Fig. B.11 Continued.

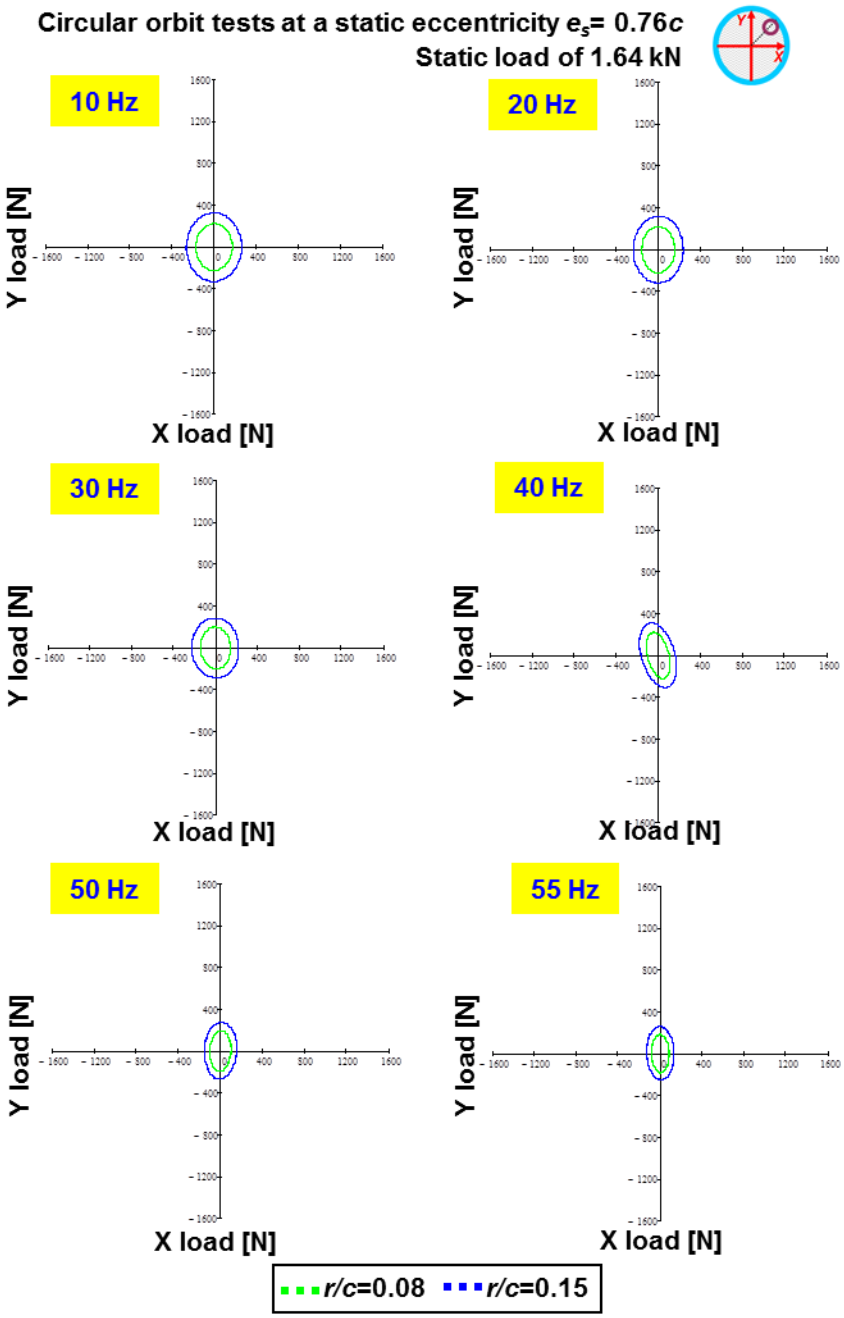

Fig. B.12 Recorded load for tests with whirl frequencies ranging from 10 to 100 Hz. Circular orbits with amplitude r=0.08c to r=0.15c at static eccentricity (e_s=0.76c). Open-ends SFD with c=251.5 μm and two 25.4 mm length film lands.

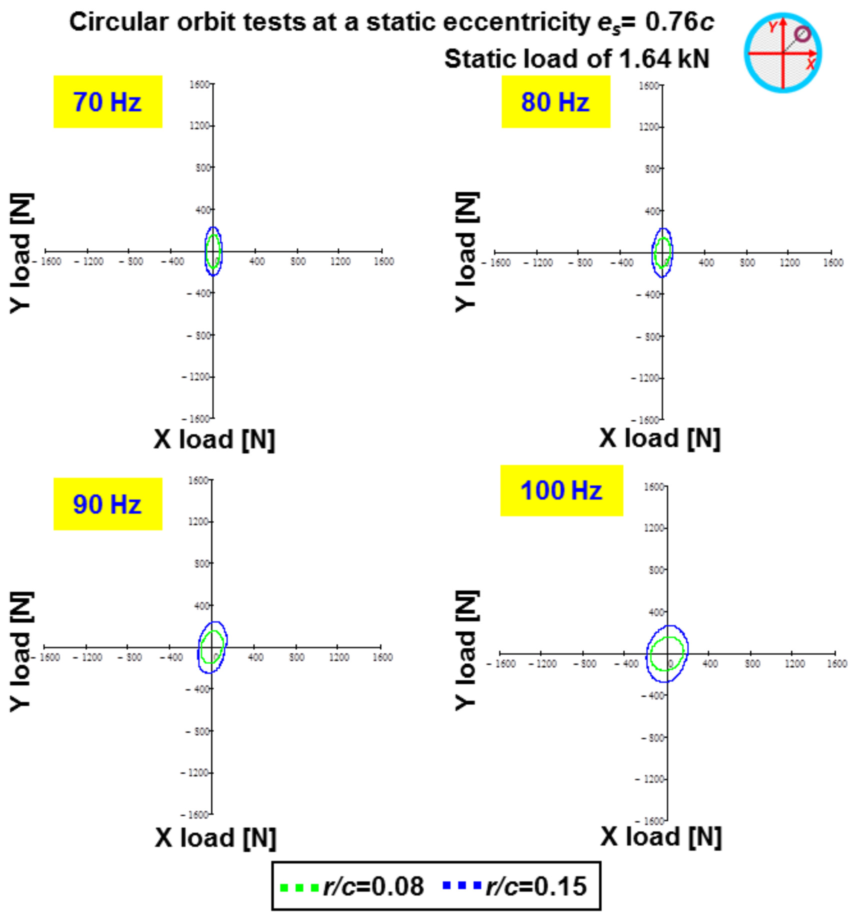

Fig. B.12 Continued.

Figures B.13 to B.16 show the Fourier coefficients of the applied load versus excitation frequency. Clearly, to induce a large orbit amplitude, larger amplitude loads are needed. For orbit amplitudes from *r/c*=0.08 to 0.61, the load amplitudes linearly drop with frequency to 80-90 Hz, and then increase. The drop and rise makes the depressed region at frequency 80-90 Hz, which turns out to be the natural frequency of the lubricated test rig. Readers are well aware of the fact that at a natural frequency, a small load is required to excite a large amplitude. However, the test system natural frequency increases with an increase in orbit amplitude (*r/c*≥0.71) due to a reduction in added mass in the SFD. Therefore, at a test with circular orbit amplitude *r/c*=0.71, the applied loads tend to increase substantially around the whirl frequency 70 – 100 Hz. Note that the natural frequency of the dry system (without lubricant) is ~114 Hz.

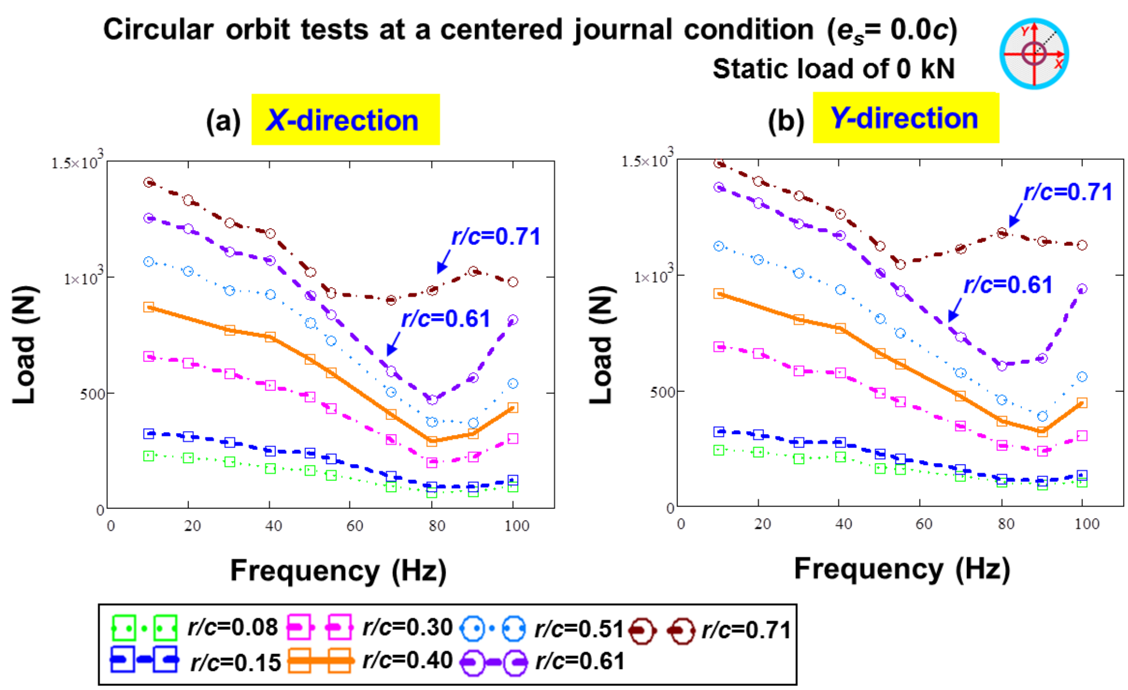

Fig. B.13 Fourier coefficients of the applied loads versus excitation frequencies ranging from 10 to 100 Hz. Tests with the circular centered (e_s=0.0*c*) orbit amplitudes *r*=0.08*c* to *r*=0.71*c*. (a) *X*-direction, (b) *Y*-direction. Open-ends SFD with *c*=251.5 μm and two 25.4 mm length film lands.

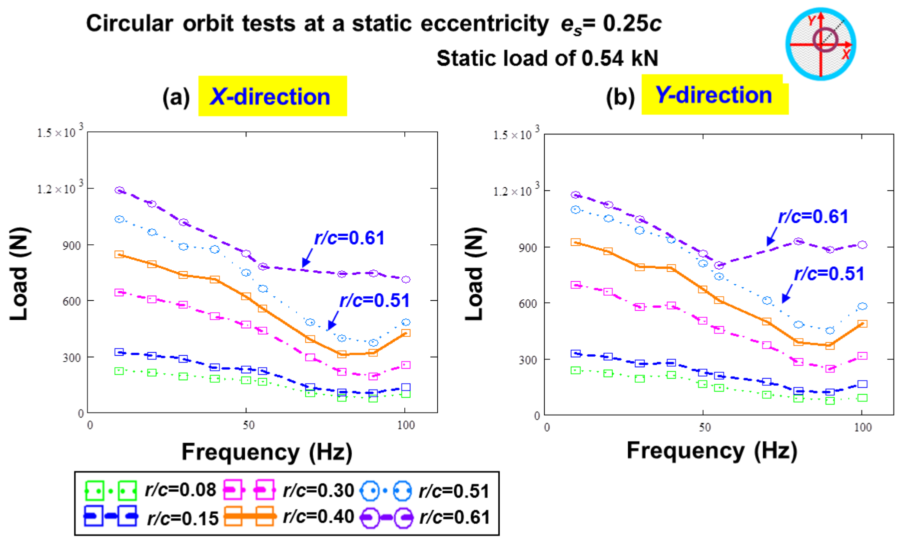

Fig. B.14 Fourier coefficients of the applied loads versus excitation frequencies ranging from 10 to 100 Hz. Tests with the circular orbit amplitudes *r*=0.08*c* to *r*=0.61*c* at static eccentricity (e_s=0.25*c*). (a) *X*-direction, (b) *Y*-direction. Open-ends SFD with *c*=251.5 μm and two 25.4 mm length film lands.

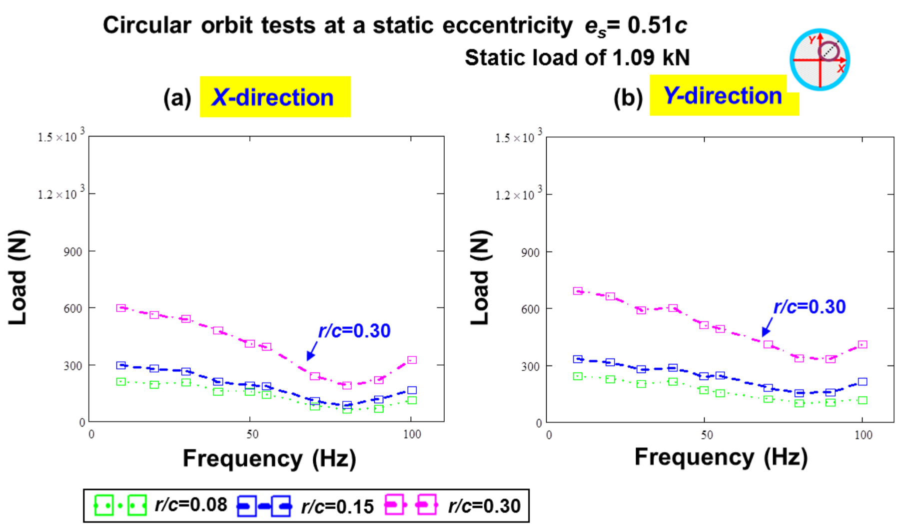

Fig. B.15 Fourier coefficients of the applied loads versus excitation frequencies ranging from 10 to 100 Hz. Tests with the circular orbit amplitudes *r*=0.08*c* to *r*=0.30*c* at static eccentricity (e_s=0.51*c*). (a) *X*-direction, (b) *Y*-direction. Open-ends SFD with *c*=251.5 μm and two 25.4 mm length film lands.

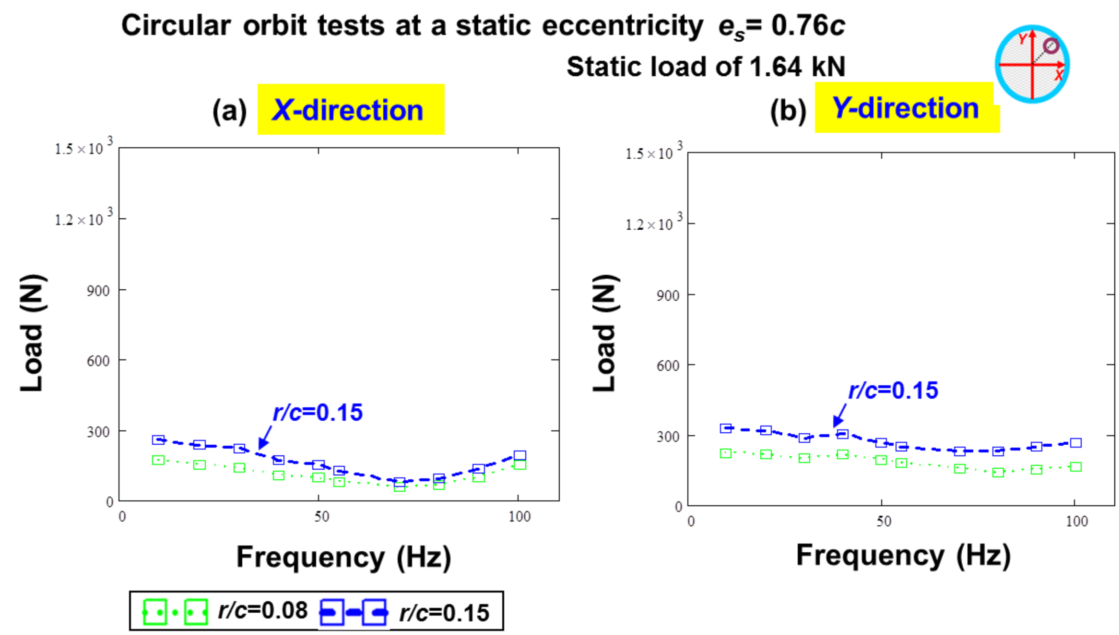

Fig. B.16 Fourier coefficients of the applied loads versus excitation frequencies ranging from 10 to 100 Hz. Tests with the circular orbit amplitudes *r*=0.08*c* to *r*=0.15*c* at static eccentricity (e_s=0.76*c*). (a) *X*-direction, (b) *Y*-direction. Open-ends SFD with *c*=251.5 μm and two 25.4 mm length film lands.

APPENDIX C

DYNAMIC IMPEDANCES FOR CIRCULAR ORBITS TESTS

Figures C.1 through C.6 show the real and the imaginary parts of the direct dynamic impedances (H_{XX}, H_{YY}) for circular orbit tests with increasing orbit amplitudes (r/c) and static eccentric positions (e_s/c). Note that the frequency range for the respective physical model curve fits spans from f_{start}=10 Hz to f_{end}=100 Hz.

Figures C.7 to C.14 present the cross-coupled dynamic impedances (H_{XY}, H_{YX}). The SFD cross-coupled coefficient magnitudes are more than one order smaller than the direct coefficient for small journal static eccentricity $e_s/c \leq 0.25$, hence showing low correlation factor (R^2) to the respective physical model. However, the estimated SFD cross-coupled damping (C_{XY}, C_{YX}) and added mass coefficients (M_{XY}, M_{YX}) increase as large as same order magnitudes of direct coefficients for moderate to large static eccentricities $e_s/c \geq 0.51$ and thus resulting in an increase of the goodness of fits (R^2).

1. Direct dynamic impedance (H)

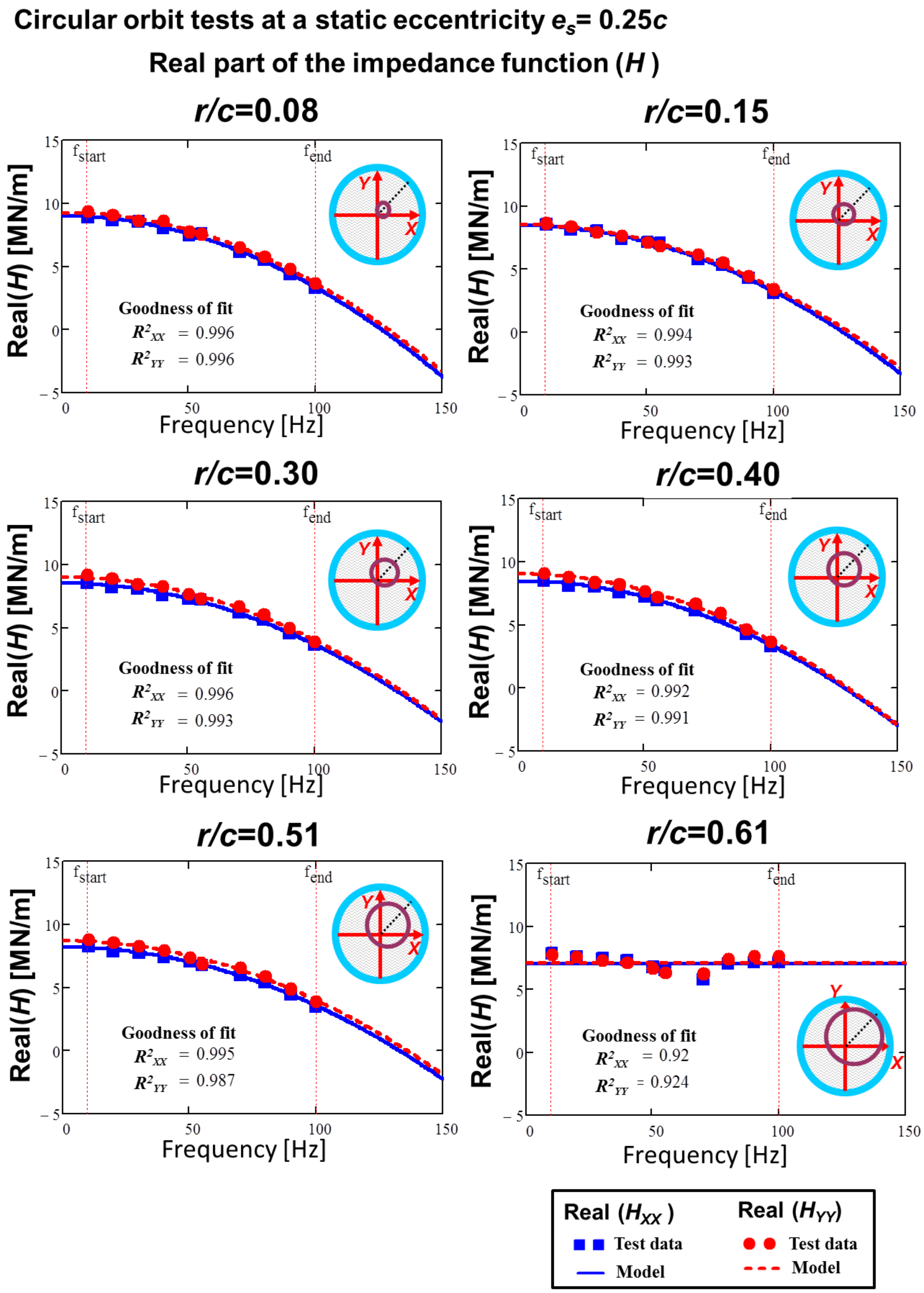

Fig. C.1 Real part of the test system direct impedances (H_{XX}, H_{YY}) versus excitation frequency. Tests with orbit amplitudes r/c=0.08 - 0.61 at static eccentricity (e_S=0.25c). Test data and the model fits. Open-ends SFD with c=251.5 μm and two 25.4 mm length film lands.

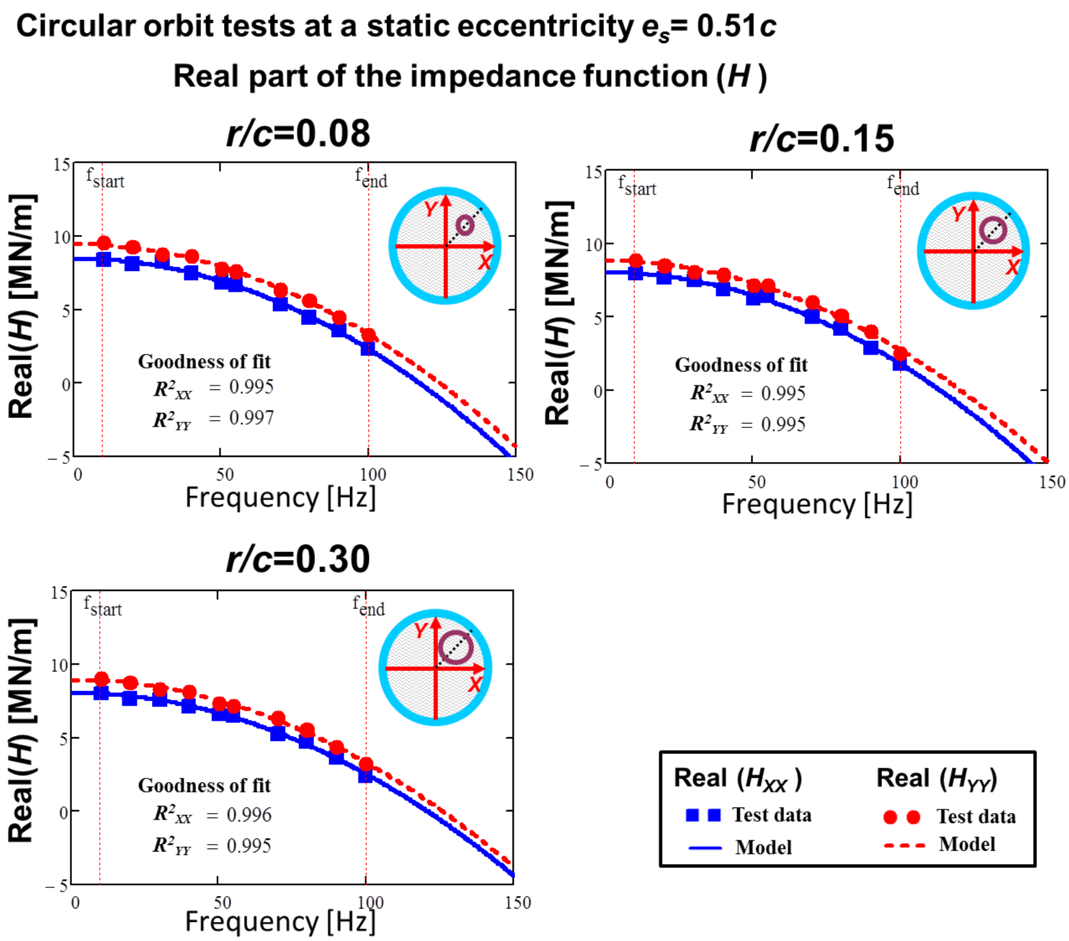

Fig. C.2 Real part of the test system direct impedances (H_{XX}, H_{YY}) versus excitation frequency. Tests with orbit amplitudes r/c=0.08 - 0.30 at static eccentricity (e_S=0.51c). Test data and the model fits. Open-ends SFD with c=251.5 μm and two 25.4 mm length film lands.

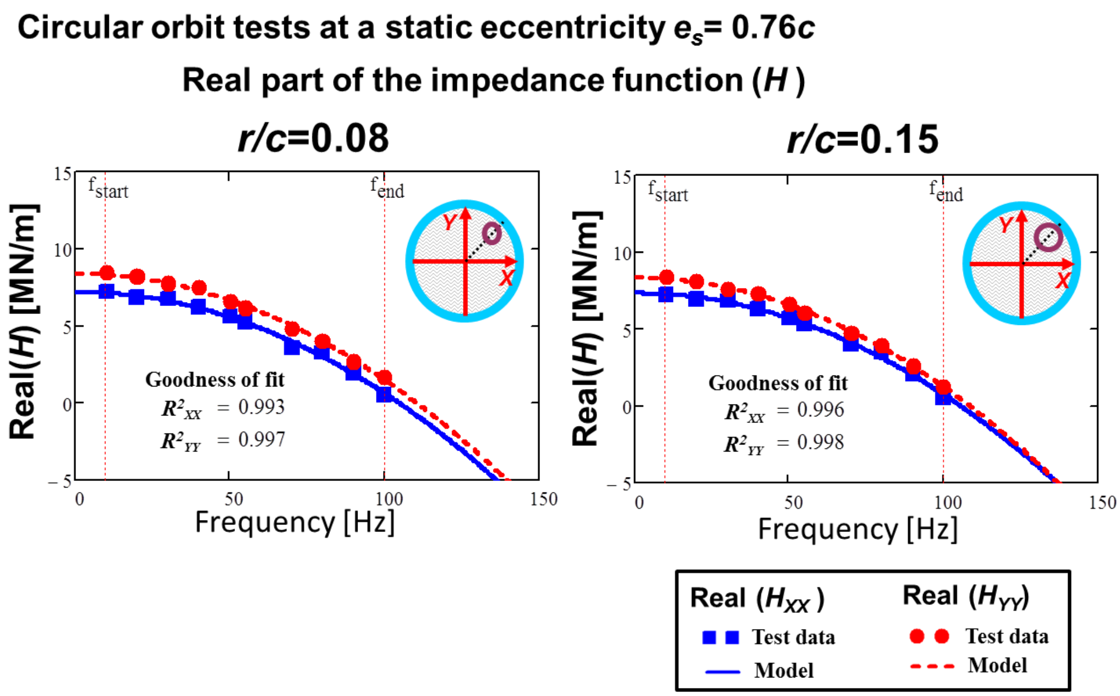

Fig. C.3 Real part of the test system direct impedances (H_{XX}, H_{YY}) versus excitation frequency. Tests with orbit amplitudes *r/c*=0.08 - 0.15 at static eccentricity (e_S=0.76*c*). Test data and the model fits. Open-ends SFD with *c*=251.5 μm and two 25.4 mm length film lands.

Circular orbit tests at a static eccentricity e_s= 0.25c
Imaginary part of the impedance function (H)

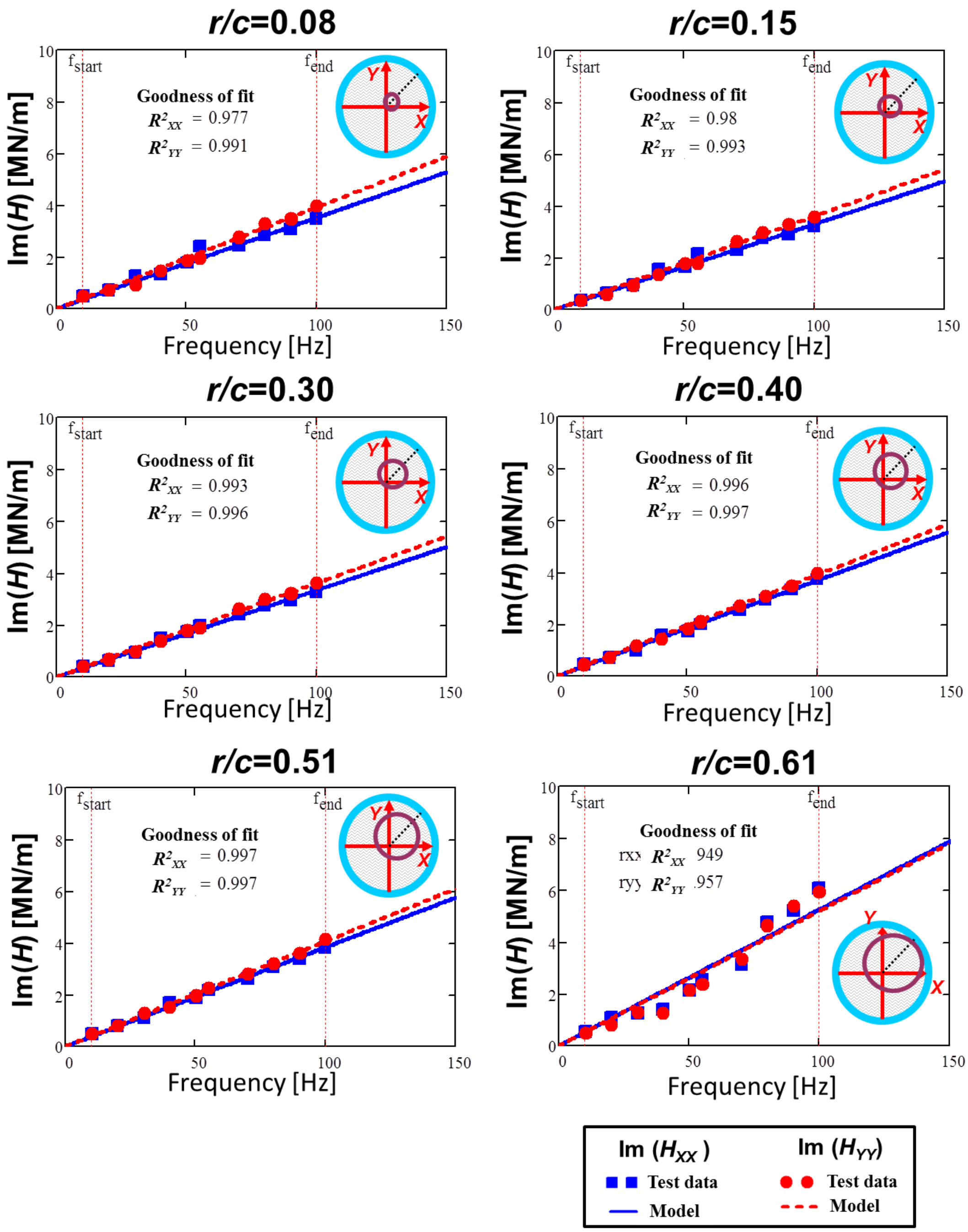

Fig. C.4 Imaginary part of the test system direct impedances (H_{XX}, H_{YY}) versus excitation frequency. Tests with orbit amplitudes r/c=0.08 - 0.61 at circular centered orbit (e_S=0.25c). Test data and the model fits. Open-ends SFD with c=251.5 µm and two 25.4 mm length film lands.

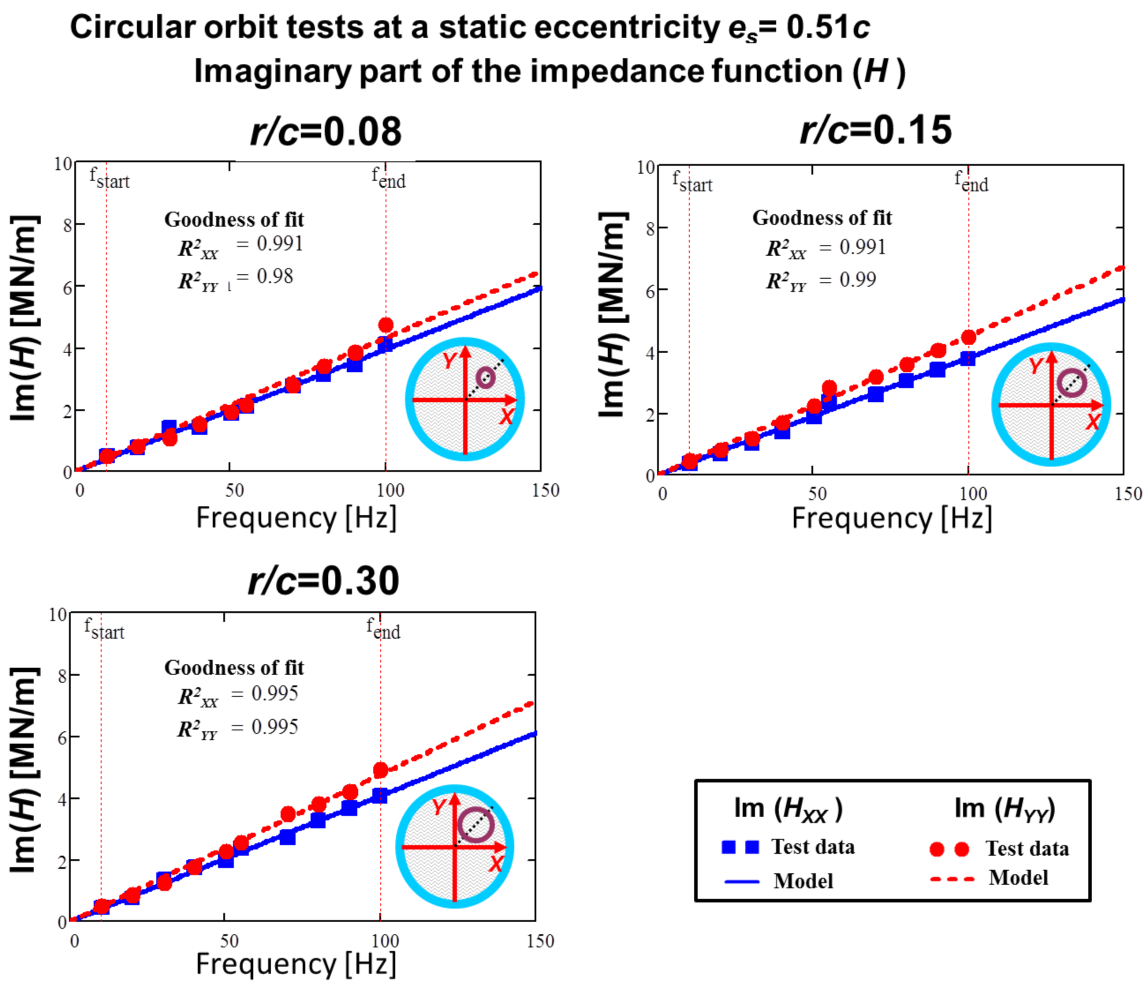

Fig. C.5 Imaginary part of the test system direct impedances (H_{XX}, H_{YY}) versus excitation frequency. Tests with orbit amplitudes r/c=0.08 - 0.30 at circular centered orbit (e_S=0.51c). Test data and the model fits. Open-ends SFD with c=251.5 μm and two 25.4 mm length film lands.

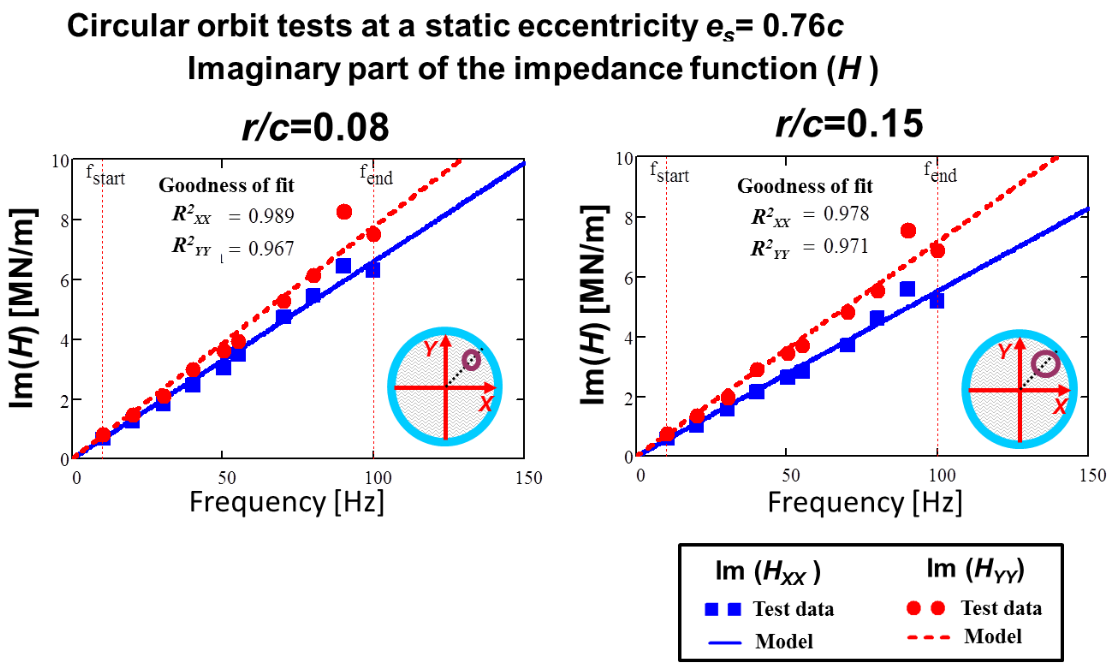

Fig. C.6 Imaginary part of the test system direct impedances (H_{XX}, H_{YY}) versus excitation frequency. Tests with orbit amplitudes r/c=0.08 - 0.15 at circular centered orbit (e_S=0.76c). Test data and the model fits. Open-ends SFD with c=251.5 μm and two 25.4 mm length film lands.

2. Cross-coupled dynamic impedance (H)

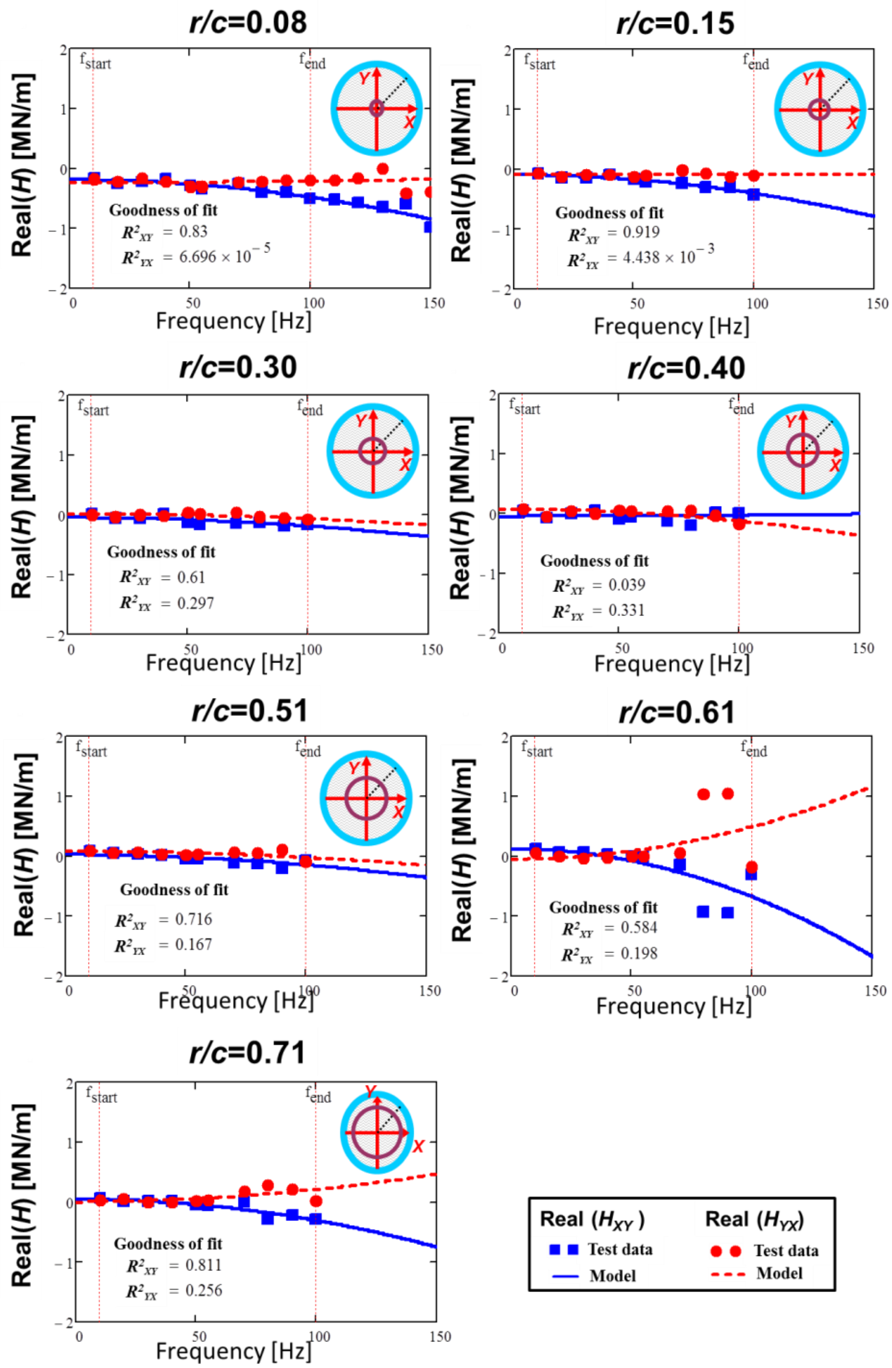

Fig. C.7 Real part of the test system cross-coupled impedances (H_{XY}, H_{YX}) versus excitation frequency. Tests with circular orbits with amplitudes *r/c*=0.08 - 0.71 and centered condition (e_S=0.0*c*). Test data and model fits. Open-ends grooved SFD with *c*=251.5 μm ad two 25.4 mm length film lands.

Circular orbit tests at a static eccentricity e_s= 0.25*c*

Real part of the impedance function (*H*)

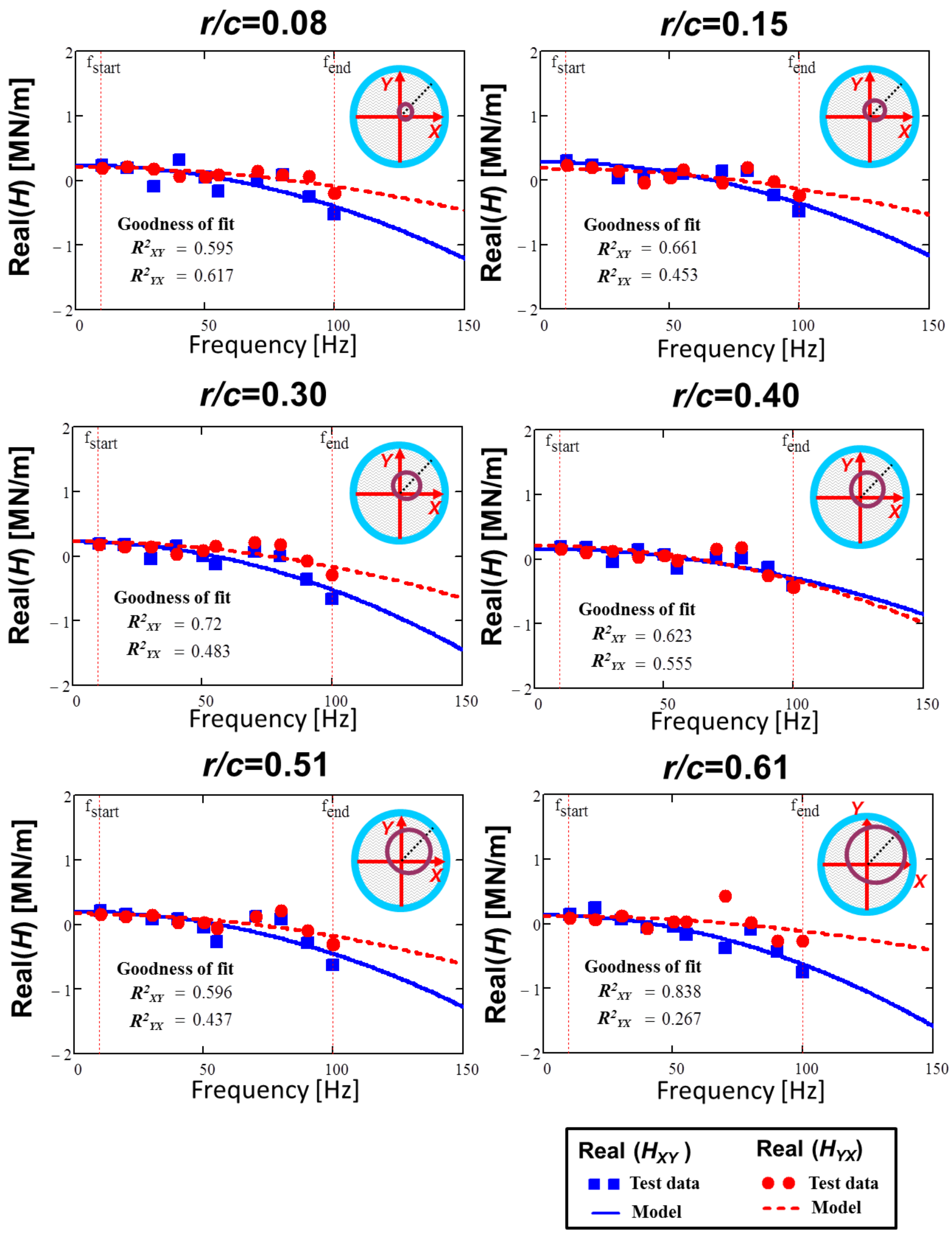

Fig. C.8 Real part of the test system cross-coupled impedances (H_{XY}, H_{YX}) versus excitation frequency. Tests with orbit amplitudes *r/c*=0.08 - 0.61 at static eccentricity (e_S=0.25*c*). Test data and the model fits. Open-ends SFD with *c*=251.5 µm and two 25.4 mm length film lands.

Circular orbit tests at a static eccentricity e_s= 0.51c

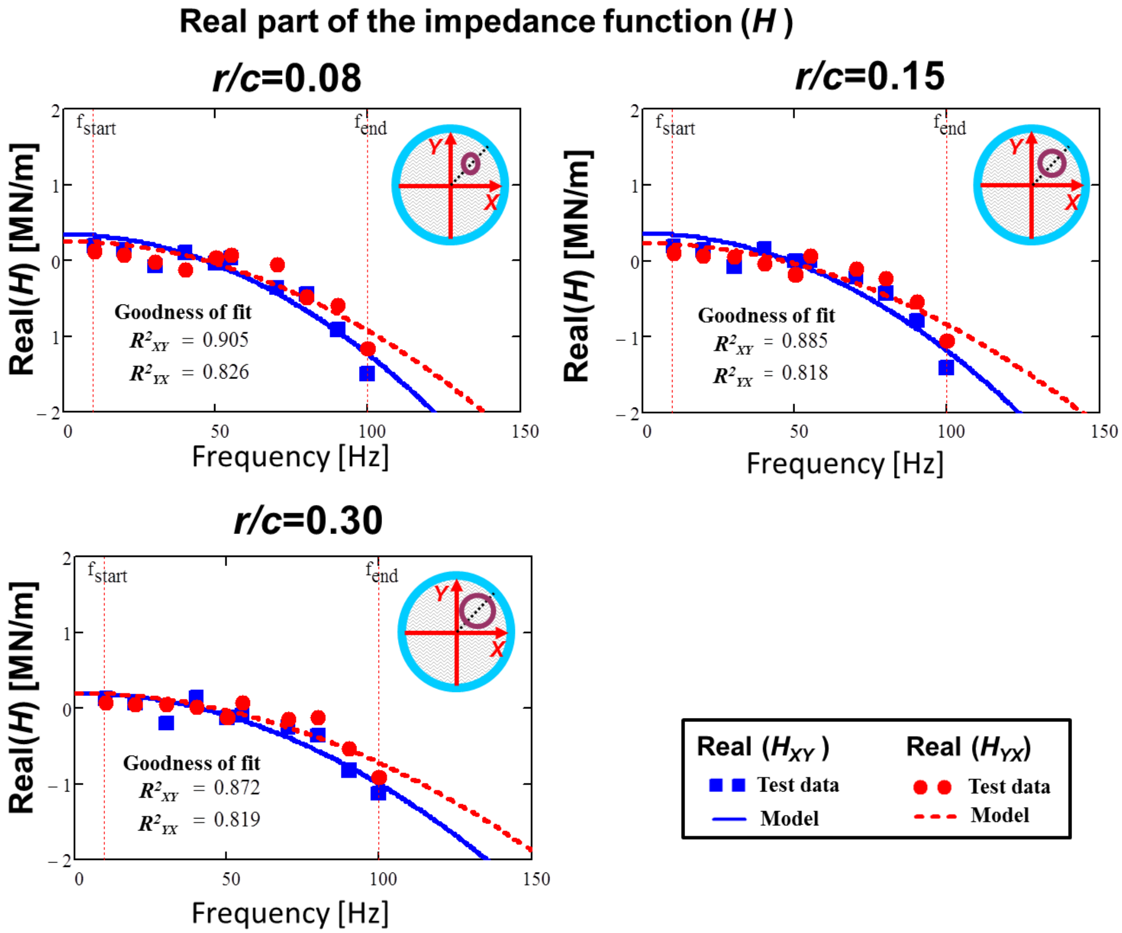

Fig. C.9 Real part of the test system cross-coupled impedances (H_{XY}, H_{YX}) versus excitation frequency. Tests with orbit amplitudes r/c=0.08 - 0.30 at static eccentricity (e_S=0.51c). Test data and the model fits. Open-ends SFD with c=251.5 μm and two 25.4 mm length film lands.

Circular orbit tests at a static eccentricity e_s= 0.76c

Real part of the impedance function (H)

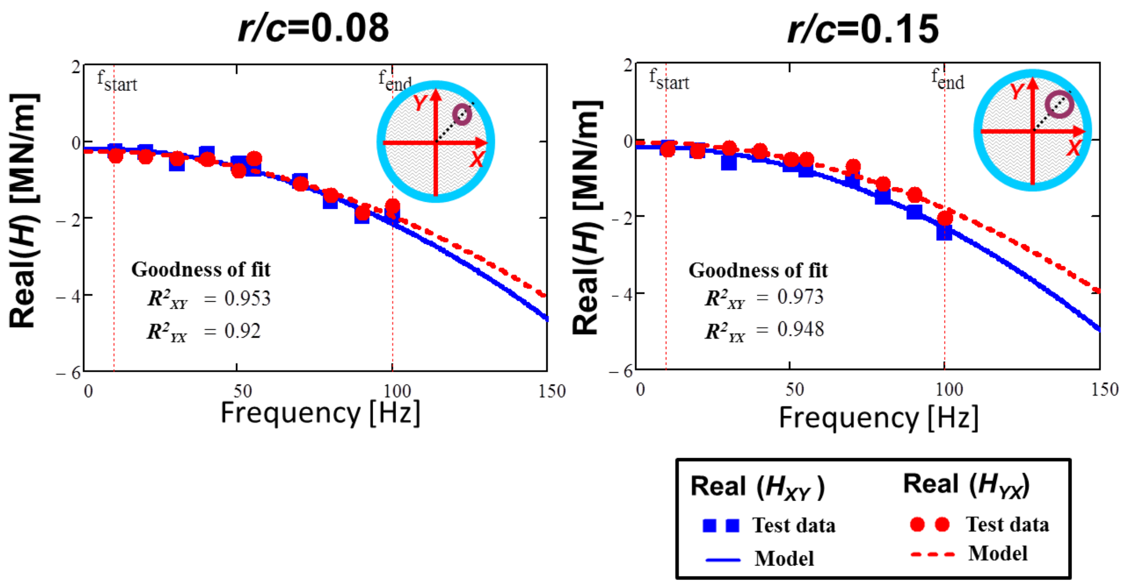

Fig.C.10 Real part of the test system cross-coupled impedances (H_{XY}, H_{YX}) versus excitation frequency. Tests with orbit amplitudes r/c=0.08 - 0.15 at static eccentricity (e_S=0.76c). Test data and the model fits. Open-ends SFD with c=251.5 μm and two 25.4 mm length film lands.

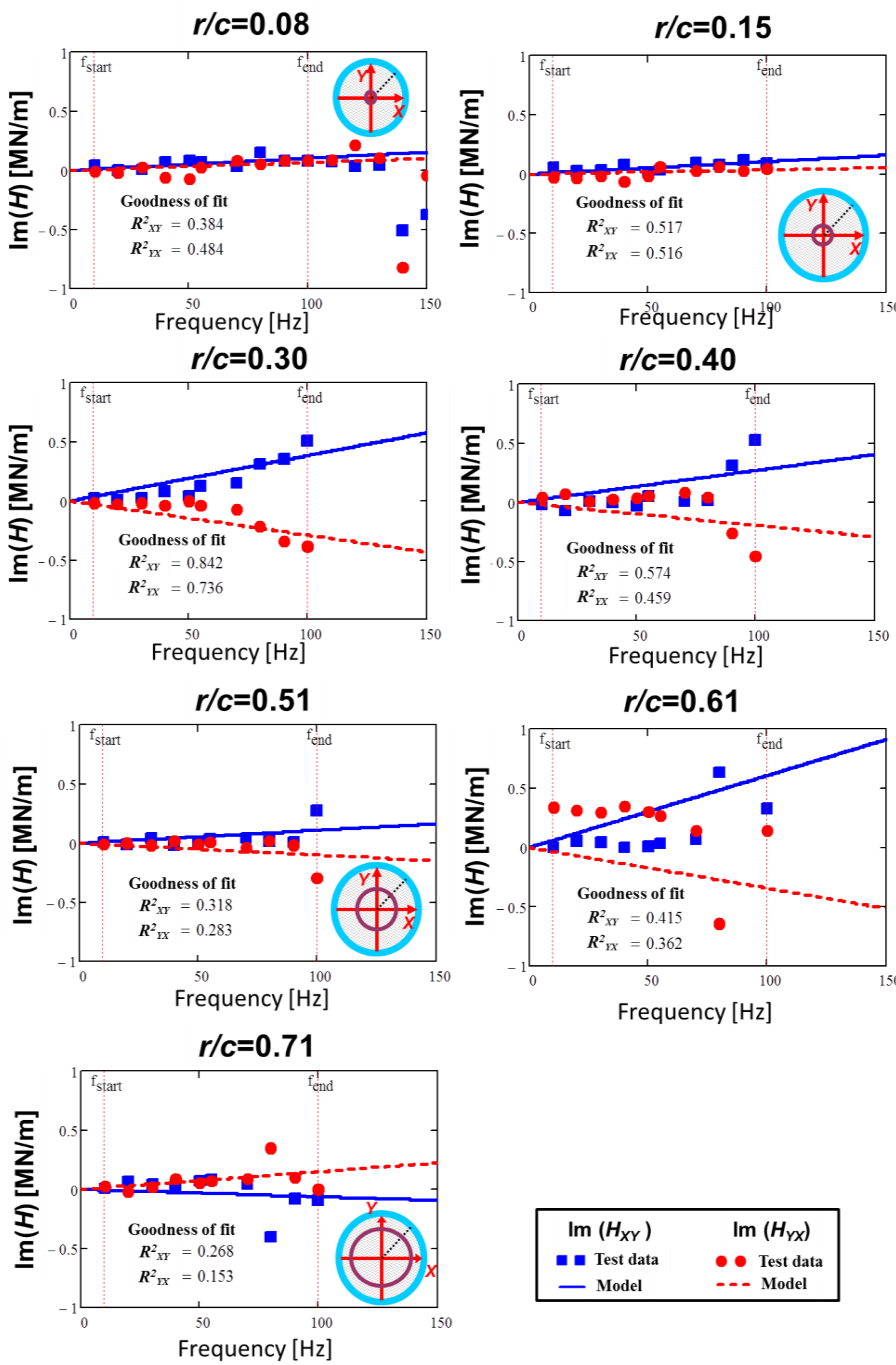

Fig.C.11 Imaginary part of the test system cross-coupled impedances (H_{XY}, H_{YX}) versus excitation frequency. Tests with circular orbits with amplitudes r/c=0.08 - 0.71 and centered condition (e_S=0.0c). Test data and model fits. Open-ends grooved SFD with c=251.5 μm and two 25.4 mm length film lands.

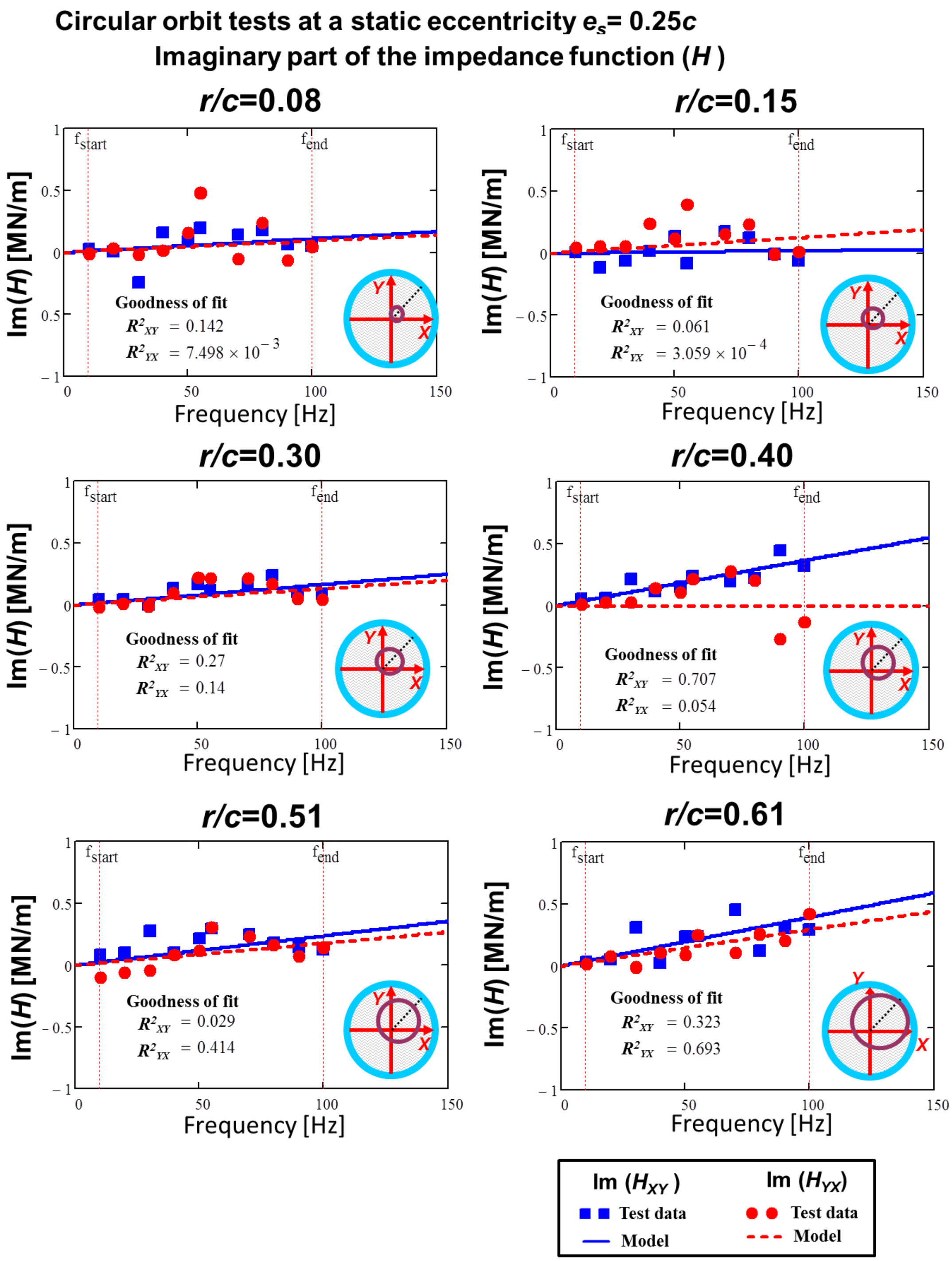

Fig. C.12 Imaginary part of the test system cross-coupled impedances (H_{XY}, H_{YX}) versus excitation frequency. Tests with orbit amplitudes *r/c*=0.08 - 0.61 at circular centered orbit (e_S=0.25*c*). Test data and the model fits. Open-ends SFD with *c*=251.5 μm and two 25.4 mm length film lands.

Circular orbit tests at a static eccentricity e_s= 0.51c
Imaginary part of the impedance function (H)

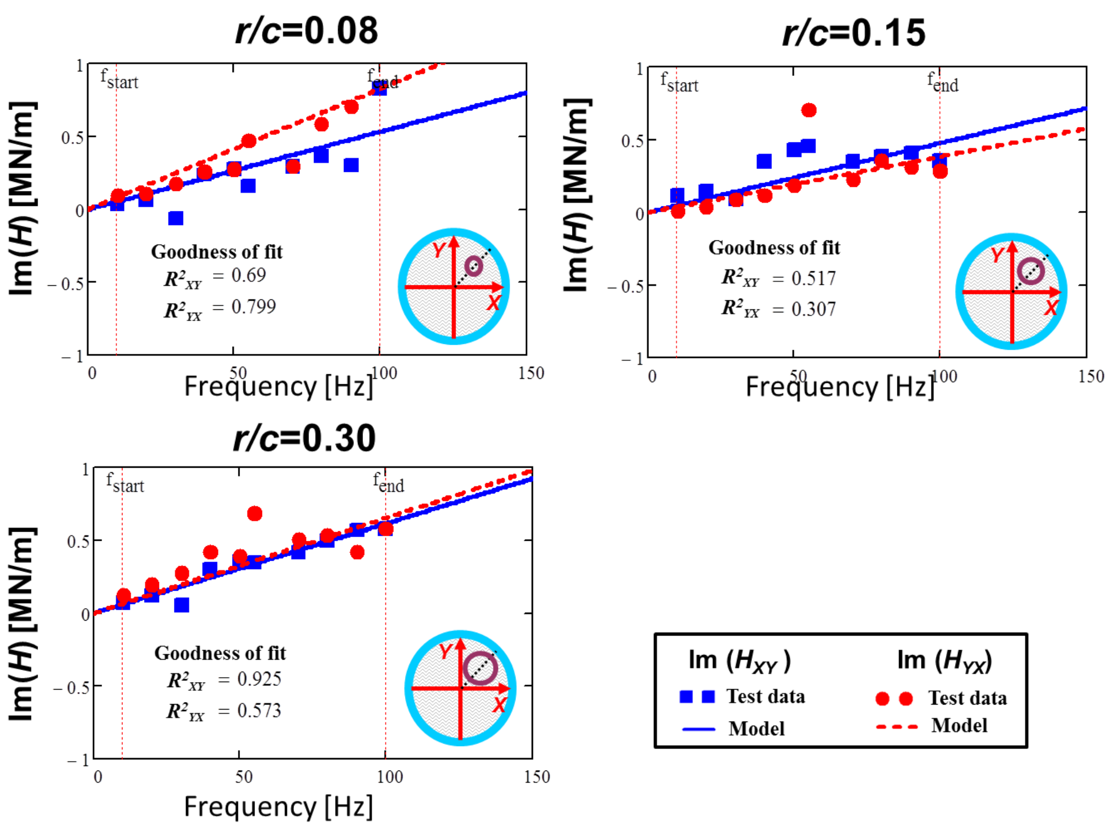

Fig. C.13 Imaginary part of the test system cross-coupled impedances (H_{XY}, H_{YX}) versus excitation frequency. Tests with orbit amplitudes r/c=0.08 - 0.30 at circular centered orbit (e_S=0.51c). Test data and the model fits. Open-ends SFD with c=251.5 μm and two 25.4 mm length film lands.

Circular orbit tests at a static eccentricity e_s= 0.76c
Imaginary part of the impedance function (H)

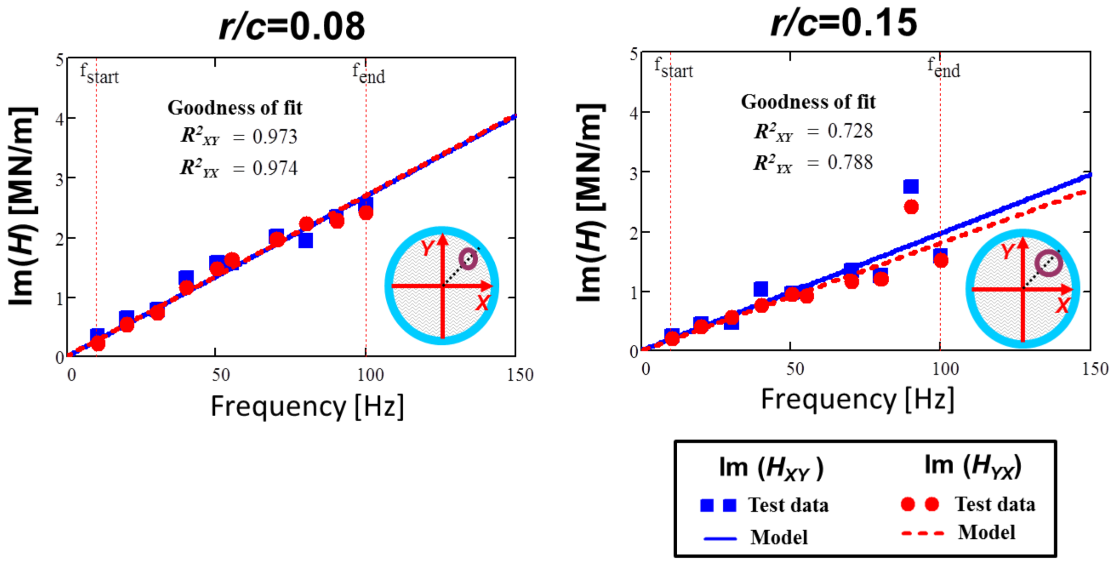

Fig. C.14 Imaginary part of the test system cross-coupled impedances (H_{XY}, H_{YX}) versus excitation frequency. Tests with orbit amplitudes r/c=0.08 - 0.15 at circular centered orbit (e_S=0.76c). Test data and the model fits. Open-ends SFD with c=251.5 μm and two 25.4 mm length film lands.

APPENDIX D

DYNAMIC PRESSURE IN THE FILM LANDS AND GROOVE FOR OPEN ENDS SFD

Figures D.1 to D.3 show the measured dynamic peak-to-peak (p-p) pressures in the both film lands and in the central groove for circular orbit tests with increasing orbit radii at three different static eccentricities, e_s/c=0.0 to 0.76. Measured peak-to-peak pressures in the both top and bottom film lands and the groove increase with larger orbit amplitudes.

Figures D.4 to D.6 show the pressure profiles in the groove and the film lands at a whirl frequency 100 Hz for circular orbit tests with increasing orbit radii at three different static eccentricities, e_s/c=0.25 to 0.76. The magnitude of the dynamic pressures in the groove and the film lands increase with increasing orbit amplitudes. The groove pressures measured at locations of 165° and 285° show identical magnitudes. Measured dynamic pressures show a single frequency waveform until the orbit amplitude reaches r=0.51c. For larger orbit amplitudes, above r>0.61c, the pressure waveforms show both sudden spikes and a flat zone. Overall, the amplitude of the lubricant dynamic pressure in the groove pressure is lower than in the film lands.

Figures D.7 through D.9 present the normalized peak-to-peak dynamic pressures $\overline{P}$ reproducing data in Figures D.1 to D.3. Regardless of the circular orbit size the $\overline{P}$ in the groove converges in to a single slope whereas the $\overline{P}$ in both film lands increase with increasing orbit amplitudes. However, as the static eccentricity (e_s) increases, increase of fluid viscous contribution ($\overline{P}_{viscous} \sim constant$) on the groove dynamic pressures (θ=165º, 285º) and fluid inertia effect ($\overline{P}_{inertial} \sim \omega$) on the film land dynamic pressures (θ=120º) are observed. This is most likely due to the radial clearance between the journal and the BC decreases at the location of pressure sensors measuring the groove (θ=165º, 285º) whereas the radial clearance increases at θ=120º. Note that influence of fluid viscous effect on lubricant dynamic pressure is larger when the radial clearance gets smaller. Recall that the location of the dynamic pressure sensors in the BC (see Figure 22).

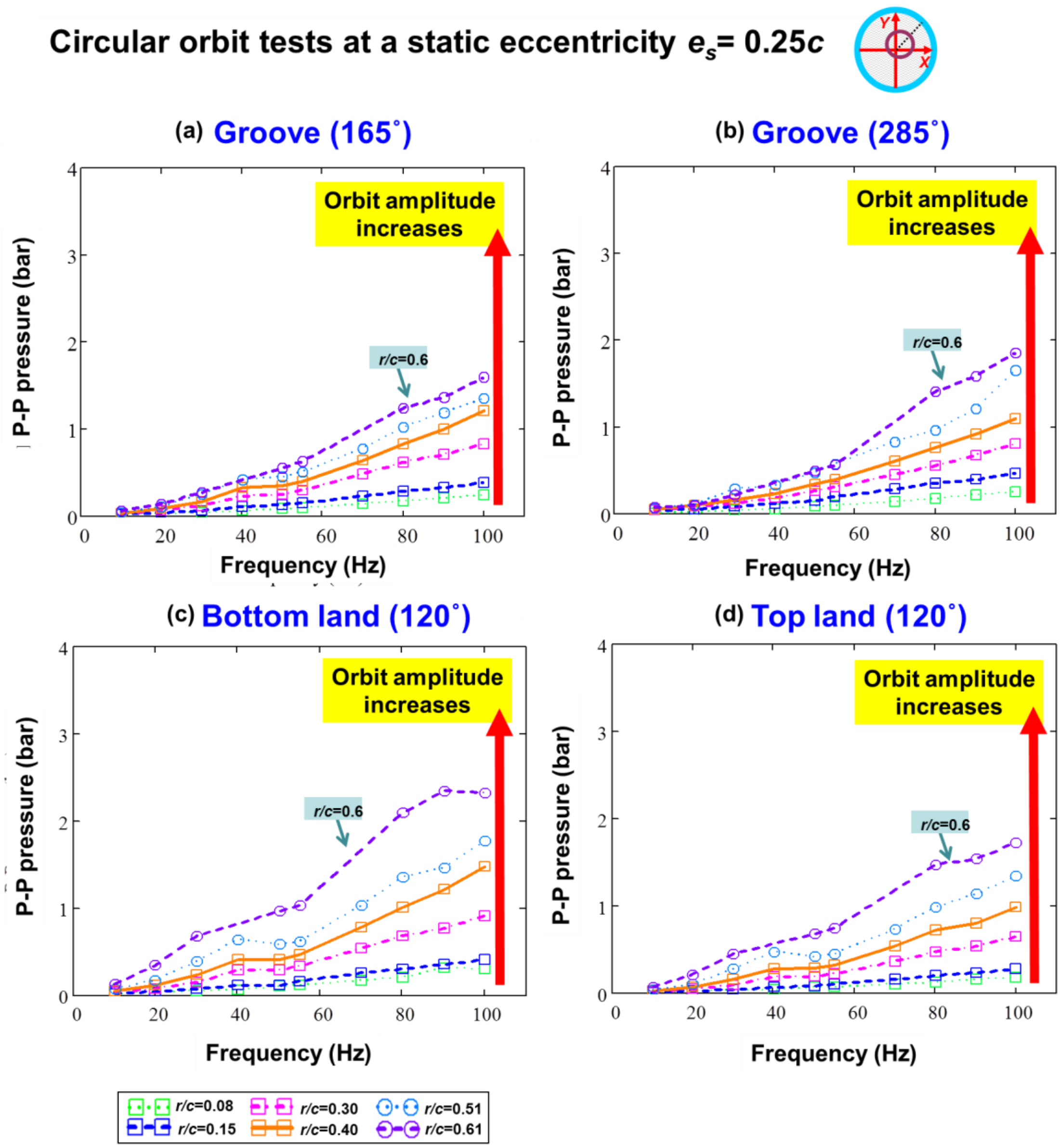

Fig. D.1 Peak-peak dynamic pressure versus excitation frequency. Tests with orbit amplitudes r/c=0.08 - 0.71 at static eccentricity (e_S=0.25c): at (a) groove (165˚), (b) groove (285˚), (c) bottom film lands (120˚) and (d) top film lands (120˚). Open-ends SFD with c=251.5 μm and two 25.4 mm length film lands.

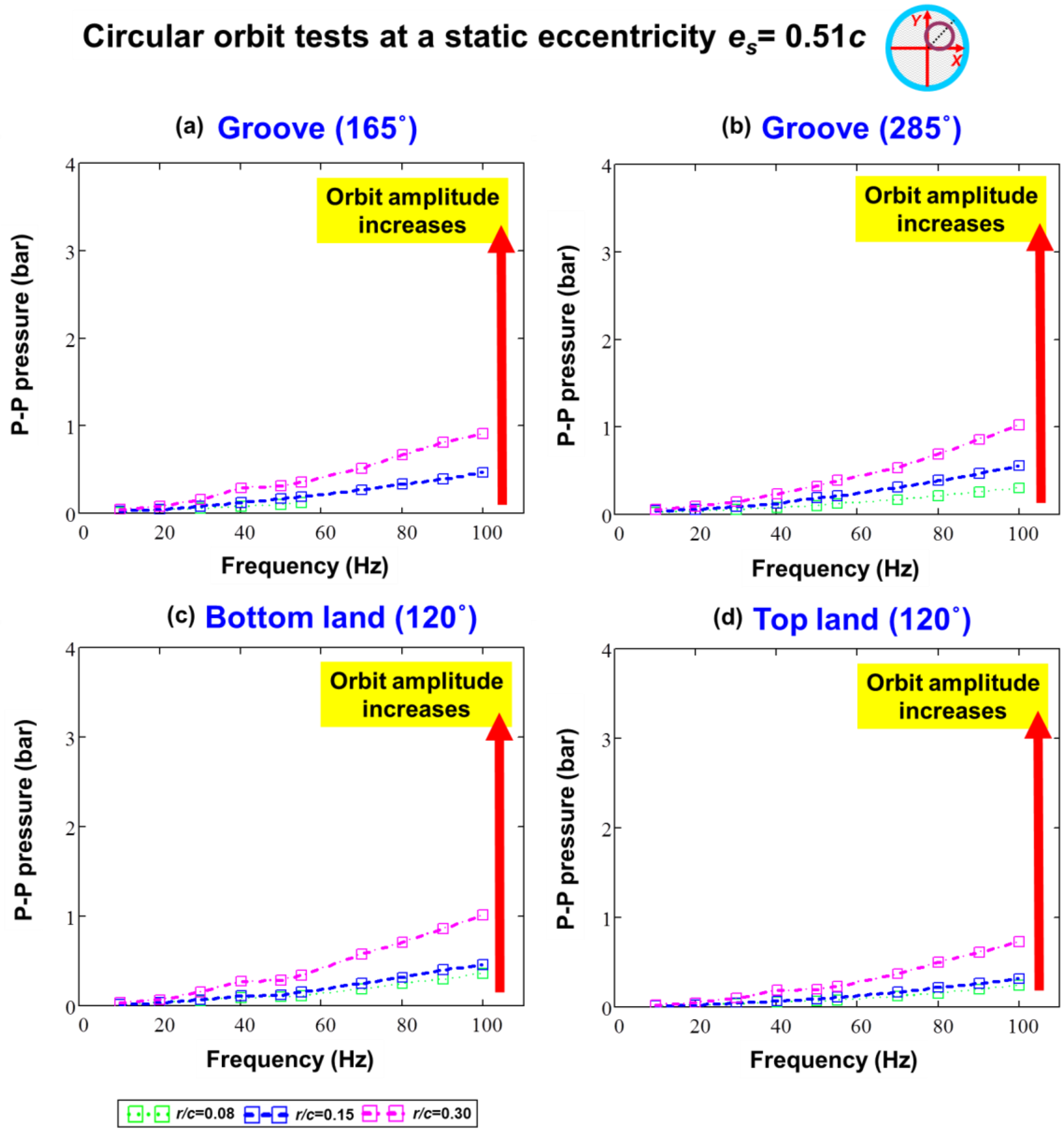

Fig. D.2 Peak-peak dynamic pressure versus excitation frequency. Tests with orbit amplitudes *r/c*=0.08 - 0.71 at static eccentricity (e_S=0.51*c*): at (a) groove (165˚), (b) groove (285˚), (c) bottom film lands (120˚) and (d) top film lands (120˚). Open-ends SFD with *c*=251.5 μm and two 25.4 mm length film lands.

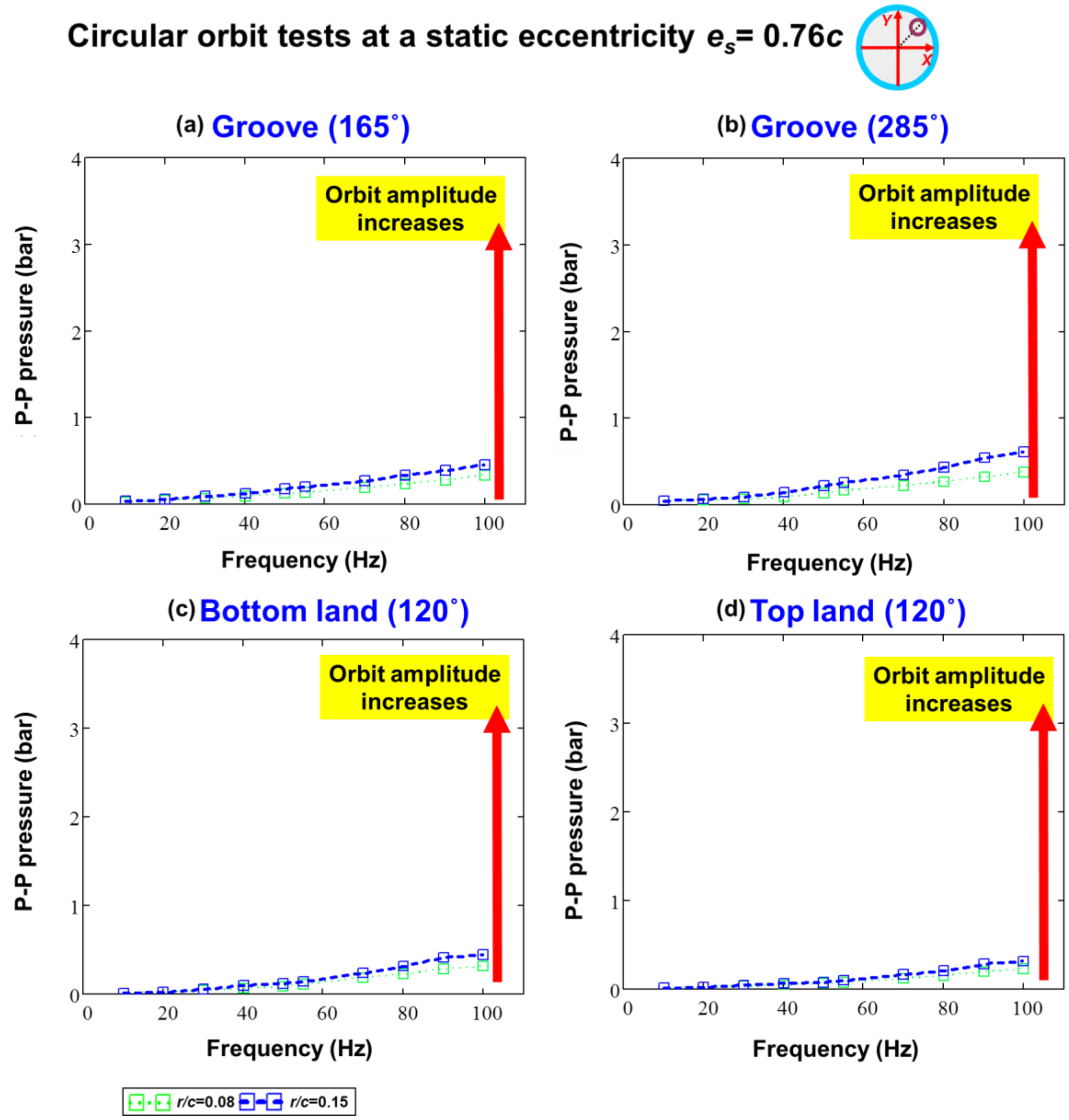

Fig. D.3 Peak-peak dynamic pressure versus excitation frequency. Tests with orbit amplitudes r/c=0.08 - 0.71 at static eccentricity (e_S=0.76c): at (a) groove (165˚), (b) groove (285˚), (c) bottom film lands (120˚) and (d) top film lands (120˚). Open-ends SFD with c=251.5 μm and two 25.4 mm length film lands.

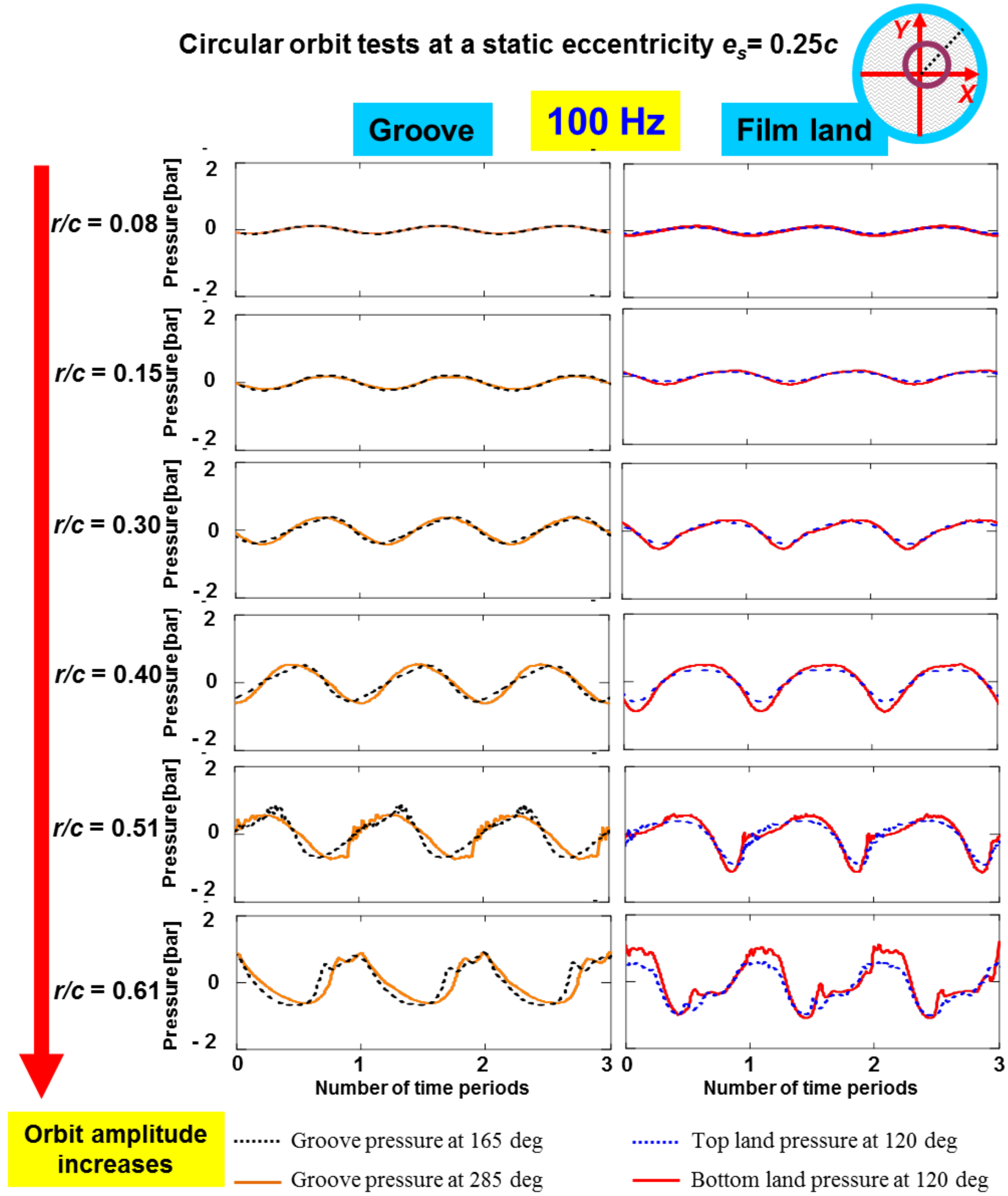

Fig. D.4 Lubricant dynamic pressures in the groove and the film lands versus number of time periods. Tests with circular orbit amplitudes *r*=0.08*c* to *r*=0.61*c* at static eccentricity e_S=0.25*c* and at a whirl frequency 100 Hz. Open-ends SFD with *c*=251.5 μm and two 25.4 mm length film lands.

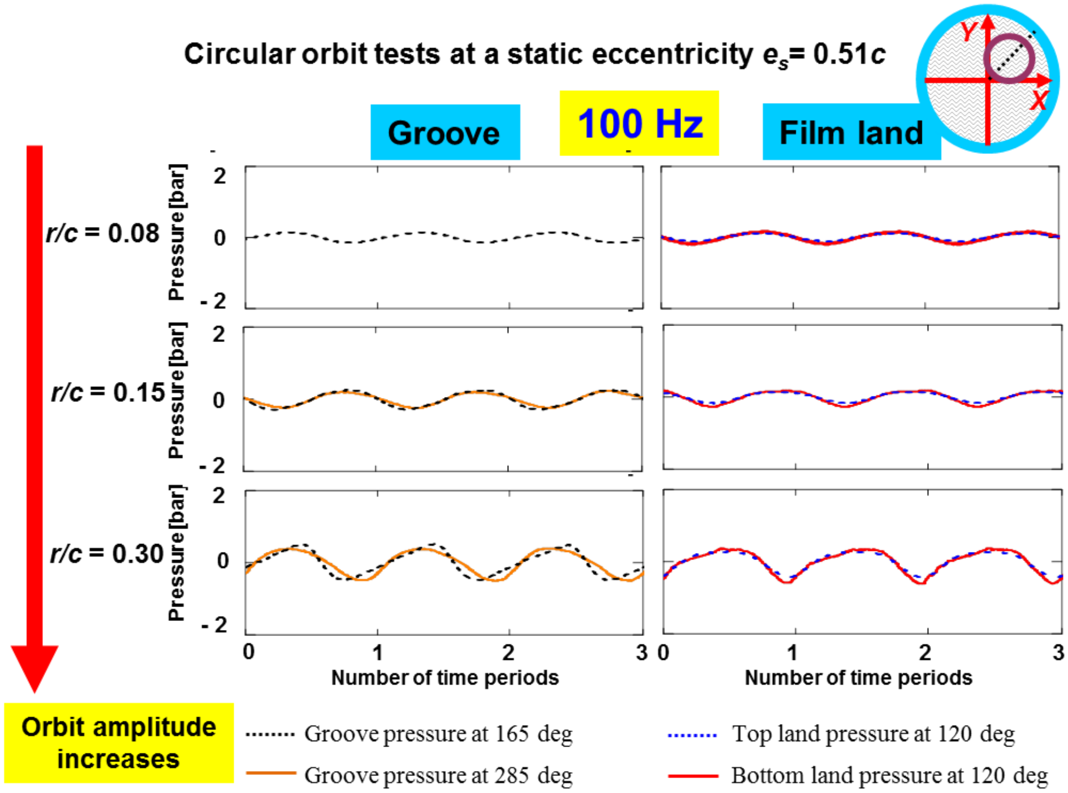

Fig. D.5 Lubricant dynamic pressures in the groove and the film lands versus number of time periods. Tests with circular orbit amplitudes *r*=0.08*c* to *r*=0.30*c* at static eccentricity e_S=0.51*c* and at a whirl frequency 100 Hz. Open-ends SFD with *c*=251.5 μm and two 25.4 mm length film lands.

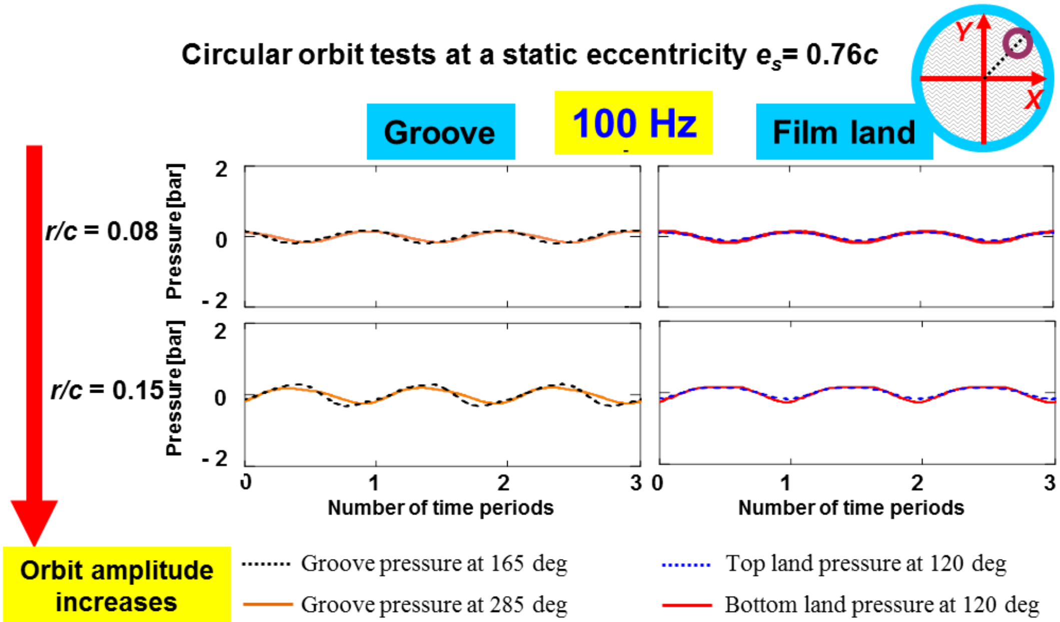

Fig. D.6 Lubricant dynamic pressures in the groove and the film lands versus number of time periods. Tests with circular orbit amplitudes r=0.08c to r=0.15c at static eccentricity e_S=0.76c and at a whirl frequency 100 Hz. Open-ends SFD with c=251.5 μm and two 25.4 mm length film lands.

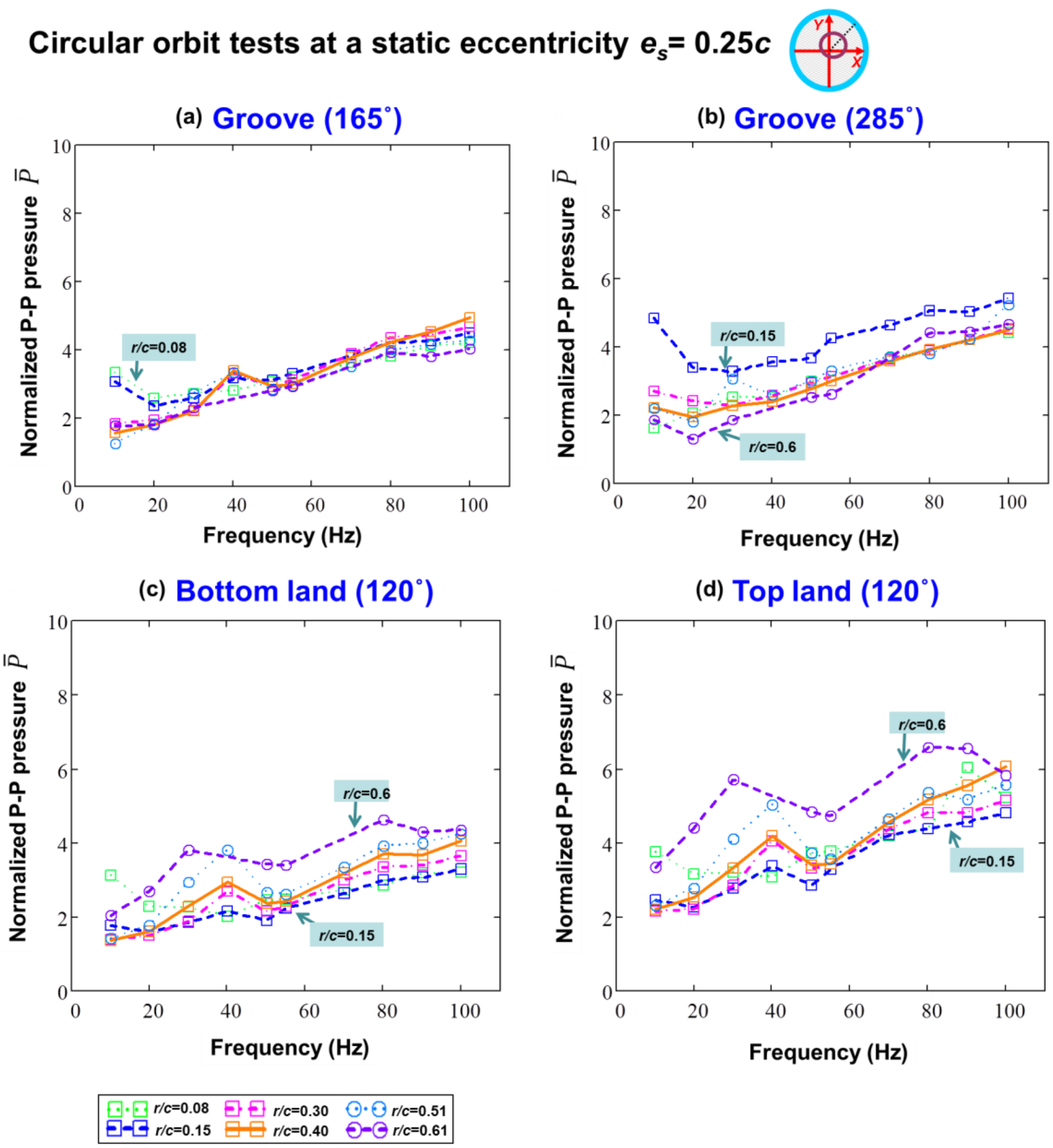

Fig. D.7 Normalized peak-to-peak pressure versus whirl frequency ranging 10 – 100 Hz. Tests with orbit amplitudes *r/c*=0.08 - 0.61 at static eccentricity (e_S=0.25*c*): at (a) Groove (165°), (b) Groove (285°), (c) Bottom land (120°), and (d) Top land (120°). Open-ends SFD with *c*=251.5 μm and two 25.4 mm length film lands.

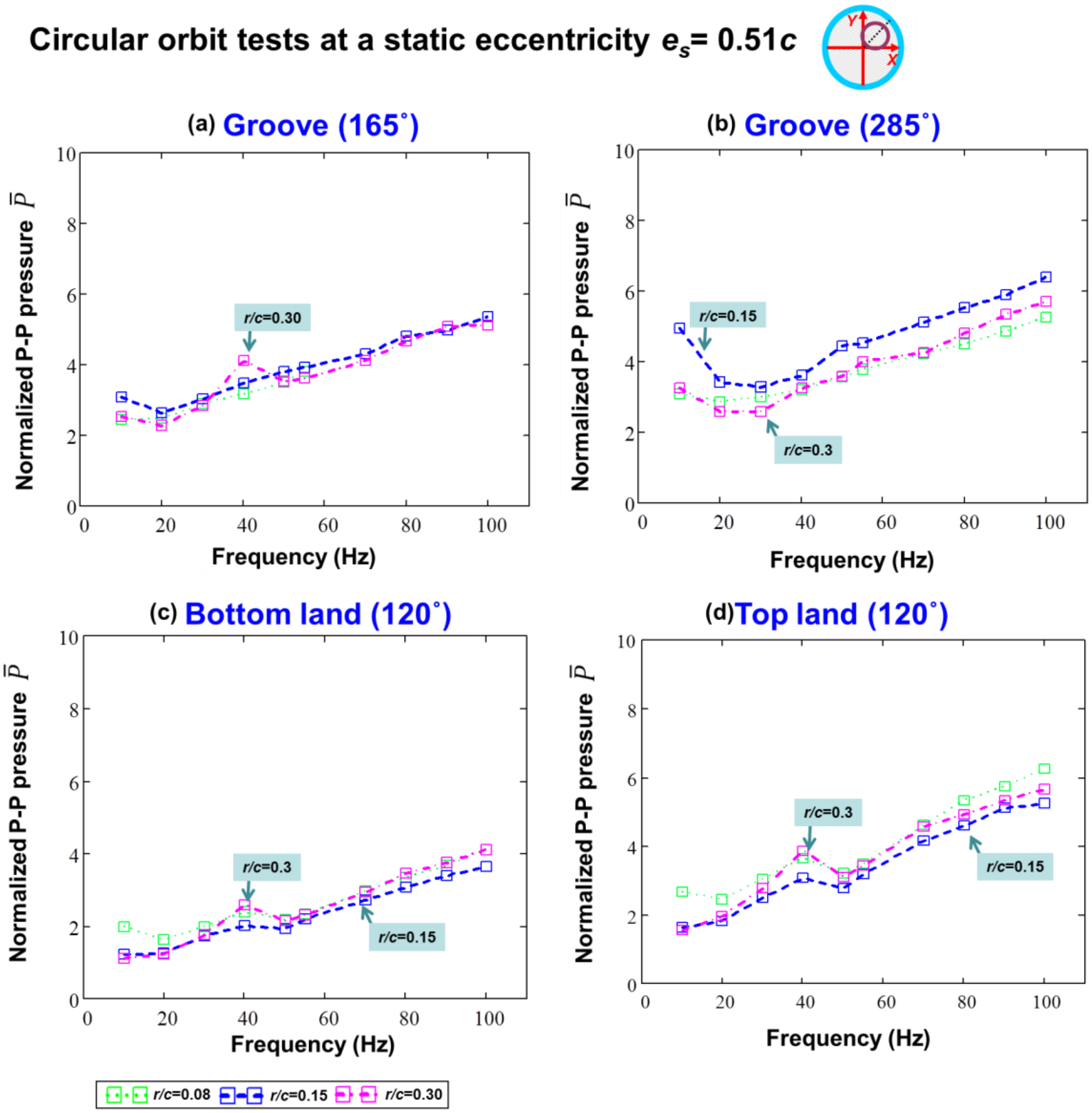

Fig. D.8 Normalized peak-to-peak pressure versus whirl frequency ranging 10 – 100 Hz. Tests with orbit amplitudes *r/c*=0.08 - 0.30 at static eccentricity (e_S=0.51*c*): at (a) Groove (165°), (b) Groove (285°), (c) Bottom land (120°), and (d) Top land (120°). Open-ends SFD with *c*=251.5 μm and two 25.4 mm length film lands.

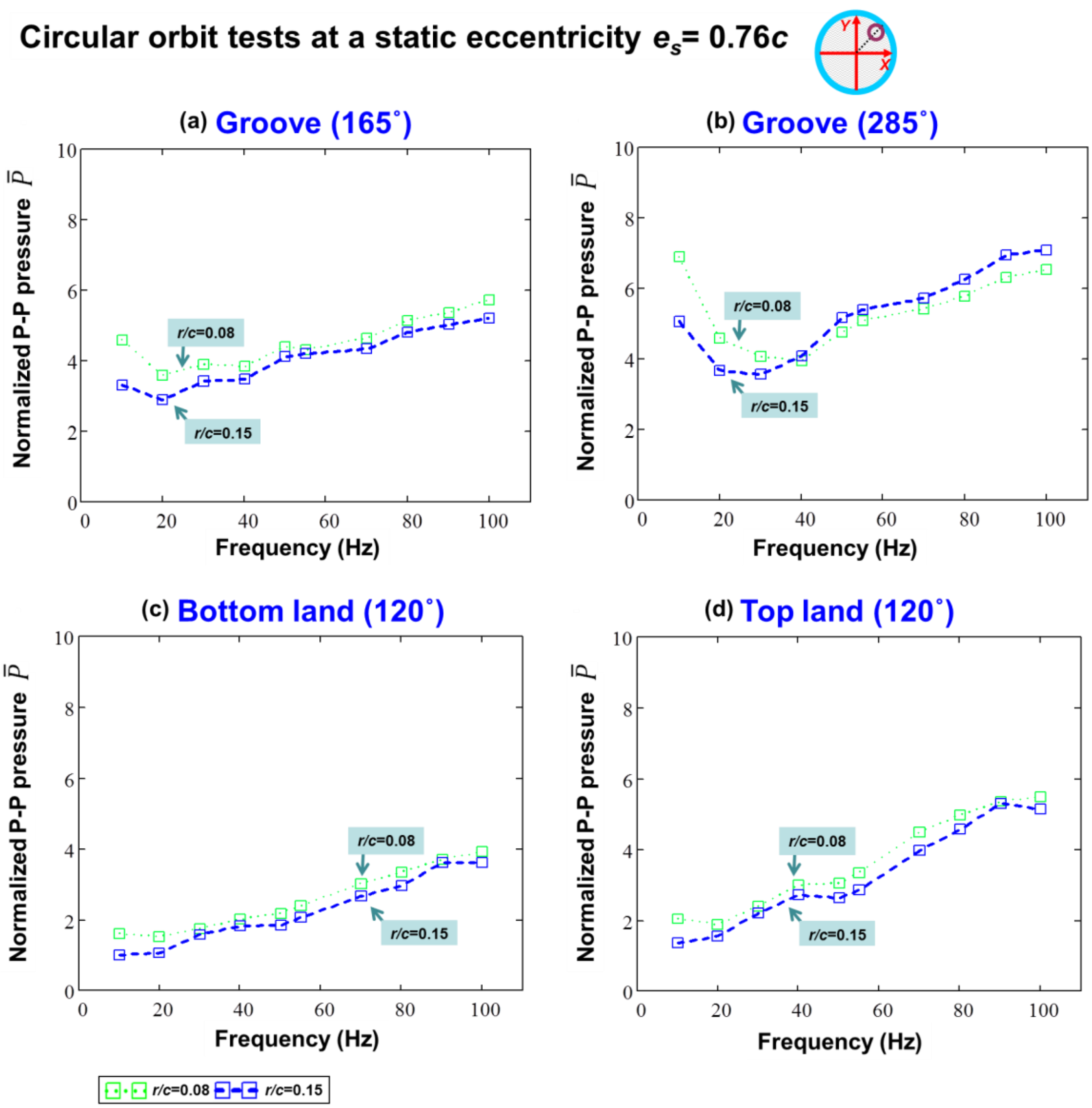

Fig. D.9 Normalized peak-to-peak pressure versus whirl frequency ranging 10 – 100 Hz. Tests with orbit amplitudes *r/c*=0.08 - 0.15 at static eccentricity (e_S=0.76*c*): at (a) Groove (165°), (b) Groove (285°), (c) Bottom land (120°), and (d) Top land (120°). Open-ends SFD with *c*=251.5 μm and two 25.4 mm length film lands.